Theses and Dissertations   Student Graduate Works

6-2006

Characterizing a Co-flow Nozzle for Use in a Filtered Rayleigh Scattering System

David S. Miceli

**CHARACTERIZING A CO-FLOW NOZZLE
FOR USE IN A FILTERED RAYLEIGH
SCATTERING SYSTEM**

THESIS

David S. Miceli, Ensign, USN

AFIT/GAE/ENY/06-J10

**DEPARTMENT OF THE AIR FORCE
AIR UNIVERSITY**

AIR FORCE INSTITUTE OF TECHNOLOGY

Wright-Patterson Air Force Base, Ohio

APPROVED FOR PUBLIC RELEASE; DISTRIBUTION UNLIMITED

CHARACTERIZING A CO-FLOW NOZZLE FOR USE IN A FILTERED RAYLEIGH SCATTERING SYSTEM

THESIS

Presented to the Faculty

Department of Aeronautical Engineering

Graduate School of Engineering and Management

Air Force Institute of Technology

Air University

Air Education and Training Command

In Partial Fulfillment of the Requirements for the

Degree of Master of Science in Engineering

David S Miceli, BS

Ensign, USN

June, 2006

CHARACTERIZING A COFLOW NOZZLE FOR USE IN A FILTERED RAYLEIGH SCATTERING SYSTEM

David S. Miceli, BS

Ensign, USN

Approved:

_____   _____
Dr. Mark F. Reeder, Assistant Professor (Chairman)   Date

_____   _____
Raymond C Maple, Lt Col, USAF (Member)   Date

_____   _____
Richard D Branam, Major, USAF (Member)   Date

Acknowledgments

I would like to express my sincere appreciation to my faculty advisor, Dr. Mark Reeder, for his guidance and support throughout the course of this thesis effort. His insight and experience was certainly critical to my understanding of the subject matter. I am also indebted to the many maintenance professionals who spent their valuable time to help set up and maintain the experiment.

David S. Miceli

To Mom and Dad

Table of Contents

List of Figures

XI

List of Tables

Nomenclature

a………………………………………………………………Speed of sound

d…………………………………………………………...……Hydraulic diameter

FRS…………………………………………………….... Filtered Rayleigh scattering

I………………………………………………………….…Turbulence intensity

M………………………………………………………..….Mach number

N……………………………………………………………Number of scatterers

P……………………………………………………………Static pressure

P_o………………………………………………………..…………Pressure

q……………………………………………………………Dynamic pressure

R……………………………………………………………Air gas constant

R`……………………………………………………………Distance from scatterer

SLPM………………………………………………………...……Standard liters per minute

Re………………………………………………………...……Reynolds number

Re,crit …………………………………………………..Critical Reynolds number

Re,h …………………………………………………………Hydraulic Reynolds number

t……………………………………………………………Temperature

u_m………………………………………………………Mean hydraulic velocity

v……………………………………………………………Velocity

α…………………………………………………………Under-relaxation parameter

α`………………………………………………...…………Polarizability

Δ……………………………………………………Change in Fluent solution from previous iteration

ε……………………………………………………Epsilon- Turbulence model parameter

γ…………………………………………………………Ratio of specific heats

v…………………………………………………...…………Kinematic viscosity

φ……………………………………………………………Fluent solver parameter

ρ……………………………………………………………Density

AFIT/GAE/ENY/06-J10

Abstract

Research was conducted on the flow field exiting a co-annular flow nozzle for use in filtered Rayleigh scattering flow visualizations. More specifically, the flow visualizations were of the flow field exiting a coflow nozzle and illuminated by a tunable, nominal 4.2 watt narrow line width Argon laser operating at 514.5nm. ND:YAG lasers are typically used in this application, but some of the properties of a tunable Argon laser make it an attractive alternative. Before generating flow visualizations, the coflow nozzle was characterized both experimentally and computationally. Due to a flow asymmetry in the outer annulus flow field, the nozzle was redesigned using a commercially available computational fluid dynamics program (Fluent) to produce a more homogeneous exit plane velocity profile. The redesigned nozzle was built and experimentally tested through the use of a three dimensional traverse controlled Pitot probe resulting in good relationship between the computational and experimental results. The sharp cutoff molecular iodine filters used to reduce the incident frequency light were tested and the locations of their iodine absorption transitions were determined. Finally, the argon laser was used to produce flow visualizations at both 100 Hz and 1 kHz frame rates.

I. Introduction

Background

Filtered Rayleigh scattering (FRS) is a developing non-intrusive, optical method of measuring velocities and determining thermodynamic properties of flow fields. By passing a narrow line width laser through a moving flow field, the scattered light is frequency shifted by the Doppler Effect, while at the same time being frequency broadened by the Maxwellian velocity distribution of the molecules in the flow (Seasholtz, Buggele). The resulting frequency shifted and broadened signal is elastically scattered by a phenomenon known as Rayleigh scattering (Milonni, Eberly). The scattered light radiates with the same frequency as the incident light plus the change in frequency caused by the Doppler effect from the flow velocity. By filtering out the original laser signal with a sharp cutoff molecular filter such as mercury or iodine, only the Doppler shifted signal remains (Miles et al). The resulting signal can then be collected by a camera and compared in frequency and intensity to the original signal to extract information about the flow field. This is the basis for the fluid diagnostic technique known as filtered Rayleigh scattering.

There are many alternatives to using filtered Rayleigh scattering such as using Pitot probes, Shlieren photography or hot wire techniques. However, one of the most attractive aspects of FRS is that it is non-intrusive, which eliminates the flow interference by Pitot probes and hotwire devices, or, more importantly, the sting systems used to control these instruments. Another attractive element of FRS is that it allows for simultaneous measurement of multiple flow properties including density, temperature and

velocity through the same experimental setup (Elliott and Samimy). In addition to such quantitative data, flow visualizations of supersonic and subsonic flows are possible with FRS.

The concept of filtered Rayleigh scattering is a relatively new one, initially contrived by Shimizu et al in 1983 while developing a High Spectral Resolution LIDAR system for atmospheric property measurements (Shimizu and Lee). FRS is certainly a developing technology and as such, there are several competing methodologies. Practically everything about the experimental setup varies from one experimentalist to the next, and there is no definitive answer as to what approach is the best. The main variances between experimental setups are the laser and camera systems beings used.

Most FRS systems use neodymium-doped yttrium aluminum garnet (ND:YAG) laser in a frequency doubled mode emitting a pulsed beam centered on 532 nm. Although this is well in the visible range and well aligned with a cutoff notch of the molecular iodine filter, the ND:YAG lasers have some shortcomings that prompt investigation into other laser media. The Argon laser used in this experimental setup is a nominally 4.2 watt, continuous wave laser centered on 514.5 nm. This high laser output power leads to a maximum data rate of 1 kHz while operating at an etalon temperature of 53.145 C. This laser also has the ability to mode hop, or discretely switch frequencies to shift the Rayleigh scattered signal in relation to the filter's absorption bands.

Previous experiments have typically struggled with particle induced scattering coming from the surrounding environment and flow entrainment (Seasholtz et al). In an effort to reduce particle influence, researchers have gone to great lengths to maintain a

particle free environment, or apply a low velocity particle free flow field around the high velocity flow field to be examined (Panda, Gomez). The flow field providing the Doppler Shift in this experiment came from a co-annular flow nozzle capable of independently varying mass flow rates for the outer annulus and central jet flow fields. This arrangement provides a separate clean flow field around the central jet and reduces particle entrainment. The velocities of various combinations of outer annulus and central jet flow mass flow rates were experimentally determined through the use of a traverse driven Pitot probe.

Bluff body flows often produce asymmetric flow fields although they may be symmetrically shaped (Pinho, Whitelaw). These flow fields have been studied both experimentally and computationally not only to discover the cause of the flow asymmetry, but also how to correct it (Davies). When a significant asymmetry was discovered at the exit plane of the outer annulus of the coflow nozzle used in this experiment, the internal flow structure of the outer annulus and intake pipe were studied using Fluent based computational fluid dynamics. The experimentally determined flow field at the exit of the outer annulus was matched by the CFD model, and then the nozzle was redesigned and tested in the Fluent environment to reduce the magnitude of the asymmetry. The redesigned nozzle was then built and tested showing a reduced asymmetry and good correlation to the CFD results.

Problem Statement

The development of a laser based filtered Rayleigh scattering system capable of gathering meaningful qualitative data takes a great deal of time and effort. One goal of

this body of work is to piece together, install, synchronize, test and finally employ an FRS system to generate flow visualizations of a coflow jet. To facilitate comparisons to future flow visualizations, the flow field of the co-annular flow nozzle must be well defined through a traditional experimental method such as a Pitot probe.

Research Objectives/Questions

Research Objectives

At the onset of this research there were several goals. First, since all of the individual components of the experimental setup were new, they had to be installed, debugged, tested and synchronized. Next, the coflow nozzle used in the setup had to be characterized using a traditional Pitot probe to gather velocity data of the flow field. Once the flow field was known, the FRS system was employed to generate flow visualizations. Finally, the flow visualizations were compared to the data gathered experimentally by the Pitot probe measurements.

Questions

Although the final research goals were well known, several aspects of the experiment were unclear. The first unknown was the characteristics of the flow field exiting the coflow nozzle. It was assumed that the outer annulus and central jet flow fields would be axisymmetric and concentric, but this had to be confirmed through experimental analysis. If the nozzle was not fully tested before generating flow visualizations, any flow asymmetries discovered by the flow visualization would be difficult to explain.

4

The next unknown was the absorption characteristics of the molecular iodine filter. This data cannot be imported from other researchers work because of the high variability in the length, density and temperature of the iodine cells, all of which are influential in the iodine absorption characteristics. These characteristics would have to be experimentally determined before generating flow visualizations.

Most FRS systems are based around a frequency doubled injection seeded Nd:Yag laser operating at 532 nm. Because of the competing mode emission prevalent in these lasers as described by Seasholtz it was decided to base this system around a continuous wave argon ion laser centered on 514.5 nm. By eliminating the competing mode, the resulting received signal should contain less Mie scattering signal. It is unclear however how much particle scattering will remain, even with the flow provided via a co-annular nozzle designed to reduce particle scattering.

The next question about this system is how fast data can be gathered. Because the PCO.4000 camera used is capable of exposure times down to 5μs without delay, the real limiting factors will be the intensity of the scattered signal and the post processing methods used to extract the data from the images. Ideally, this system will be capable of high enough frame rates to facilitate time resolved data acquisition in future applications.

Research Focus

The focus of the research contained in this body of work is on the setup and initial flow visualizations generated through an argon ion laser based filtered Rayleigh scattering fluid diagnostics system. This work will include characterization of a co-annular jet flow field at varying flow rates through a traditional Pitot probe measurement.

This data was used as a basis for comparison to the laser based flow visualizations using a molecular iodine filter.

Methodology

The testing methodology is extensively outlined in chapter III of this paper.

Implications

This body of work will serve as a starting point for future research in this area. Procedures for system operation and adjustment such as determining location of the iodine cell absorption transitions will be thoroughly outlined for future researchers. The Pitot probe resolved flow fields of the coannular jet under different flow configurations may be referenced when determining flow velocities through FRS imaging. Testing should provide a clear proof of concept for a newly installed experimental setup including baseline filtered Rayleigh scattering flow visualizations and determination of frame rate capabilities. Finally, several issues relating to the experimental setup or equipment will be discovered and resolved.

II. Literature Review

Introduction and Historical Perspective

The central theme of this literature review is the history and development of filtered Rayleigh scattering as a flow diagnostics technique including key components of the experimental setup. The concept of filtered Rayleigh scattering is a relatively new one, initially conceived by Shimizu et al in 1983 while developing a High Spectral Resolution LIDAR system for atmospheric property measurements (Shimizu and Lee). Since its inception, FRS has been researched and employed as a non-intrusive, optical method of determining thermodynamic properties and velocity measurements of a flow. FRS is certainly a developing technology and as such, thorough descriptions of the background theory and all components of the experimental setup are warranted.

Rayleigh Scattering

When an incident field strikes a particle or molecule of sufficiently small size the incident wave is scattered. The scattered wave oscillates at the same frequency as the incident field, and in turn, radiates at this frequency. This effect is due to the Lorentz model of atoms, which is a model of how an atom reacts to a perturbation more so than an atomic model (Milonni and Eberly). After being scattered by the particle the incident wave continues about its initial path with an attenuated intensity as seen in Figure 1. This process is known as Rayleigh scattering, named after Lord Rayleigh, the scientist who determined that the sky was blue in color because of this scattering effect. Rayleigh scattering has a fourth power inverse scattering intensity dependence on wavelength, so

as the wavelength increases, the Rayleigh scattering intensity decreases rapidly (Milonni and Eberly). This explains why the short wavelength of blue is the dominant color scattered in the atmosphere.
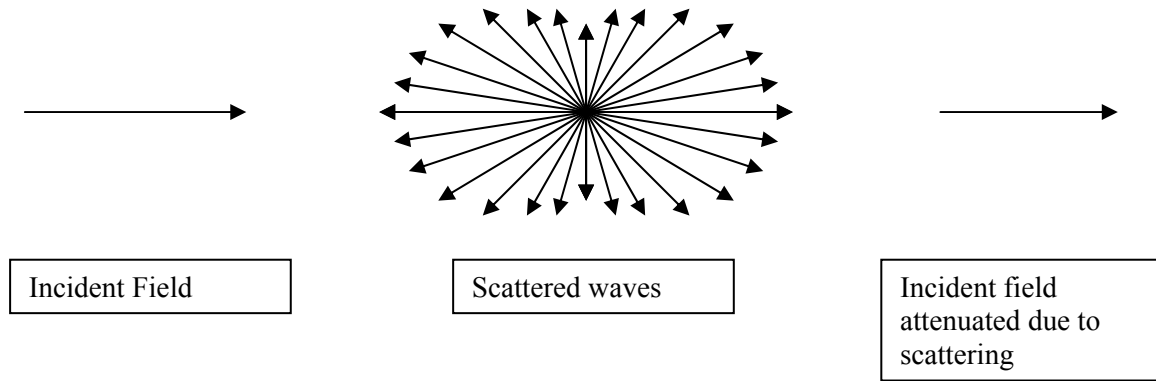
Figure 1- Relationship of Rayleigh scattered signal to incident field.

As seen above in Figure 1, the intensity of the scattered waves varies with the angle of the scattered wave relative to the incident light. This relationship is characterized below in equation 1.

$$I = I_o \frac{8\pi^4 N \alpha^{\cdot 2}}{\lambda^4 R^{\cdot 2}} (1 + \cos^2 \theta)$$ (2.1)

Given the relationship above, the scattering at right angles to the incident light direction is only half the maximum intensity found at no angle to the incident light direction. For Rayleigh scattering to take place, the particle must have a diameter less than one-tenth that of the wavelength of the color of light. For particles sufficiently larger than the wavelength of incident light, the induced scattering is known as Mie scattering.

Mie scattering is not very wavelength dependent and produces a large asymmetric scattering lobe in the direction of the incident field as shown below in figure 2. This is because the particles have a much larger scattering cross section.
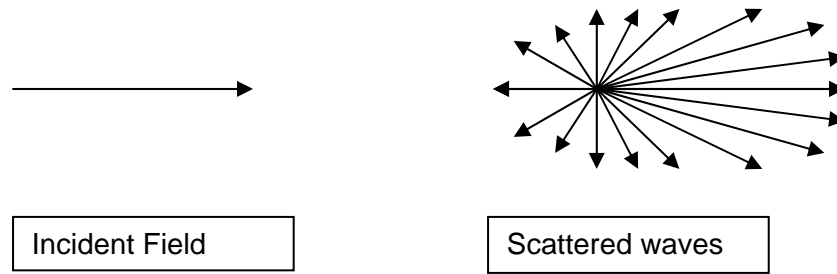
Figure 2- Relationship of Mie scattered signal to incident field.

This Mie scattering is what causes an observer to see a bright white glow around the sun, or around bright lights at night. This bright glow is only seen close to the light source because the intensity of Mie scattering rapidly reduces as the relative angle between the observer and incident field increases.

A third type of scattering, known as Raman scattering, is less dominant in the frequency range used for FRS diagnostics. Raman scattering is an inelastic scattering that shifts the photon frequency and energy levels. It is typically used in combustion diagnostics and clean flows because it facilitates determination of molecular composition of flows. This is because the scattered Raman signal is species specific and linearly proportional to the species number density (Eckbreth).

The relationship between the intensities of the Rayleigh, Mie and Raman scattering signals is important to understand when examining an image of scattered laser light used for flow diagnostics. Experimentally determined values for Mie scattering from a frequency doubled Nd:YAG laser are three orders of magnitude larger than the Rayleigh scattering, which is still three orders of magnitude larger than the Raman scattering signal. Although this is for a specific case examining N_2 at 2000 K, it clearly shows that the three scattering signals are quite different in intensity (Eckbreth). This

relationship also shows the importance of having a particle free flow when Mie scattering is undesirable; failure to do so will lead to images dominated by the much stronger Mie scattering signals.

Laser use in FRS

Filtered Rayleigh scattering can be employed to determine the thermodynamic properties and velocities of a flow. To be useful in gathering data however, specific properties of the incident light are required, including a narrow frequency span and directionality; this is why lasers are commonly used. LASER stands for Light Amplification by Stimulated Emission of Radiation. Lasers were initially theorized by Albert Einstein in 1917 although the first laser patent wasn't applied for until 1958 (McAlister).   Lasers work by stimulating a lasing media filled cavity with reflectors on either end. By exciting or "pumping" the media, the electrons are driven to a higher energy level that they cannot maintain. When the excited electrons return to a more relaxed state, they release photons.   Some of the released photons travel parallel to the two mirrors in the chamber, and as the media continues to be pumped, the photons continue to be emitted and cause additional electrons to release more photons. The mirror on one end of the cavity is entirely reflective, whereas the mirror on the other end allows some photons to pass through it. The photons that exit the chamber produce a monochromatic, coherent and directional beam known as a laser beam. A simplified schematic of a laser is shown below in Figure 3. By adjusting the distance between the two mirrors, the wavelength of the emitted laser can also be adjusted. This is helpful in tuning the laser for wavelength sensitive tests such as filtered Rayleigh scattering.
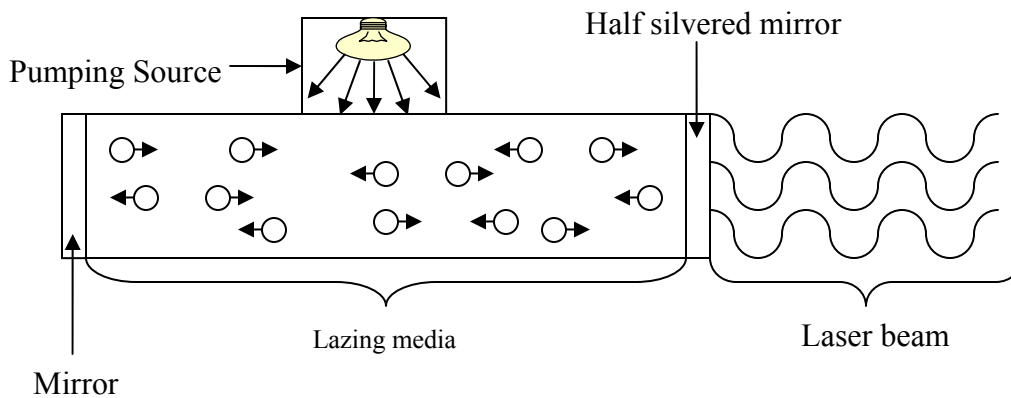
Figure 3- Simplified diagram of laser operation

The three qualities of the laser that make it especially useful in conducting

experiments with Rayleigh scattering are that it is monochromatic, coherent and

directional. The energy difference between the excited and relaxed state of the electron

in the lasing media determines the frequency of the emitted photon. Because of this, and

because the lasing media is homogeneous, only one frequency of photon will be

repeatedly emitted producing a monochromatic beam of light. The narrower the

frequency span of the emitted photons, the more monochromatic the laser beam. This

quality lends itself to testing in this experimental setup because the laser can be tuned to

the sharp edge in the absorption band of a filter.

The second important characteristic of lasers is that they are coherent. Laser light

is called coherent because the emitted beam is made up of waves of light all of the same

phase and wavelength.

The third important laser quality taken advantage of in this experiment is that

lasers are directional. This is to say that all the photons leaving the laser head are

traveling in parallel paths that do not diverge. Although this is the theoretical laser ideal,

in actuality the beam will diverge at a rate that is a function of the individual laser. This

11

quality of a near unidirectional light source is useful in testing because the laser will have a distinct and narrow beam width and therefore test area. In addition to this, because the light is assumed unidirectional, any calculations involving the Doppler shift of the beam are simplified.

The lazing media is a very important aspect of the laser and is responsible for many of the properties of the beam. Some of the more common laser media used for flow diagnostics are solid state Nd:Yag, Argon and Ti:Sapphire.   Solid-state lasers have lasing material distributed in a solid matrix (such as the ruby or neodymium:yttrium-aluminum garnet "Yag" lasers). Although Nd:Yag lasers emit infrared light at 1,064 nanometers (nm) Miles et al, and many other FRS experimentalists, use Nd:Yag lasers in a frequency doubled state of 532 nm. This allows for its light frequency to be centered on one of the sharp absorption bands of molecular iodine.   Many researchers have found that the injection-seeded pulsed Nd:Yag lasers have an inherent quality that produces competing modes in addition to the selected frequency. This competing mode can effectively reduce the iodine absorption from 10^{-5} to $3x10^{-3}$, thus reducing the effectiveness of the system (Seasholtz, Buggele). Seasholtz tried to circumvent this problem through the use of an intercavity etalon, but the transmitted light was still dominated by the injected frequency due to Mie scattering. He later went on to use an argon-ion laser for flow diagnostics of sooting flames in harsh environments (Seasholtz, Greer). Although argon lasers aren't as popular a choice in laser diagnostics, they are attractive because of their narrow line width and absence of competing modes.

Filtered Rayleigh Scattering

Although Shimizu et al first used molecular filters when developing a high spectral resolution LIDAR system in 1983, the first in depth experiments based on FRS were in 1991. Miles, Lampert and Forkey began by determining instantaneous velocity fields using filtered Rayleigh scattering and immediately followed up using FRS on supersonic flow fields. Their research was picked up quickly by Elliott and Samimy who expanded the diagnostic capabilities of FRS to include simultaneously determining multiple flow properties including density, velocity and temperature. They called their method filtered angularly resolved Rayleigh scattering or FARRS, because of the method of gathering the scattered signal from multiple angles. Like many others, Elliott et al used a 532nm frequency doubled Nd:Yag laser in conjunction with a molecular iodine filter to generate and filter the signal.

Filters

Among the first experimentalists to begin using a molecular filter in concert with Rayleigh scattering were Miles et al (Miles, Forkey and Lempert). Their research began with simple flow visualizations in both subsonic and supersonic flows, but quickly evolved into complex flow diagnostic experiments. To facilitate these experiments, Miles et al further researched different molecular and atomic filters using iodine, mercury and rubidium. The group identified three important aspects of these 'notch' filters. First, they must provide a sharp cutoff notch with discrete edges on either side. Two, that they provide very strong extinction in the blocking region and allow for 100% transmission for all other wavelengths. Finally, the filters must have absorption notches in the range of current narrow line width tunable lasers. Shown below is a schematic diagram derived

from Miles et al that depicts the effect of a molecular filter on the Rayleigh scattered
light.
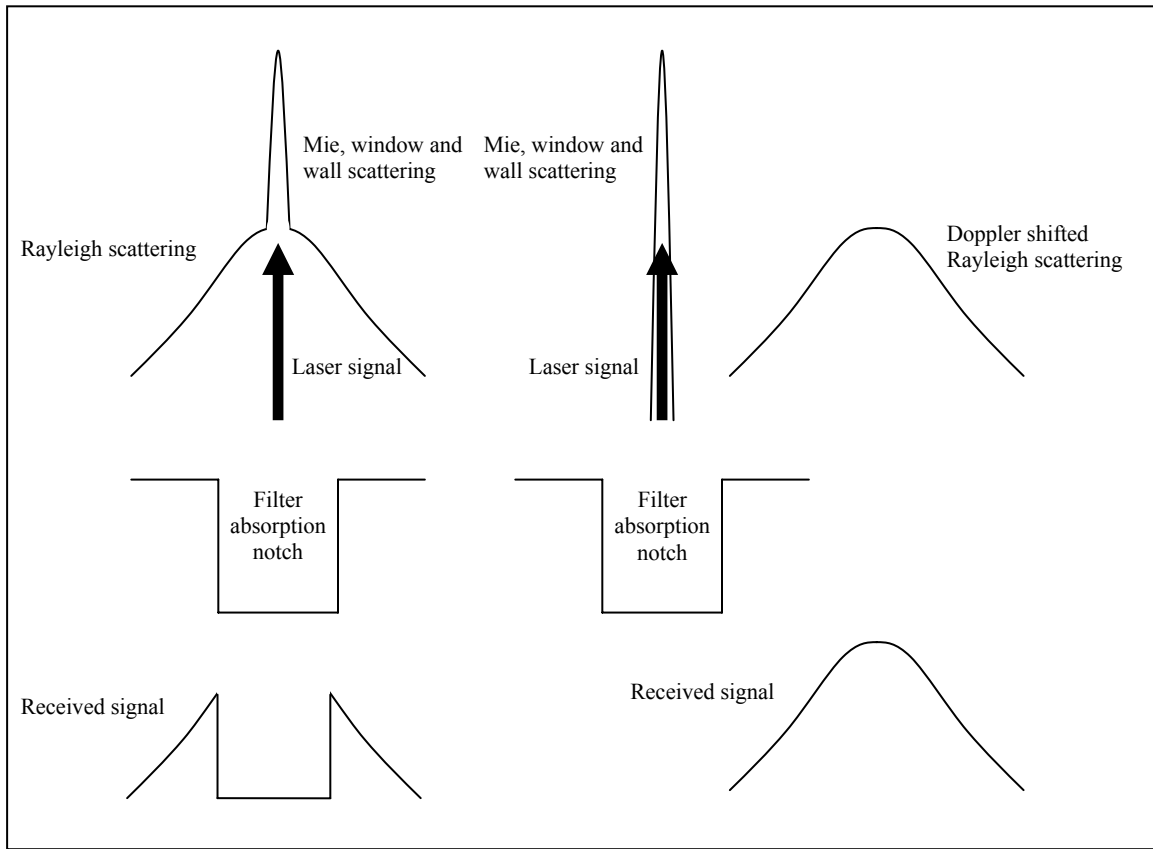
Figure 4- Pictorial representation of filtered Rayleigh scattering

      This schematic also shows how Doppler shifting the signal can move the received
Rayleigh scattering outside the absorption well of the sharp notch cutoff filter.
Shown below is a typical absorption profile for a molecular iodine filter (Elliott and
Samimy).
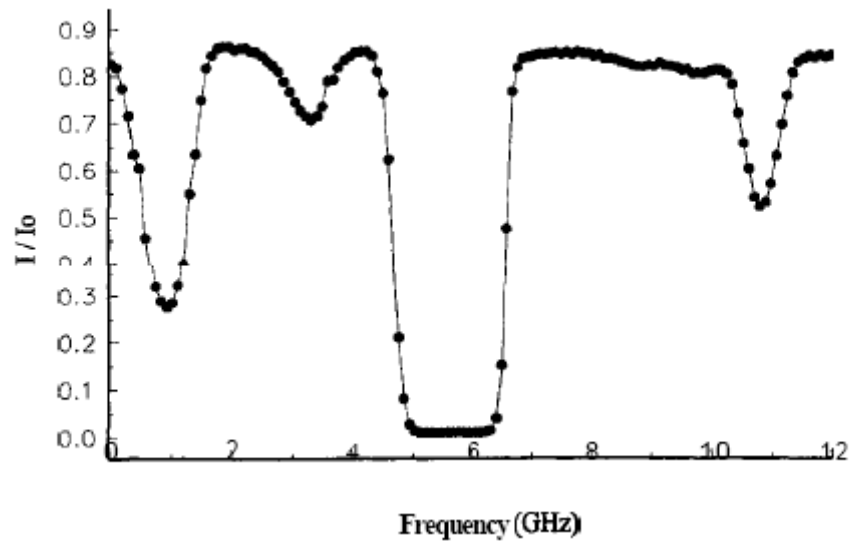
Figure 5- A typical ND:YAG (532 nm) absorption profile for a molecular iodine filter (Elliott and Samimy)

The notch centered around ~5.9 Ghz is the notch typically used for laser diagnostics using either Nd:Yag or argon lasers by many experimentalists including Miles, Elliott and Samimy.   Their research also showed that at no frequency of the iodine absorption profile was there a one hundred percent absorption notch, although some came quite close.

Flow Seeding

By seeding a flow, the Mie scattering produced from particles is more significant than the Rayleigh scattering from the molecules in the flow itself. This facilitates determination of flow velocity because the particles travel with the flow at the same speed and provide a larger signal level. A side effect of seeding the flow however is that flow temperature measurements can no longer be made. The more massive particles have substantially reduced thermal motion and because the exact mass of the particles is unknown, the temperature cannot be accurately determined (Elliott, Boguszko).

15

Coflow Nozzles

Because filtered Rayleigh scattering is based on the Doppler effect, it requires a flow field to generate the Doppler shift. The field comes from a small co-annular, or coflow, nozzle that generates two separate flow fields, a central jet, and an annular flow surrounding the central jet. This literature review will include both flows.

The central jet portion of the coflow nozzle is best compared to a simple turbulent pipe flow. Experimentalist Osborne Reynolds determined that in fully developed pipe flow, turbulence generally onsets near a Reynolds number of 2300. This phenomenon becomes more pronounced as the Reynolds number increases and turbulent effects dominate the flow causing the velocity distribution to become less skewed towards the center of the pipe. These pipe flows were first studied by Henry Darcy and Prandtl in the 1800's and their theoretical results were later compared to experimental data showing impressive similarities (Schlichting, Krause).

Even with significant boundary layer effects, pipe flows, especially those with no bends, typically have axisymmetric velocity profiles. Helmholtz and Kirchhoff first studied the jet problem in the 1850's and their research has become a mainstay of fluid dynamics. It has been determined that jet velocity profiles diverge in a predictable manner as they travel downstream of the exit plane.

The annular flow is more complicated than the central jet, and requires more discussion. Annular flows are of importance in many situations that have axisymmetric annular flows centered on one another. These geometries are often found in combustors, turbofans, chemical processing and partial admission devices. Research on these flows often focuses on a bluff body or partially blocked flow. This is a pipe with a blocking

geometry located down the long axis to divert the flow towards the pipe wall (Davies,

Beér). The blocking geometry is typically a disk or cone, whose diameter in relation to

the pipe diameter determines the blocking ratio.

$$BR = do/d \qquad\qquad (2.2)$$

Downstream of the blocking body there are three separate and unique regions of

flow. The recirculation zone, transition zone and established flow zone, as Davies defines

them, can best be illustrated in Figure 6.
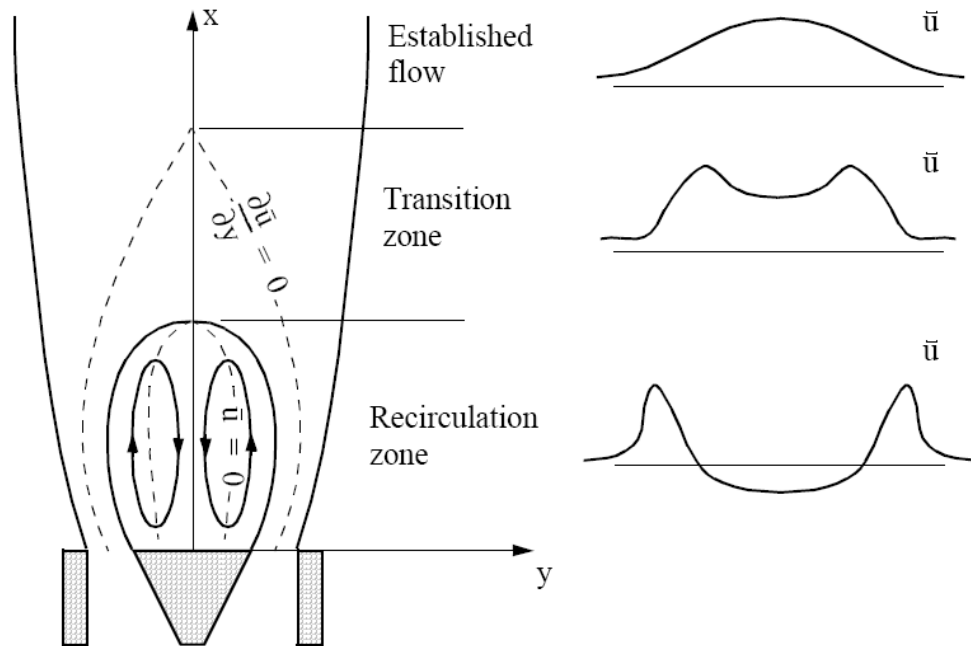
**Figure 6- Pictorial representation of the flow field from a bluff body annular jet from Davies and
Beér.**

Research has repeatedly shown that the zone lengths and blockage ratio are

related and as the blockage ratio increases, the ratio of recirculation length to blockage

diameter decreases (Davies, Durao, Ko, Taylor). Also, the ratio of reverse mass flow to

total mass flow varies directly with blockage ratio. Davies also determined that the

turbulence intensity in the recirculation zone is particularly high, rendering standard k-ε

computational models inadequate.

Although the annular nozzle may be physically axisymmetric, quite often the flow

is not. Symmetric geometries for bluff body annular flows tend to have a flow velocity

bias to a preferential side. Pinho and Whitelaw also found that as the Reynolds number

increased between 400 and 6000, that the flow became more asymmetric. Further studies

at Reynolds numbers above 6000 showed even more of an asymmetry. In one instance

with a Reynolds number of 8250 the flow asymmetry was as much as 50% of its peak

axial velocity while in the recirculation zone. They attributed the asymmetry to the

amplification of instabilities being shed from the edge of the bluff body. Ching and

Shew, however, attribute the asymmetric flow to the imperfections and asymmetries in

the upstream geometry and flow conditions.

Summary of Archival References

At the conclusion of the literature search, several things became obvious. First,

previous experiments involving temperature and velocity measurements via FRS required

considerable expertise in the area and a great deal of time generating an effective

experimental setup. Because of time constraints, research goals were limited to

experimentally characterizing the coflow nozzle and generating flow visualizations

through the use of filtered Rayleigh scattering. Although the laser and experimental

setup may be capable of more quantitative data generation, time constraints prohibit their

examination.

A second point that became obvious through the literature search is that FRS is

not typically used to gather data in a temporal sense. Because ND: YAG lasers are

pulsed, their data collection rate is limited to their pumping frequency, and they are less suited for gathering time related data, especially for high velocity flows. Conversely however, the Argon laser used in this experimental setup is a continuous laser and may be used to take data continuously. The limiting factor of this laser is the amount of time the camera shutter needs to remain open to gather enough Rayleigh scattering signal to generate quality flow visualizations. The less exposure time required per picture, the faster the data rate of the system is. Several factors can influence this data rate: including ambient light, laser output, and the sensitivity of the camera. To reduce ambient light in the laboratory, all non-essential lights should be extinguished leaving only a single computer monitor. In addition to this, any holes allowing light from adjoining labs should be plugged. Finally, the camera should use a very low F-stop lens to maximize the amount of light allowed to strike the CCD.

An area in which the Argon laser should show improvement over the ND:YAG laser for use in FRS is the reduced emission of secondary modes. Because the Argon laser does not produce secondary modes, it should not encounter the additional Mie scattering caused by the 40GHz secondary mode emissions of the ND:YAG laser (Seasholtz, Buggele). These long wavelength modes allow for Mie scattering of particles in the flow and obscure the Rayleigh scattering. Because of the Mie scattering generated by the secondary mode associated with pulsed Nd:Yag lasers, an Argon laser may be advantageous for use in sooting flames.

Next, it is clear that although the co-annular nozzle has a symmetric exit plane geometry, the flow field exiting the nozzle may not be symmetric. This chance of

19

asymmetry is further increased by the fact that there is only one air inlet pipe for the outer

annulus oriented at a 90 degree angle to the exit plane.

III. Methodology

Experimental Setup- Pitot Probe

The first step in the process of characterizing the coflow nozzle was to develop a three dimensional map of the velocity field exiting the nozzle. To accomplish this, an Aerotech A3200 traverse was used to sweep the Pitot probe through the flow field of the coflow nozzle. Shown below in Figure 7 is a block diagram of the computer code written to move the traverse through the three dimensional flow field. The actual computer code, written in G-code language, is included as appendix A.
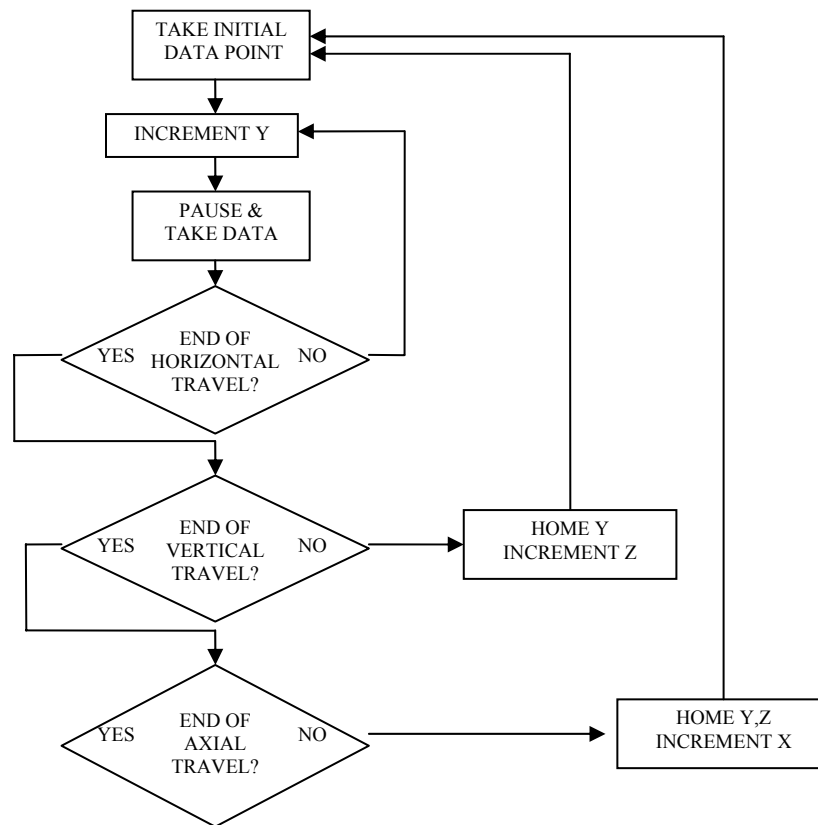
Figure 7- Block diagram of G-Code written to control the A3200 traverse.

The data resolution of the flow field depends on the grid spacing mapped by the Pitot probe. A grid of 0.25 mm^2 cells was mapped at an L/D from zero, the exit plane, to

five. The reference diameter is the diameter of the outer annulus of the coflow nozzle, which is 24.4mm. Data was only taken out to five diameters. At that point the flow will only continue to diverge and slow as it moves away from the nozzle while at the same time entraining more particles.

The pressure transducer voltage output was routed to a personal computer through a National Instruments multifunction I/O board. This pressure data was simultaneously logged in concert with the instantaneous location of the probe via the traverse. The data logging was facilitated by a Lab View script that coordinated the traverse movement and the input from the pressure transducer. To ensure that the output of the pressure transducer was not influenced by the motion of the Pitot probe, the Lab View script had a built in dwell time of a half second. Shown below in Figure 8 is a schematic layout of the experimental setup for mapping the coflow nozzle flow field.
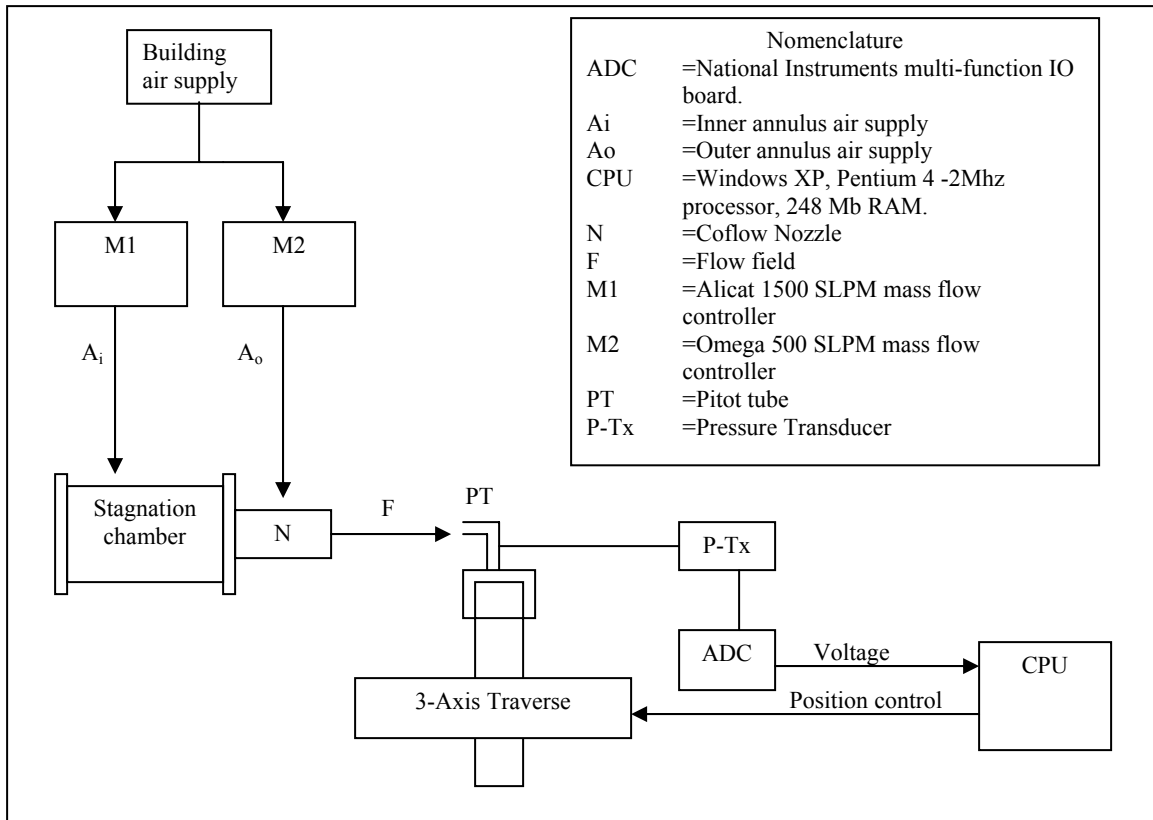
Figure 8- Experimental layout for traverse controlled Pitot probe measurements.

Experimental Setup- FRS

The experimental setup for producing flow visualizations was centered on an argon ion laser and a molecular iodine filter.

Laser

The laser used in this experiment is the Coherent Sabre-R series ion laser. The manufacturers specified maximum output in the single-line single-mode operation at a wavelength of 514.5 nm was 4.2 watts. Upon testing however, the laser showed outputs upwards of 9.5 watts. The beam dispersion is only 0.35mrad with a beam diameter of 2.1mm. Although a single laser line typically consists of numerous closely spaced frequency components, in single-frequency operation, all but one of these components

are suppressed by the use of an intercavity etalon. With the ν-track program engaged, the

frequency drift should be less than 30 MHz per degree Celsius and the temperature

should not change by more than +/- 1. ν -Track is a system that automatically varies the

laser cavity length to compensate for ambient temperature changes. With this feature

enabled, frequency drift, mode hopping and power drift are simultaneously eliminated.

With ν -track engaged, the absolute frequency of the system is locked to the extremely

stable temperature depended etalon transmission curve. This is accomplished by a

coordination motion of the four magnetic actuators which can translate the output coupler

longitudinally. The ν-track program is most effective while operating the laser in single-

frequency mode. (Coherent)

The Coherent Sabre-R series Argon lasers have the ability to discretely switch

frequencies within the range from 454-524nm (Coherent). This ability allows for the

laser to be tuned through the range of the cutoff notch of the filter. By moving the laser

towards the middle of a notch, the Rayleigh scattering signal will be passed for faster

flows while blocking the signal from the slower flows. Moving the laser frequency

towards the high frequency edge of the cutoff notch allows a broader Rayleigh scattering

signal to pass through the filter. This technique can be used to isolate the central jet flow

from the outer annulus flow when generating flow visualizations.

Laser safety information can be found in Appendix B.

The Coherent Innova Sabre-R series Argon laser was not a stand alone unit; it

consists of four primary components, power supply, heat exchanger, laser head and

remote. The power supply is the central distribution point for both power and cooling

water for the laser. As shown below in Figure 9, there are both a closed and open loop cooling water systems.
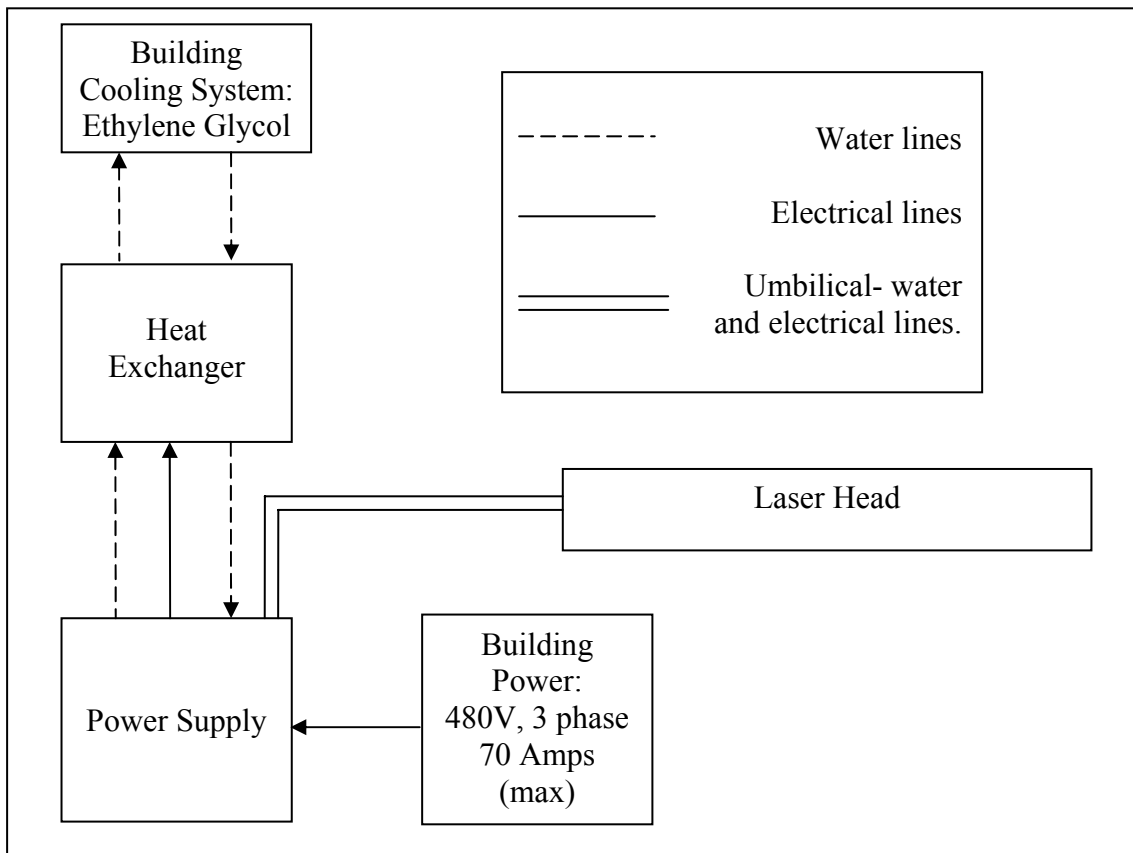
Figure 9- Laser power and water interconnection diagram.

The closed loop system continually recirculates water from the laser head, through the umbilical to the power supply, and then to the heat exchanger core. Surrounding hot water in the heat exchanger core is the outer loop of chilled ethylene glycol coming from the building cooling system. The coolant comes in chilled, extracts heat from the closed loop water system, and is returned to the coolant chiller.

Iodine Filter

Because the filter must have a sharp absorption notch centered on the beam wavelength of the laser, iodine is a well suited filter for an Argon laser. The Argon laser used has a beam wavelength of 514.5nm whereas the molecular iodine filters have a

sharp cutoff region centered on 514 nm. This relationship drives the requirement for the laser to have a very narrow line width so that all of its emitted light exists within the absorption band of the filter and can only pass through if it is shifted. Because the molecules in the flow are not homogeneous in velocity, the resulting signal will not only be Doppler shifted, but frequency broadened also (Seasholtz, Buggele). This phenomenon is further compounded by the fact that the laser light will be passing through the exhaust of a coflow nozzle involving two separate flow fields.

In this experiment, two different iodine cells are employed; one containing a higher density of iodine than the other. The two cells are used for different applications to be discussed later in the methodology section of this paper.

Because the filtered Rayleigh scattering flow visualizations rely on the absorption properties of the molecular iodine filters, it was necessary to characterize these filters. To do this, the laser was set in single-frequency mode centered on 514.5nm and the mode tune program described in the laser manual was run (Coherent). The mode tune program sets the intercavity etalon to its minimum temperature of 51.25 C and gradually heats to its maximum temperature of 56.50 C in 0.03 C increments. While this happens, the z-axis DAC program is simultaneously but minutely altering the laser cavity length to match the etalon transmission curve for optimum laser efficiency. The output of these programs is a gradually increasing laser frequency centered on 514.5nm. This facilitates monitoring the response of the iodine filter to different frequencies and determining at which etalon temperatures the cell is most effective. The experimental setup for this procedure is shown below in Figure 10Figure 10.
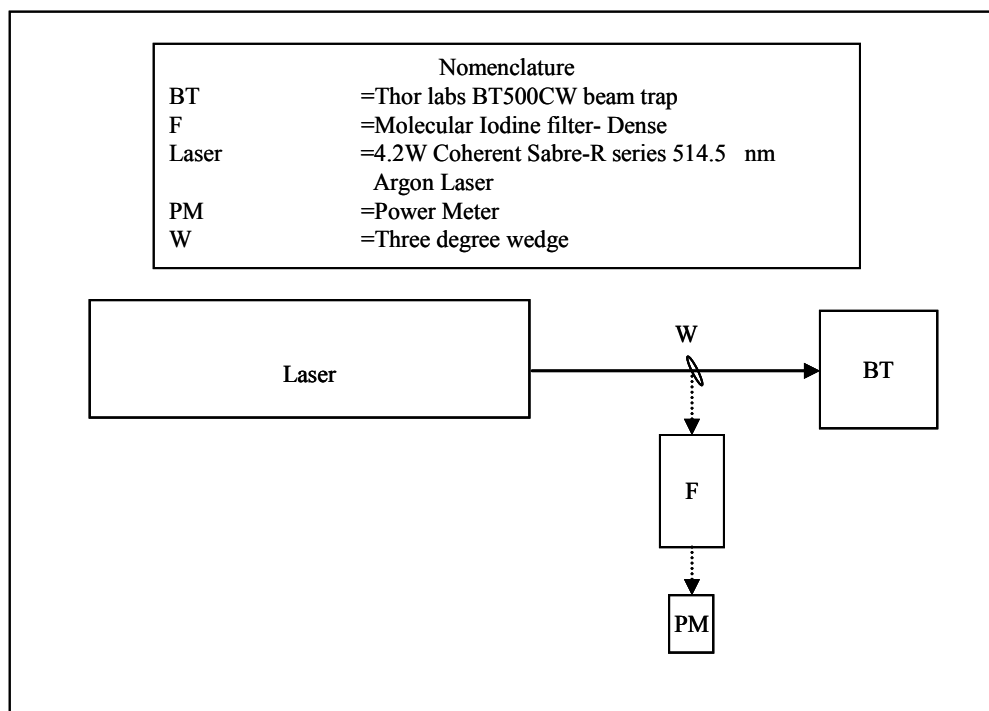
Figure 10- Experimental set up for iodine filter characteristics investigation

As shown above in Figure 10, a small portion of the laser beam is redirected

through the more dense iodine filter and into a laser power meter. While running the

mode-tune program, the instantaneous laser power output and power received were

recorded and compared. Etalon temperature regions that produced a significant reduction

in the ratio of power received to transmitted indicate laser frequencies that lie within the

iodine absorption notch. Another, more qualitative, method of determining the level of

iodine absorption was to observe the filter while mode-track was running. Frequencies of

iodine absorption were clearly indicated by the presence of a bright laser line through the

filter. In addition to this, if the laser power was sufficient, the iodine cell would fluoresce

an amber color distinctly different from the green laser light. The last method of

determining the level of iodine absorption was to monitor the intensity of the Rayleigh

and Mie scattering signals received by the camera through the filter using the

experimental setup shown in Figure 11. The mode-tune program was run several times

and each time the camera output was monitored and etalon temperatures corresponding to low received background scattering signals were recorded; the results remained consistent over many passes through the mode-tune program.

Flow Visualization Setup

Shown below in Figure 11 is a schematic of the experimental setup for the laser-based flow visualizations. The denser iodine cell is placed in front of the camera to filter the signal for the flow visualization whereas the less dense iodine cell is placed in front of the power meter to provide a reference power level. To set the laser frequency used for the flow visualizations, the laser is run through the mode-tune program and interrupted at a temperature corresponding to an absorption well. Once the mode-tune program was interrupted, the ν-track program was engaged to hold the laser output frequency constant. At the same time, the light regulation mode was also engaged to ensure that the beam strength stayed constant throughout testing. With ν-track and light regulation engaged, the cavity length was automatically varied through the ZDAC program to compensate for changes in temperature.

The iodine cell was placed nine inches from the laser line while perpendicular to and at a declination angle of 23.5 degrees with respect to plane of the optical table. Although this angle reduced the Doppler shift of the signal it was required to reduce the strong buffeting of the filter lens by the flow field.
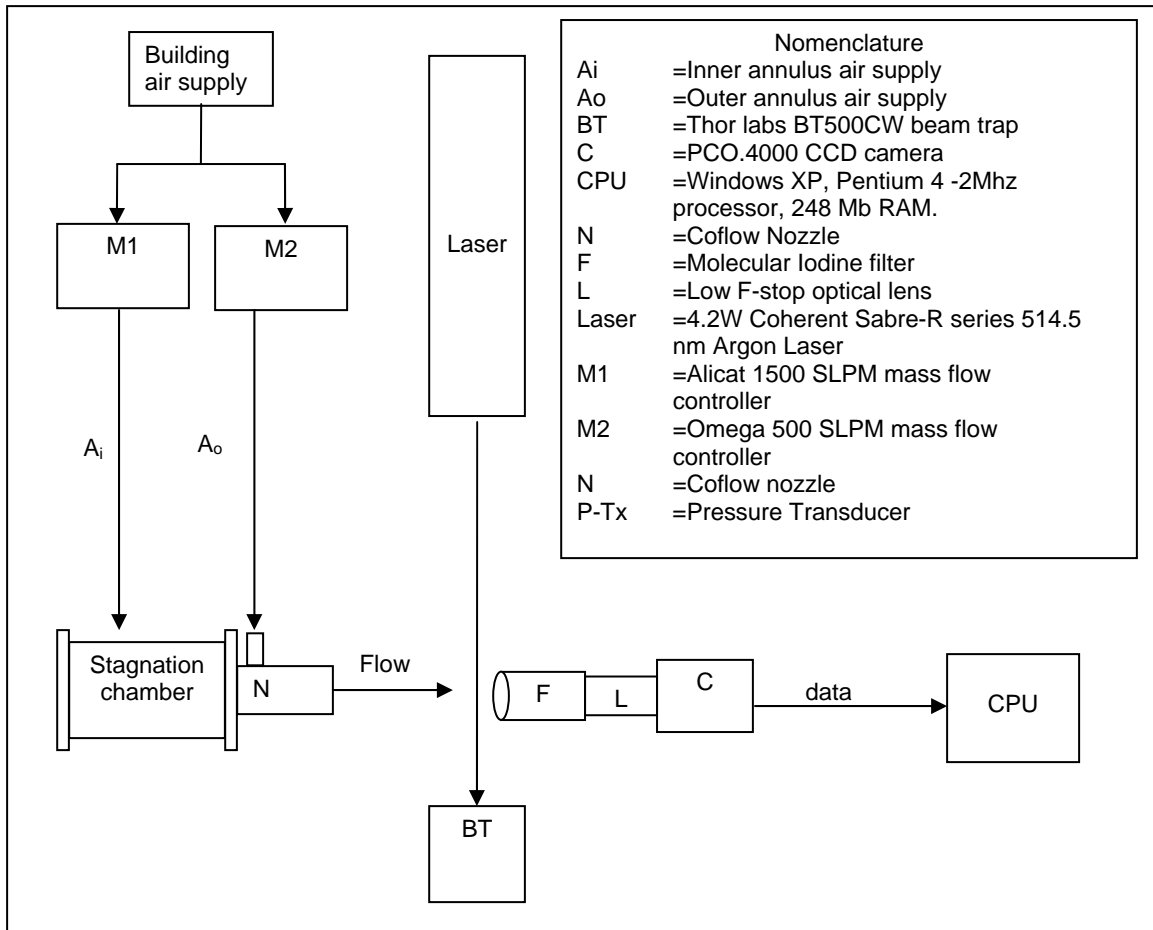
Figure 11- Experimental layout for laser based FRS flow visualizations

Experimental Components

Building air system

Air was supplied via the building compressed air system. The system uses Ingersol Rand screw type compressors with an automatic toggle maintaining pressure between 150-200 psi in an externally stored 6000 gallon tank. The air is dried by a series of two HRM series heatless driers which are preceded by a particulate/coalescing filter.

Beam Trap

The beam trap can increase laser safety by minimizing scattered laser beam energy in the laboratory. Placed in the beam's path, a beam trap absorbs nearly all of the beam energy entering it, thus minimizing backscatter. The Thor Labs BT500CW beam trap allows for a maximum average power of up to 40 watts from 200nm to 1.5μm.

Camera

A PCO.4000 CCD camera was used to capture images of scattered signal from which both qualitative and quantitative data can be extracted in the form of visible trends and received intensities respectively. The camera is equipped with a 4032x2688 pixel charged coupled device that can be used either in monochrome or color mode. Although the camera is capable of receiving several different input triggers to queue exposure, a simple manual acquisition initiation was used in this experiment. The PCO.4000 is capable of high speed recording at exposure times as low as 5μs although at the expense of increased noise. Internal image processing is accomplished through the use of dual digital to analog converters allowing the user the option of single or dual DAC operation. Several different levels of binning are available for image averaging, and all images captured in the following body of work are 2x2 binned. Tagged Image File Format (Tiff or Tif) images were sent to the computer via a firewire cable. The Tiff format was a camera default, although the unit-16 format lends itself well to grayscale images not requiring additional color scales. The camera was equipped with a 105mm Nikon Micro Nikkor f/2.8s lens.

Laser Table

The laser and optics were mounted on a ThorLabs laser table measuring 4'x12'.

The table also includes a passive vibration isolation system intended to remove floor

vibrations in the 10 to 50Hz frequency range.

Nozzle

The jet used in this experiment is an annular coflow nozzle with central jet and

outer annulus areas approximately equal at 1.3 cm^2. The annular nozzle has a blockage

ratio of ~0.87, as defined below in equation 3.1.

$$BR = \frac{D}{D_0} \qquad (3.1)$$

The coflow nozzle was first generated as a Solid Works model. The wireframe of

the model as originally designed is shown below in Figure 12.
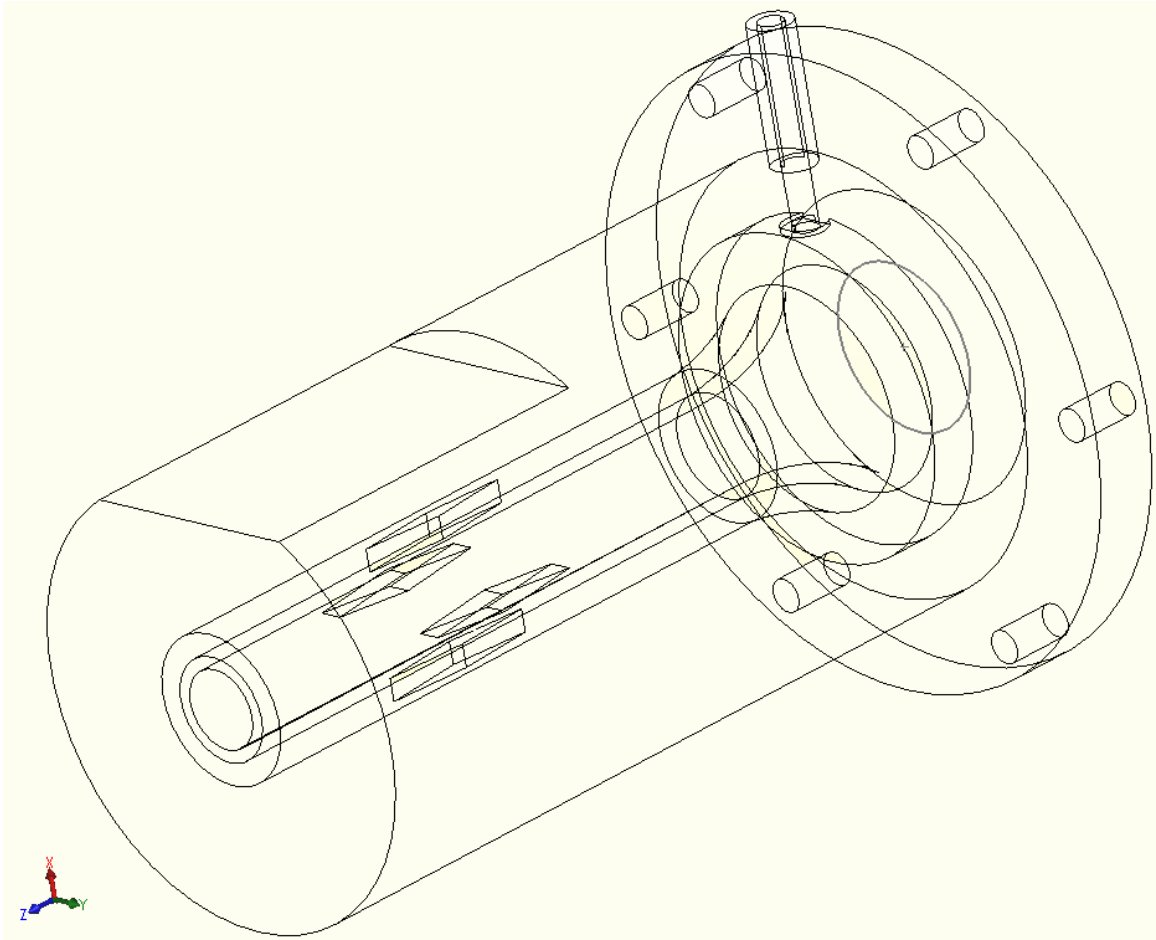
Figure 12- Wireframe view of coflow nozzle

Shown below in figure 13 are two shaded renderings of the nozzle in Solid Works. The rendering on the right shows the four support vanes that run through the outer annulus to the inner. These vanes have a sharp diamond shape and were intended only for support, not to reduce rotation.
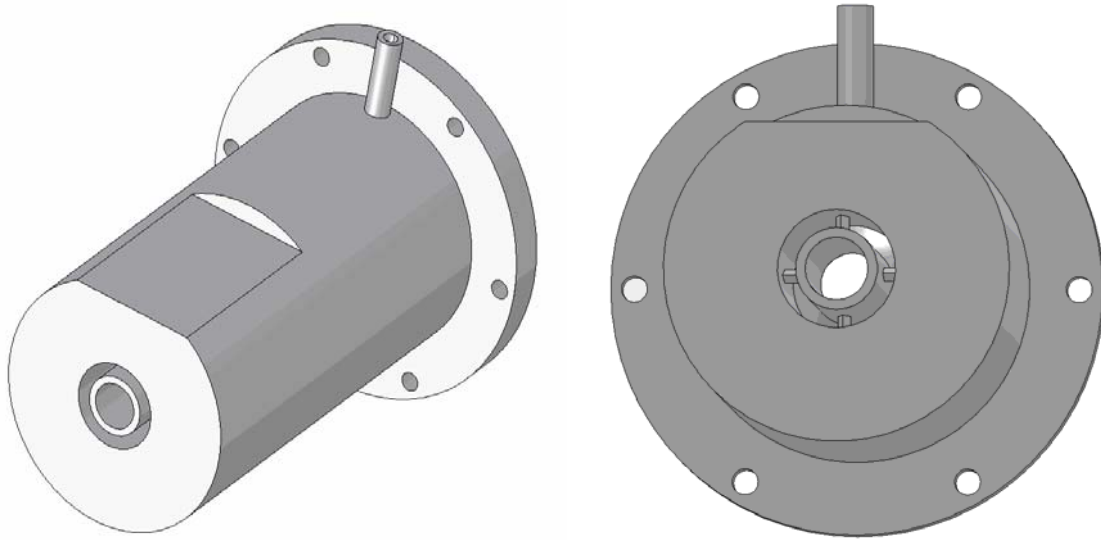
Figure 13- Rendered pictures of coflow nozzle

Both parts of the jet were fed by separate mass flow rate controllers that afforded

the operator the ability to adjust the mass flow rates of the central jet and outer annulus

seperately. The mass flow controller used for the outer annulus is an Omega FMA-2612A

with a maximum flow rate of 500 standard liters per minute. Both the central jet and

outer annulus were supplied by a larger Alicat MCR-1500SLPM-D/5M controller with a

maximum of 1500 standard liters per minute flow rate (SLPM). The larger flow

controller was fed by a stagnation chamber to reduce the effects of fluctuations in

upstream pressure.

The stagnation chamber is used as a buffer to isolate the nozzle flow from any

upstream flow fluctuations either from the mass flow controllers or from the building air

supply. The internal volume of the chamber was approximately four liters.

Because of the design of the nozzle, the outer annulus serves as a buffer between

the static laboratory air and the central jet flow field. Surrounding the central jet with a

separate but slower flow reduces particle entrainment by the central jet. By reducing the

particulate concentration of the inner flow field, the correlative Mie scattering will also be reduced, providing a more pure Rayleigh scattering signal. This is all facilitated by the fact that the building air supply is well filtered and nearly particulate free.

The flow exiting the nozzle was kept well in the subsonic regime, both because supersonic flow was unnecessary, and because of the structural limitations of the plastic nozzle. The obvious benefit, however, of a faster flow is the associated increase in Doppler shift that will facilitate improved resolution. For all calculations it was assumed that the flow was isentropic and fully expanded when leaving the nozzle.

Pitot Probe

The Pitot probe used in this experiment was made from very thin tubing to reduce the influence on the flow and measures 0.5x0.15 mm. This type of probe is typically used to sample boundary layer effects because of its small diameter and shape.

Pressure Transducer

The 10 psig Endevco fast-response pressure transducer connected inline with the Pitot probe was designed to work with flows ranging from zero to five pounds per square inch. It has an accuracy of +/- 0.05 percent and operates at a sample rate of 1kHz.

Three degree wedge

The three degree wedge is an optical lens with a three degree angle separating the front and back plane. This difference leads to the passing light to be split with ~10% of the incident light reflected back three degrees off parallel from the incident light, with the rest of the light passing through in the original direction.   In this experiment it is used as a beam pick off.

Traverse

The traverse was a computer controlled Aerotech A3200 unit that allowed for 32 axis manipulation, although only the three primary axes were used. Although the traverse can be controlled manually through the use of a joystick, it was typically controlled using a Lab View driven graphical user interface that ran user generated programs.

IV. Results

Central jet Flow-External

The first thing to be experimentally tested was the flow field of the inner annulus or central jet. Using the data from the Pitot probe measurements a pressure map was generated. Next, these pressures were converted to velocities by combining two standard isentropic compressible flow equations:

$$\frac{p_o}{p} = \left(1 + \frac{\gamma - 1}{2} M^2\right)^{\frac{\gamma}{\gamma - 1}}$$
(4.1)

$$a = \sqrt{\gamma R t}$$
(4.2)

By combining these two equations and solving for velocity yields:

$$V = \sqrt{\frac{\gamma R t \left(\frac{p_o}{p}\right)^{\frac{\gamma - 1}{\gamma}}}{\frac{\gamma - 1}{2}}}$$
(4.3)

To check for accuracy, the compressible flow equations were compared to Bernoulli's equation for incompressible flow:

$$q = \frac{1}{2} \rho v^2$$
(4.4)

When the nozzle was run at a low mass flow rate and resulting maximum velocities were less than the accepted Mach number 0.3 transition to compressible flow, the two equations resulted in less than one percent difference. As the mass flow rate for the central jet flow was increased, the deviation between the incompressible and compressible flow solutions also increased as expected. It was important to know the

36

velocities of the nozzle flow field because these velocities determine the amount of Doppler shift the laser light will encounter.

Although while generating flow visualizations both the central jet and outer annulus flows will be running at the same time, this portion of testing was only to check for flow asymmetry or other unexpected problems. Because of this, the central jet flow was tested independently of the outer annulus flow. The experimental results of the central jet field were as expected; the flow was nearly axisymmetric and slowed slightly near the wall due to boundary layer effects. The strong adverse pressure gradient near the edge of the flow caused an area of separation and reversed flow around the central jet. As the flow progressed down stream of the nozzle, it diverged but remained rather symmetric. The data shown below is of the central jet flow at a mass flow rate of 750SLPM at the exit plane.
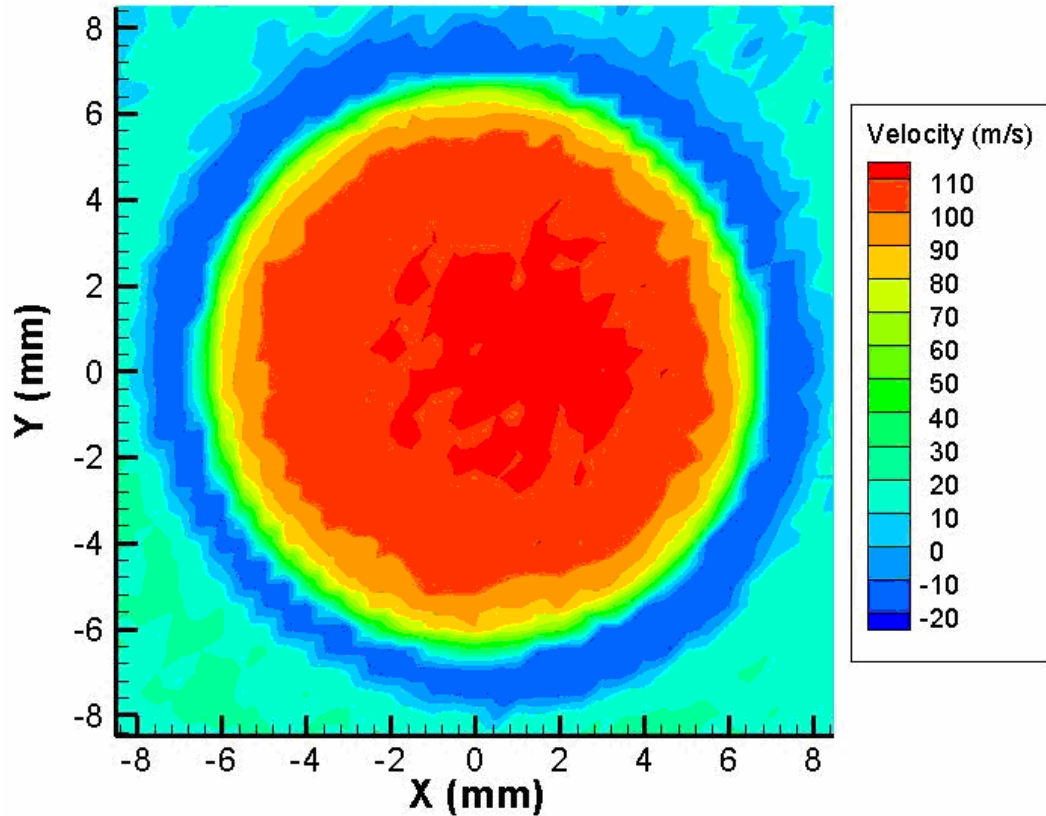
Figure 14- Experimentally determined flow field for 750 SLPM central jet flow.

Outer annulus Flow-External

Although the results of the inner flow field were as expected, the experimentally determined velocity profile when the air only flowed through the outer annulus was unexpected. The expected result was an axisymmetric flow field centered on the long axis of the nozzle with a layer of slower flow on both the inner and outer walls due to boundary layer effects. Although the experimental radial flow profile confirmed the expected outcome, the flow was far from axisymmetric. At the exit plane there was a strong bias towards the side of the annulus opposite the injection port. Shown below in Figure 15, is the experimentally determined velocity profile at the exit plane of the outer

38

annulus without central jet flow. The data was recorded in a 0.25mm^2 grid with the mass flow controller set at 500 SLPM.
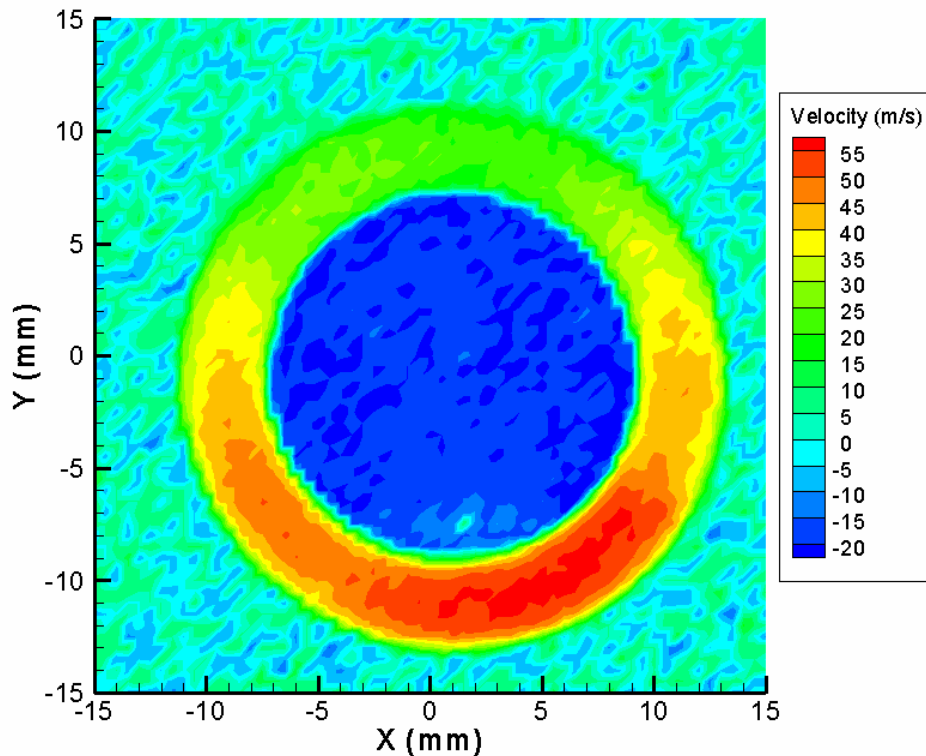
Figure 15- Velocity profile at the exit plane of the nozzle at an outer annulus flow rate of 500 SLPM. The air intake tube is situated opposite the side of high flow velocity; reference Figure 12 for nozzle geometry.

The experimental data clearly showed a very strong bias towards the side of the exit plane directly opposite the injection port of the outer annulus. There was as much as a 50% flow differential in flow velocities exiting the upper and lower portion of the outer annulus. At this point, experimental testing of the outer annulus was halted to determine the source of this flow asymmetry. The asymmetry could have been caused by several different phenomena.

First, the injection port could have been off axis and imparted the flow with a rotational velocity that propagated downstream in the annulus. Although this is possible,

the existence of four stability/guide vanes in the annulus somewhat discredit this theory. Ideally, the vanes would deny the existence of a strong rotational flow, but their influence in this particular case was still unknown. In addition to this, the nozzle was built using a computer controlled three dimensional printing process that yields highly accurate models and such an inaccuracy is unlikely.

Another possibility is that when the flow exits the intake pipe, it behaves as it were flowing through a sharp bend in a pipe; the flow near the large radius turn retains more of its momentum compared to the short radius flow. The inner radius flow separates from the wall causing an area of recirculation. The faster flow would propagate towards the bottom half of the annulus whereas the slower flow on the inside of the bend would propagate towards the top half of the annulus. This is analogous to a river bend that continues to erode the river bank on the outside of the bend, where the flow is moving faster (Prandtl).

The next possibility is the existence of some support material remaining in the outer annulus. When the nozzle was built using the three dimensional printing process, there are two different materials used. The first material is a plastic used to generate the solid portion of the nozzle which remains after the process is complete. The second material is a support material that replaces the eventually hollow areas of the model. As each layer of the model is printed, the plastic is injected onto the future solid areas and the support material is injected onto the future void spaces. When the process is complete, a solid block exists consisting of both plastic and support material. The support material is separated from the plastic with a high pressure water stream sprayed both on the outside and into the internal cavity of the nozzle. To remove any remaining

support material, the entire block is soaked in a special solvent for an extended period of time. After soaking in the solvent, any remaining support material should be easily removed using the high pressure water leaving only the plastic nozzle originally modeled in Solid Works. Although this is the ideal case, it was possible that some of the support material did not fully dissolve and remained inside the outer annulus. This remaining support material could have been the cause for the flow asymmetry.

A final cause could have been that the inlet pipe for the outer annulus was too small for the desired mass flow rates, and the flow was being choked. Immediately after the inlet pipe where the area rapidly increased, the flow could have become supersonic, causing a series of shock interactions. These shock interactions could be responsible for the asymmetry downstream.

Although all of these theories underlying the flow asymmetry are viable they lacked any sort of computational or experimental support. To remedy this, the model was analyzed using computational fluid dynamics.

CFD Analysis of Outer Annulus- Internal

Computational fluid dynamics requires that the shape being analyzed is partitioned into a grid with sufficiently small spacing to allow for calculations of flow properties. The first step in generating this grid is to build a computer model of the object to be analyzed. Although this step can be done in several different programs, the nozzle was modeled in Solid Works. The existing Solid Works model used to create the coflow nozzle in a 3-D printer was imported into a program called Gridgen, and the resulting database is shown below in Figure 16.
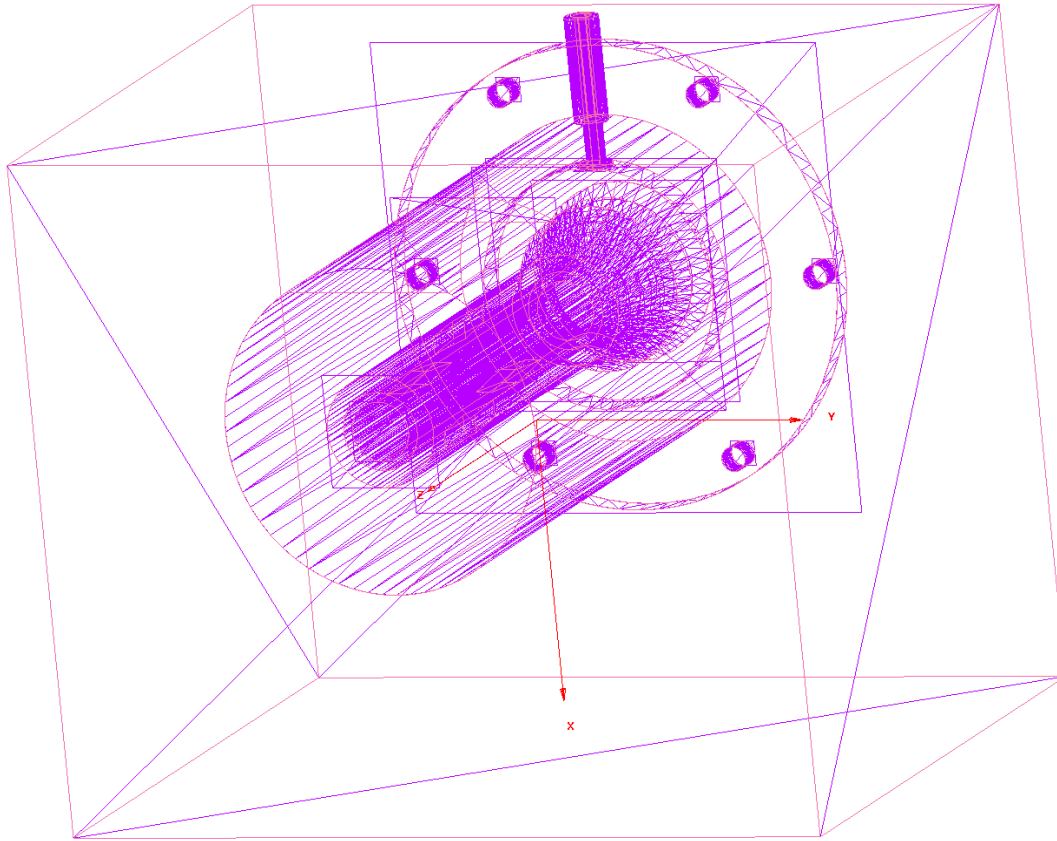
Figure 16- Gridgen model imported from Solid Works

The next step was to remove all the parts in this model that do not contain or

affect the path of the airflow. Because the final product will be a finely meshed grid,

including unnecessary objects will only increase the file size and slow calculations. Once

the unnecessary parts were removed from the nozzle, only the outer annulus and intake

tube were left.

The next step was to generate connectors on top of the database entities shown in

the above figures. This step creates the outline for the mesh to build upon later on in the

process. This results in an overlay of the original database with connectors. After

creating connectors on top of all database entities, the next step is to manually connect

the curves that are not already connected.

Once all the connectors were generated, they needed to be partitioned into smaller segments or dimensioned. The connectors were broken up into equal spaced segments at a consistent size throughout the model. This consistency was chosen because at the onset of the process there was no clear reason for the flow asymmetry, and therefore there was no region that required additional grid definition, other than the nozzle exit plane and guide vanes. The grid density was increased for the nozzle outlet to generate a clearer picture of the exit plane flow field whereas the density was increased on the guide vanes because of their impact on the flow downstream. The ΔS values were set at 0.025 inches for all surfaces except the guide vanes and outlet plane which were set at 0.02 inches.

The lines and curves of dimensioned connectors were linked together to form flow boundaries called domains. Each domain is an infinitely thin portion of the shell of the nozzle, and is assigned a boundary definition for its role in the model. Domains that, when fitted together, form the solid portion of the nozzle walls, guide vanes, and air inlet pipe are defined as walls. The working fluid, in this case, air, cannot pass through these wall boundaries. The walls also have material properties such as roughness and thermal conductivity that affect the flow. The domains that cover the open part of the air inlet pipe are defined as a mass flow inlet surface. Similarly, the domains that cover the exit plane of the nozzle are defined as a pressure outlet. All domains in the Gridgen model for the nozzle were unstructured, meaning they were manually generated by forming a closed loop system around the border of the model. The closed loop was then filled with triangles, as opposed to a structured domain that would be filled with a parametric or parametric fit transfinite interpolation (Gridgen).

To determine whether the flow is turbulent or laminar, the flow Reynolds number must be calculated and compared to the critical Reynolds number of 2,300 for pipe flow. If the flow has a Reynolds number greater than 2,300 it is typically considered turbulent and if it is less than 2,300 it is typically considered laminar (Schlichtin and Krause). To determine the Reynolds number for the outside annulus, the following equations were applied.

$$\text{Re}, crit = 2,300 = \frac{u_m d_h}{\nu} \qquad (4.5)$$

$$d_{hydraulic} = d_2 - d_1 \qquad (4.6)$$

Because the outer annulus outer diameter is 24.4 mm and inner diameter is 21.21 mm, the mean velocity would have to be less than ~12.48 m/s for the flow to remain under the critical Reynolds number. With a mass flow rate of 500 SLPM, the average velocity at the exit plane of the nozzle was ~35 m/s and with a mass flow rate of 250 SLPM, the average velocity was ~18 m/s, yielding Reynolds numbers of ~6453 and ~3319 respectively. In both cases the Reynolds number was beyond 2,300 and therefore the outer annulus would be most accurately modeled as a turbulent flow in Fluent.

Because the model was to be analyzed as a turbulent flow, the flow interaction with the boundary surfaces is of heightened importance. However, boundary areas did not require additional cell density because the wall functions intrinsic to Fluent resolve the boundary layer and turbulence effects in these regions. The wall functions do this by using semi-empirical formulas to bridge the region between the wall's no slip condition and the turbulent flow (Fluent). Because of the wall functions, the boundary influence parameter was set at 0.95, which meant that the grid did not significantly tighten at the

domain interfaces. Shown below in Figure 17 is a picture of the Gridgen model with

some of the domains blanked for clarity.
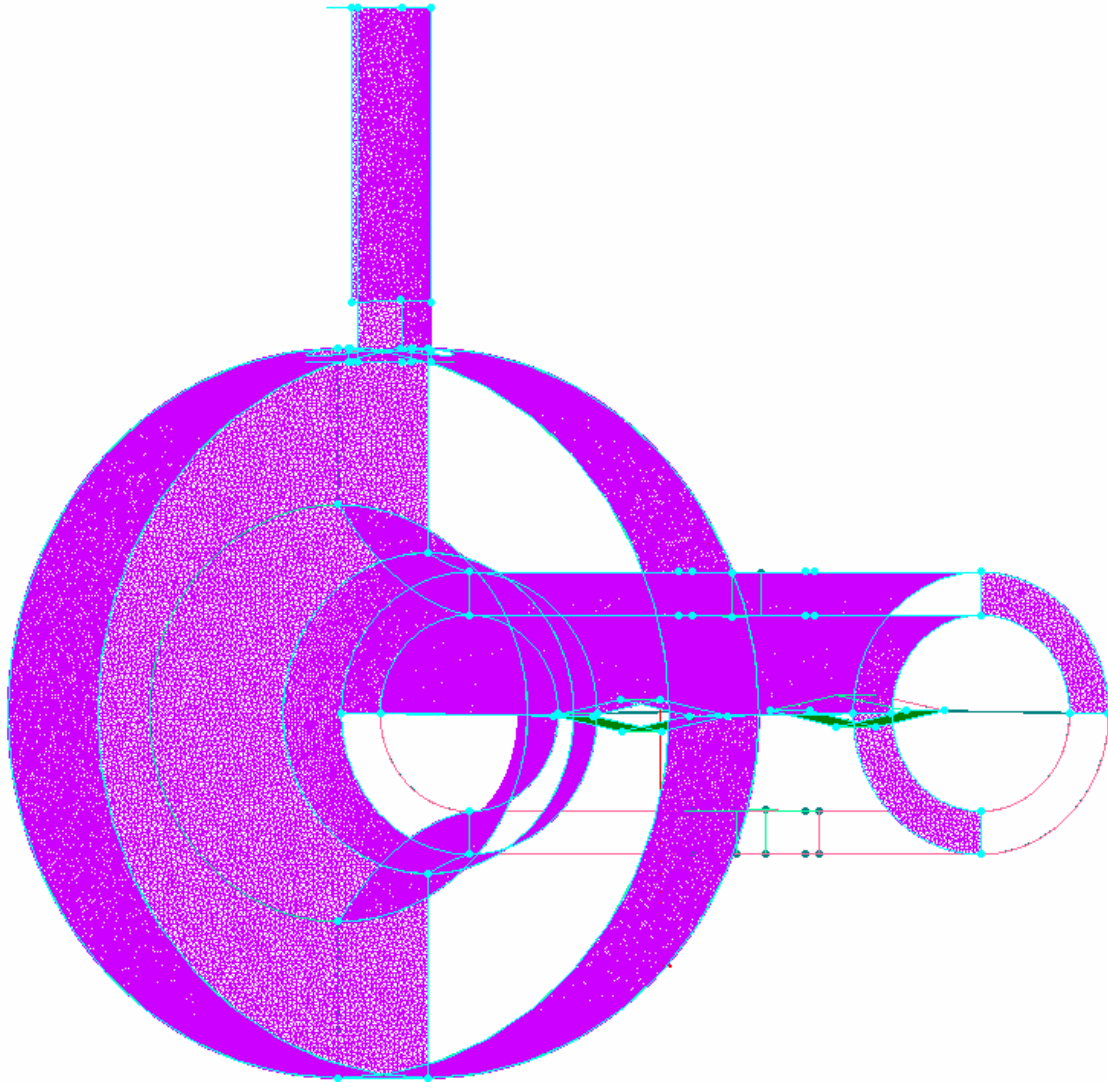
Figure 17-Cutaway Gridgen model showing selected domains

      After defining the domains, the next step was to join the edges of the domains

together forming a hollow, water-tight block. Blocks make up the volume through which

the working fluid passes in the CFD solver. Once the block has been generated, the next

step is to run the unstructured solver in Gridgen which generates the tight grid of three

dimensional cells that fill the volume of the block. Anywhere the air may flow inside the

volume of the nozzle is filled with cells. The final result of this process is a grid of the internal flow path of the outer annulus composed of 3.3 million cells filling the 42.0 cc volume. Show below in Figure 18 is a cutaway of the entire nozzle with one plane of cells shown in each of the primary axis.
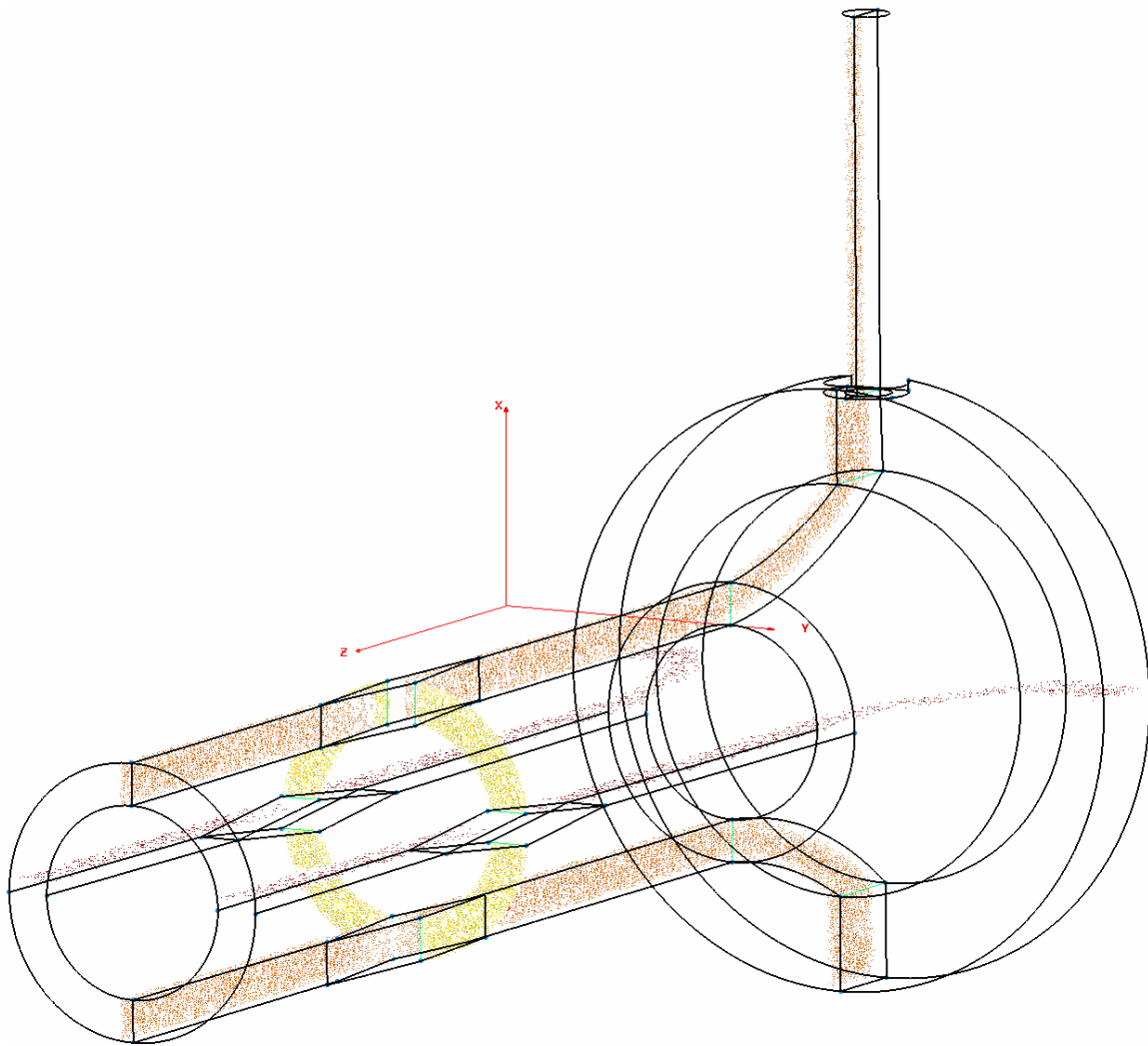
Figure 18- Gridgen model showing the three axis cell distribution of the Gridgen model.

Figure 19 shows a zoomed view of the cell distribution in the region surrounding one of the guide vanes in the outer annulus. Each different color represents a slice of the internal grid along the three primary axes of the nozzle. Note how the cell density is consistent among all three primary axis directions, and all cell faces are composed of

nearly equilateral triangles. Although this is not a necessity, it reduces cell skewness which and increase model accuracy.
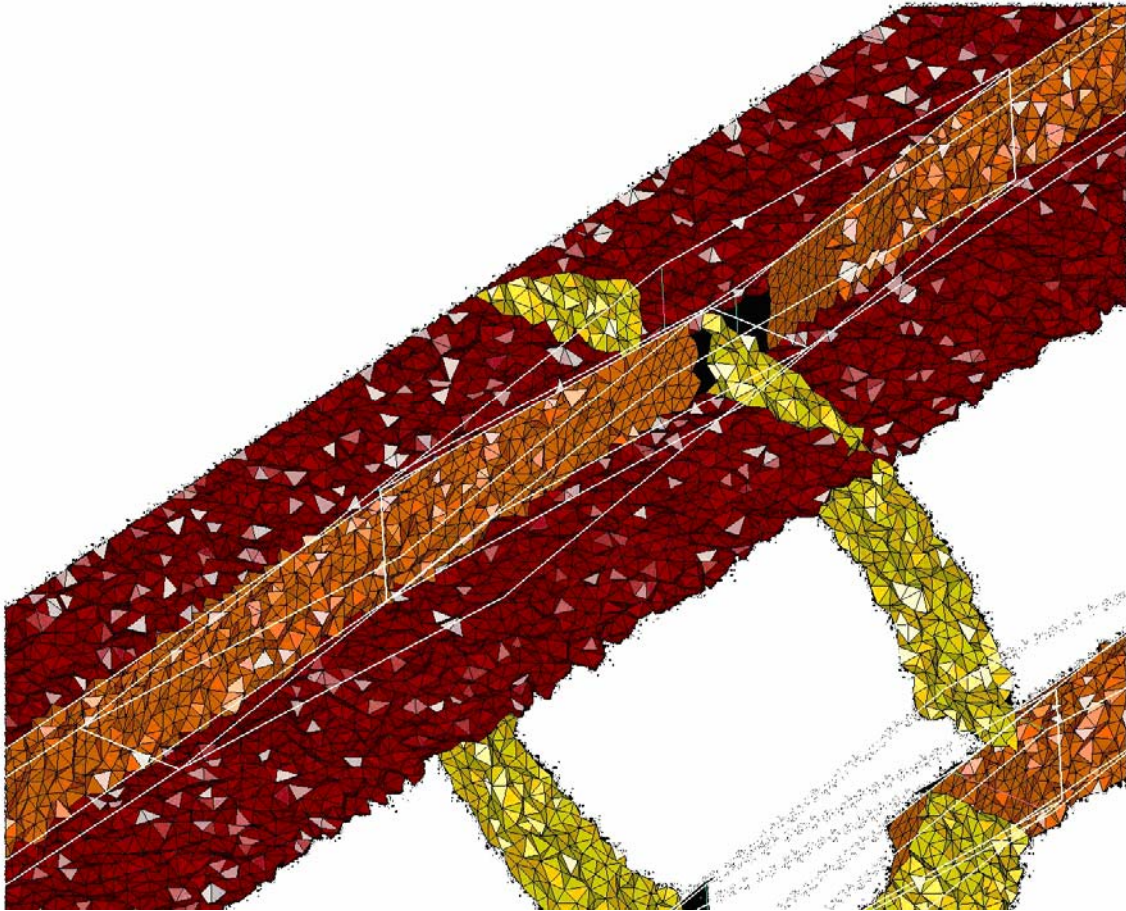
Figure 19- Close in picture of the cell distribution of the Gridgen model around a support vane.

The number of cells is related to the dimension of the connectors making up the domains and is a critical element of the process. Having too few cells will result in a coarse mesh that will not allow for accurate calculations. Conversely, too many cells will lead to an overcomplicated model and that would unnecessarily slow calculation times. Although the number of cells is related to the dimension of the connectors, it is ultimately driven by the characteristics of the flow and model. Laminar, incompressible flows are

less complicated computationally and require fewer cells than a turbulent, compressible flow.

The viscosity model used was a two equation, κ-ε turbulence model. Although there are several ways for the user to input the initial values for ε and κ, the option most applicable to this model was to input the turbulence intensity and hydraulic diameter for both the mass flow inlet and pressure outlet. In both cases the hydraulic diameter was set at 0.125 inches and the turbulence intensity was calculated based on their Reynolds number using equation 4.7 (Fluent).

$$I \approx 0.16(Re_{,h})^{-1/8} \tag{4.7}$$

The turbulent intensities for the mass flow inlet and pressure outlet were 3.67 and 5.37 percent respectively. Although different values for the turbulence intensity were tried, they had very little impact on the final solution.

After having run several cases in Fluent using different roughness models, it was discovered that the texture of the model has a great impact on the computational solution. The nozzle was made from a three dimensional printing process that produced a ribbed texture on the nozzle surface. When the three dimensional printer generated the nozzle, it built up layers of material on the X-Z plane. After each plane was complete, the Y value was increased and another X-Z plane was laid down. This process resulted in a model textured with equally spaced ridges progressing along the Z axis. Since the Z axis is the primary flow direction for air in the nozzle, this texture could have a significant impact on the flow characteristics.

The actual plastic coflow nozzle was ridged as a result of the three dimensional printing process, but had been modeled in Fluent as smooth. To remedy this, the

boundary conditions for the walls were updated to include a roughness height of 0.5

mm. This number is an estimation of the height of the ridges on the nozzle. Related to

the roughness height is the roughness constant that takes into account the pattern or shape

of the roughness. Although the Fluent user's manual suggests that roughness constants

for ribs, such as the texture of the nozzle, can range from 0.5 to 1.0, it was left at the

default level of 0.5. This choice was made because there was no guidance for varying the

roughness constant. The lack of roughness in the original Fluent models could have lead

to a lack of flow turbulence, especially around the support vanes of the outer annulus.

The last Fluent parameters that were altered were the under-relaxation parameters.

The under-relaxation parameters are a way to deal with the non-linearity of the equation

set being solved. Each iteration, the under-relaxation parameters limits the change of the

variable, φ, by a user-defined parameter as shown below in equation 4.8 (Fluent).

$$\varphi = \varphi_{,old} + \alpha\Delta\varphi \qquad\qquad (4.8)$$

Although a decrease in under-relaxation parameters increases the computation

time to arrive at a solution, it also increases the chance that the parameters will converge

to an accurate solution. Shown below in Table 1 are the default and altered under-

relaxation parameters.

Table 1- Tabulation of Fluent under relaxation parameters.

Parameter	Default	Altered
Pressure	0.3	0.3
Density	1.0	1.0
Body Forces	1.0	1.0
Momentum	0.7	0.7
Turbulent Kinetic Energy	0.8	0.25
Turbulent Dissipation Rate	0.8	0.5
Turbulent Viscosity	1	0.5
Energy	1	0.5

With these parameters set at their default level, the solver encountered many reversed flow faces on the pressure outlet, and many cells that exceeded the maximum turbulent viscosity. Because of this, the solution rarely converged, and did so with peculiar results. To remedy this situation, the under-relaxation parameters were dropped from the default level to the level recommended by the user's manual for turbulent flows that are having difficulty reaching a plausible solution. By dropping the under-relaxation parameter values as indicated, the solver could avoid the errors it encountered previously and converged to a solution. For the turbulent case with ~3.3 million cells, the solver iterated 790 times before all parameters were considered converged. The convergence criteria are listed below in Table 2.

Table 2- Tabulation of Fluent convergence criteria

Parameter	Convergence Criteria
X-Momentum	1e-3
Y-Momentum	1e-3
Y-Momentum	1e-3
Energy	1e-6
Continuity	1e-3
E	1e-3
K	1e-3

Once the flow solution was determined using the correct roughness factor and updated under-relaxation parameters, the results could be analyzed. By examining the particle paths in Fluent, the reasoning for the flow asymmetry was readily apparent. When the air exited the inlet pipe, most of it followed one of two patterns. Some of the flow exited the pipe and began circulating in the top half of the stagnation volume directly adjacent to the pipe exit. Particles that entered this path remained there for several circulations as their velocity slowly reduced. This behavior can clearly be seen in Figure 20 below. Although the flow pattern is still evident in Figure 20, Figure 21 has rescaled velocity contours to highlight the flow variances in the region of recirculation.
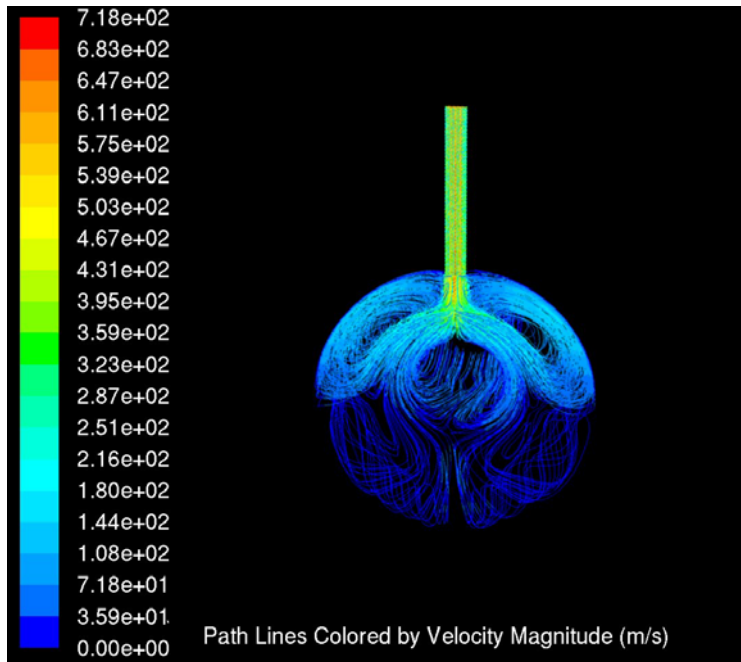
Figure 20- Unscaled back view of original nozzle outer annulus internal flow field at a flow rate of 500 SLPM
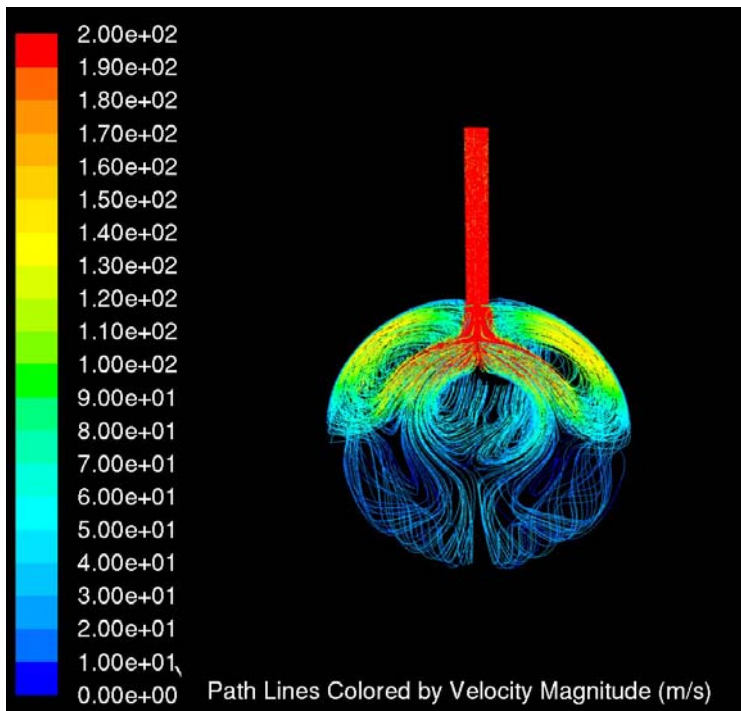
Figure 21- Scaled back view of original nozzle path lines showing the circulation in the stagnation volume at a flow rate of 500 SLPM

Notice how the particles enter the circulation pattern at over 200 m/s but slow to below 100 m/s by the time they begin to move downstream along the upper side of the annulus.

The other flow pattern shown above was for the air molecules to exit the inlet pipe and travel circumferentially around the inner wall of the annulus while also moving downstream. After moving to the side of the annulus opposite the inlet pipe, these air molecules head downstream without circulating in the XY plane like the other molecules did. This is illustrated in Figure 22 below.
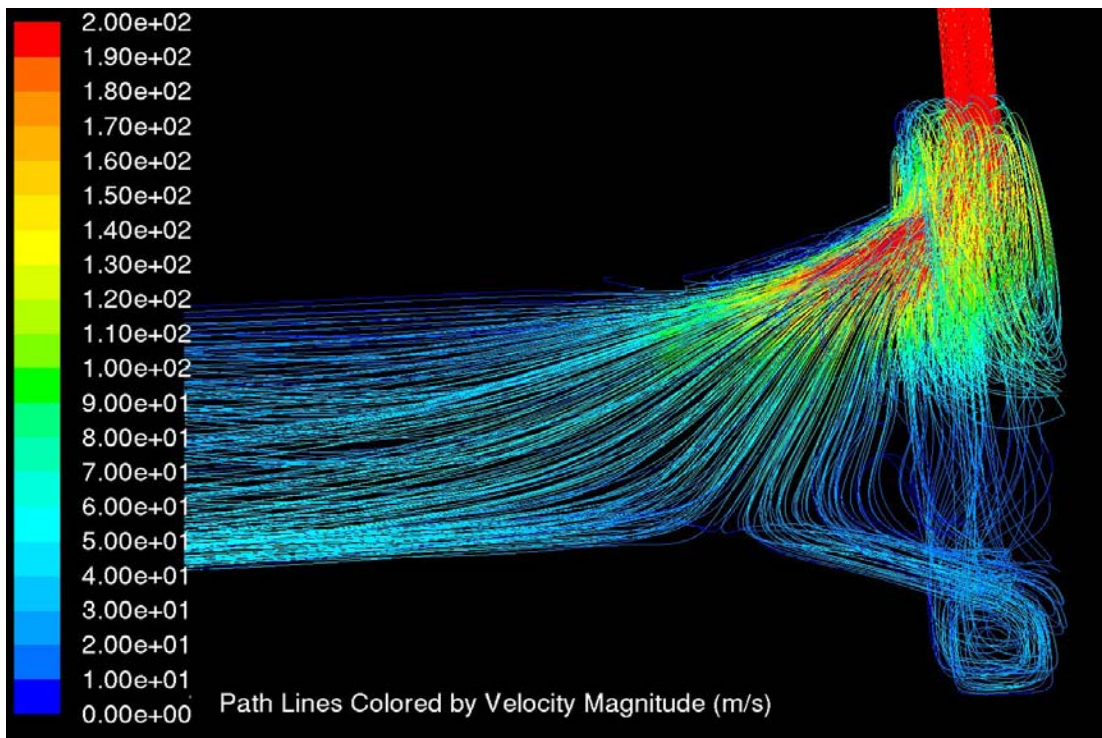
Figure 22- Side view of nozzle path lines showing the disproportionate amount of fast air moving towards the bottom part of the outer annulus compared to the upper while operating at a flow rate of 500 SLPM.

Notice how the path lines heading towards the lower side of the annulus show a higher velocity than those in the upper half. Most of the path lines traveling towards the bottom half enter the annulus at over 200 m/s, nearly 100 m/s faster than the molecules

that circulated in the upper half of the diffuser. The molecules leading to the lower half of the annulus clearly have a more direct path to the nozzle outlet and exit at a higher speed than the molecules on the upper half of the annulus. This flow pattern can be compared to that of a 90 degree bend in a pipe, the flow on the outer portion of the bend typically moves faster than the flow on the inner wall of the bend. The resulting markedly different flow patterns for the upper and lower sides of the annulus are what leads to the flow asymmetry at the exit plane. This flow asymmetry that was first seen experimentally was recreated computationally, as shown below in Figure 23.
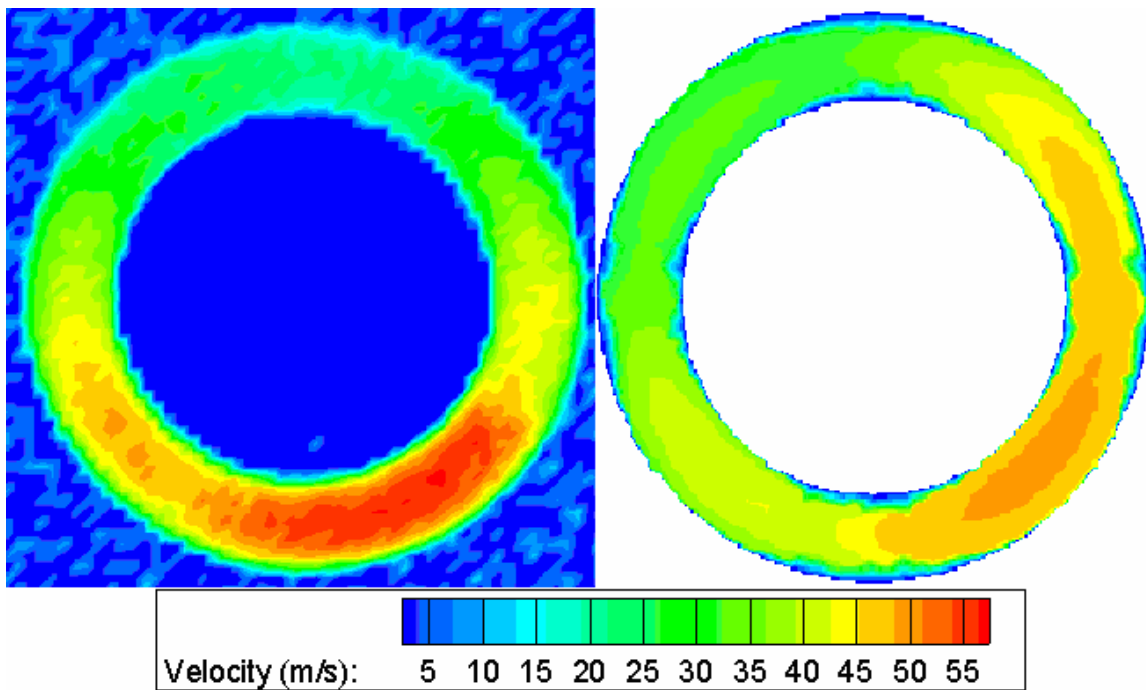
Figure 23- Comparison of experimentally to CFD resolved velocity profiles at the exit plane of the outer annulus while operating at 500 SLPM. The recirculation zone inside the outer annulus is not shown here because the Fluent model is only showing the flow at the exit of the annulus, not the resulting external flow field. Both images use the same contour scale.

Not only are the velocity magnitudes profiles very similar, but so are the flow asymmetries. Because the flow is nearly axial at the exit plane of the nozzle, there is no

reason to extend the CFD analysis downstream. The area of interest is the exit plane and adding the entire flow field to the CFD analysis would be computationally difficult and unnecessary.

Redesign and CFD Analysis of the Outer Annulus- Internal Flow Field

Once the reason for the asymmetric flow at the exit plane of the outer annulus was determined, the next step was to devise viable solutions to the problem. The goal was to eliminate the existing flow asymmetry and produce a consistent flow field at the coflow exit plane.

One way to combat the problem would be to add another air inlet pipe to the coflow nozzle directly opposite the current pipe. The goal of this is to reduce the asymmetry caused by the flow entering only one side of the diffuser. Although this may eliminate the current asymmetry, it could also produce flow patterns that cause different asymmetries. In addition to this, the addition of another air inlet pipe would further complicate the experimental setup. Not only would the air line running to the initial air inlet pipe need to be split, but both air lines leading to the intake pipes would have to be of the exact length. This would ensure that any pressure fluctuations upstream of the tee would reach the intake pipes at the same time.

Another possibility was to increase the size of the air inlet pipe to reduce the inlet flow speed. By slowing the inlet flow, the influence of the bend would not be as pronounced. In addition to slowing the incoming flow, the stagnation volume could also be enlarged to allow more settling time to equalize pressures. This approach to the problem would not require augmentation of the current experimental setup other than replacing the current nozzle with a new one.

54

In addition to the changes in model design, the model building material and process were also changed. The three dimensional printer used to generate the first nozzle would be replaced with one more capable. The result was a decrease in roughness coming from tighter printing definition and a change in structural material.

Because it was the option that would require the least changes to the experimental setup, and because of the simplicity of the changes, the second option was selected. The coflow air inlet pipe inner diameter increased from 1/8 to 3/8 inches. This increased the area nine fold, while slowing the incoming velocity by approximately the same ratio. Also, the diffuser was increased in volume approximately five fold over the initial design.

Once the nozzle was redesigned in Solid Works, it, had to be imported into Gridgen to produce the internal grid before being analyzed in Fluent. Following the same procedures as with the previous nozzle, the new nozzle was run in Gridgen and the resulting grid contained 3.2 million cells. The approximately three percent deviation in cell count between the old and new nozzles came from the variances encountered while trying to block the model. The old nozzle needed multiple grid refinements around certain trouble areas for the domains to become watertight; fortunately the new model did not require this and therefore, has slightly fewer cells. Shown below in Figure 24 is a zoomed in view of the cell distribution in the region surrounding one of the guide vanes in the outer annulus. Again, cell density is consistent among all three primary axis directions, and all cell faces are composed of nearly equilateral triangles.
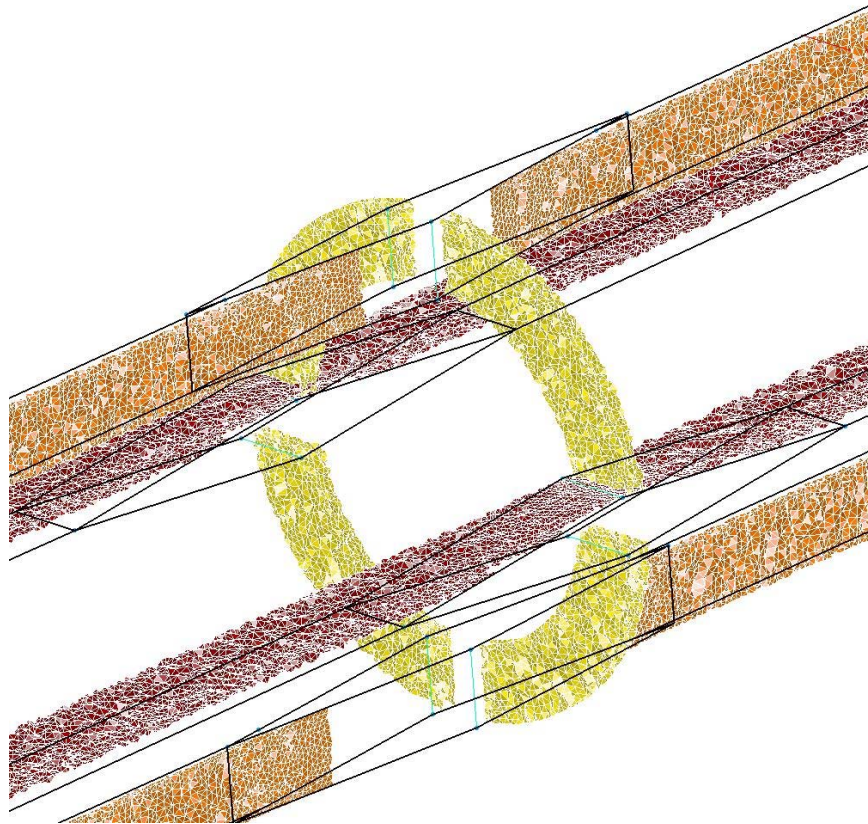
Figure 24- Close up view of the CFD cell distribution in the outer annulus of the nozzle. A slice of the three primary axis are shown around the wedge shaped guide vanes.

Before the model could be imported in to Fluent, the boundary conditions were set in Gridgen. Because the experimental conditions have not changed, all boundary conditions remained the same as they were for the first nozzle. In Fluent however, some values had to be updated to remain consistent with the new model. The hydraulic diameter increased to 0.375 inches and the turbulence intensity decreased to 4.35 percent for the mass flow inlet.

To test the influence of the model roughness in Fluent, cases were run using a roughness height and coefficient corresponding with both of the three dimensional printers. Because the higher definition printer produces a smoother nozzle, the resulting roughness height was dropped to 0.1mm, although the roughness coefficient was left

unchanged. This is because the printing process still generated a patterned or ribbed

texture similar to the initial nozzle texture.

Once the simulations were run comparing the two types of three dimensional

printers, the results showed that the flow at the exit plane was not greatly affected by the

change in internal roughness. Although the magnitudes of velocity at the exit plane

varied slightly, the overall flow pattern was invariant.

Shown below in Figure 25 is the computed velocity profile at the exit plane of the

outer annulus of the redesigned nozzle.
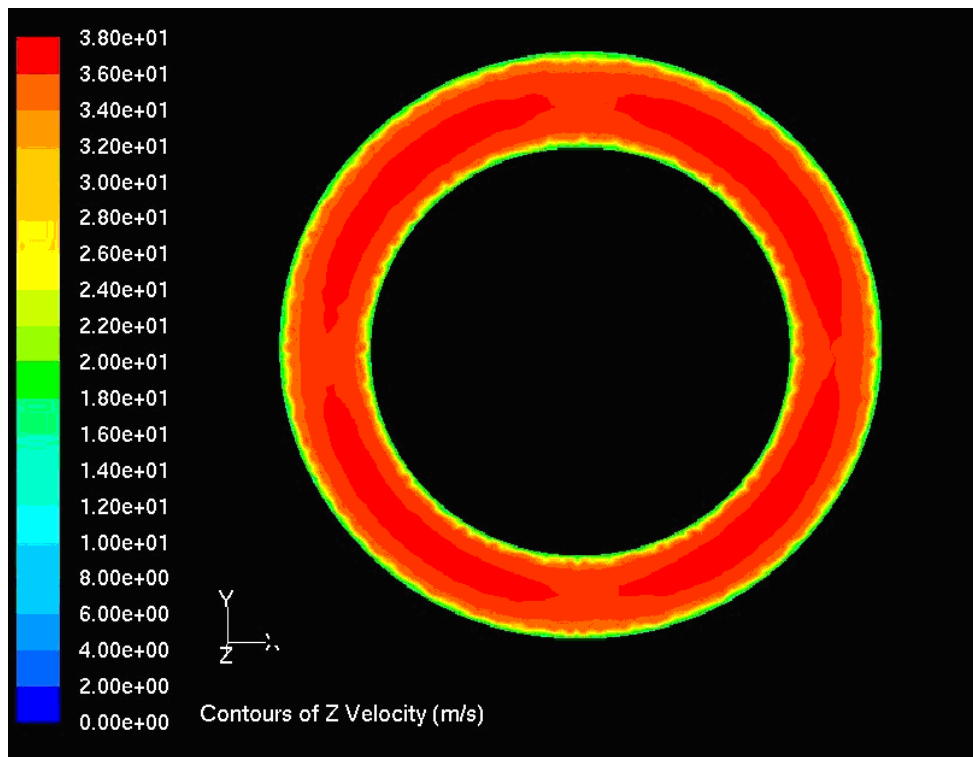
Figure 25-CFD resolved exit plane velocity profile of redesigned coflow nozzle operating at a 500

SLPM outer annulus flow rate.

Clearly the redesigned nozzle eliminated the asymmetry found in the initial

nozzle. The exit plane velocity distribution is the result of the elimination of the

undesirable internal flow patterns found in the original nozzle. Shown below in Figure

26 is the back view of the internal flow pattern.
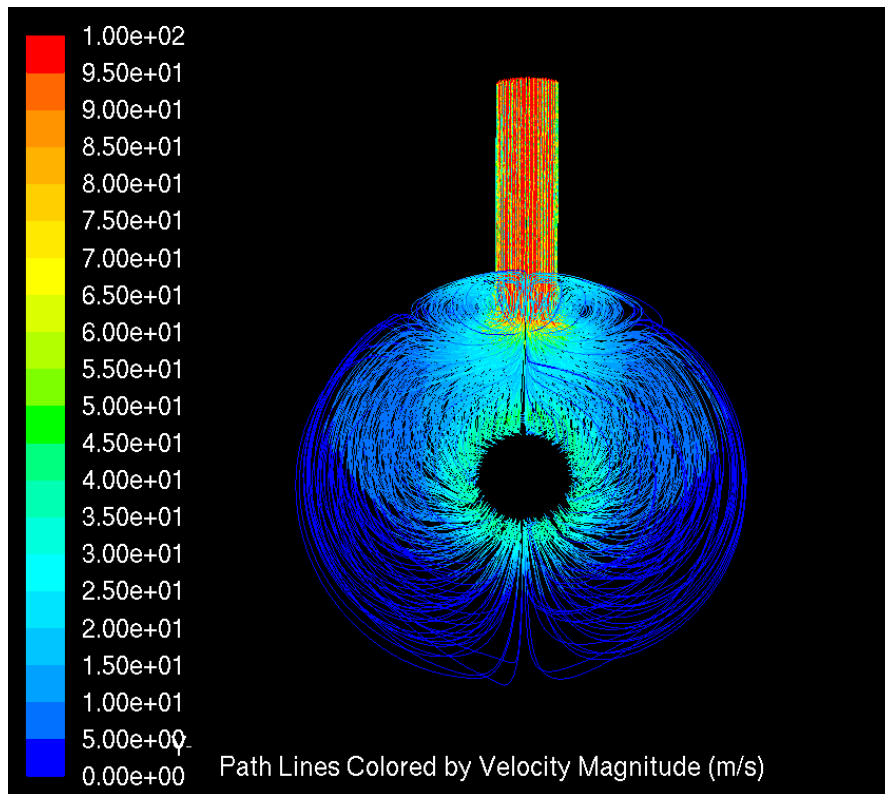
Figure 26- Back view of redesigned nozzle path lines showing the slower velocities and improved flow in the settling area while operating at a 500 SLPM outer annulus flow rate

As shown by the path lines above, the combination of slower intake velocity and

increased stagnation volume allow for the incoming air to settle before flowing

downstream. There is no circulation pattern in the X-Y plane as in the previous nozzle.
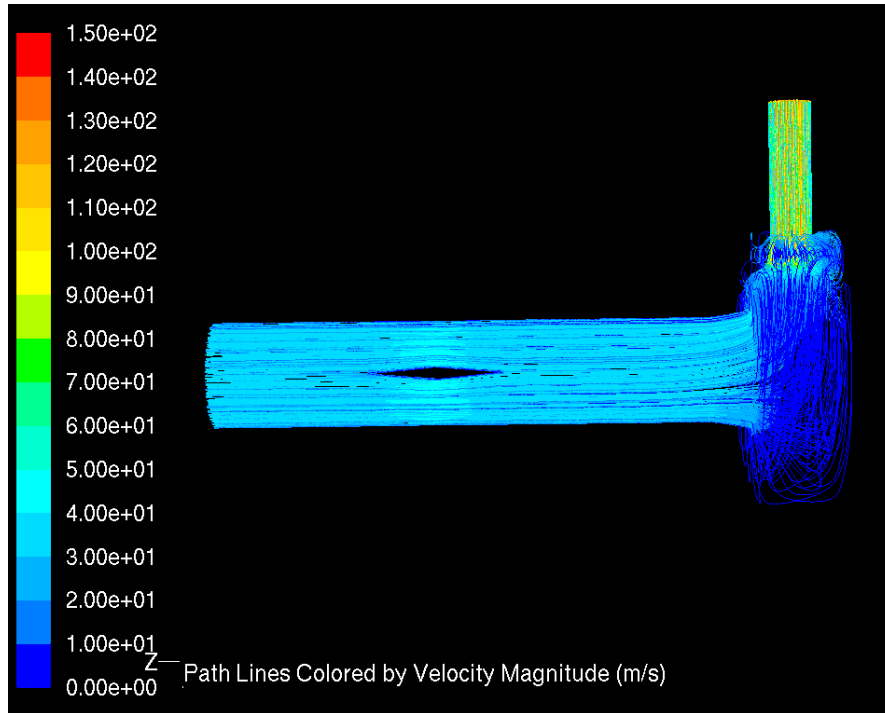
Figure 27- Side view of the redesigned nozzle velocity path lines showing the symmetry of the flow entering the outer annulus operating at a 500 SLPM outer annulus flow rate

The side view of the nozzle above in Figure 27 shows the symmetry in flow velocity entering the annular portion of the nozzle that was not present in the initial nozzle. In addition to this, the flow field in the settling area is much slower and evenly distributed in the redesigned nozzle. Because the theoretical redesign seemed to solve the initial problems, the new nozzle design was built in a Statasys Eden 333 three-dimensional printer.

Redesigned Outer annulus Flow- External

Now that the nozzle had been redesigned and proven viable computationally, the next step was to print and test the model. The new three dimensional printer yielded a smoother nozzle that was tested in the same manner as the initial nozzle. When the new nozzle was tested at a mass flow rate of 500 SLPM the resulting velocity profile was

fairly axisymmetric and clearly more homogeneous than the original nozzle. The Fluent

solution compared well with the experimentally determined data as shown below in

Figure 28. The redesigned nozzle had a maximum flow asymmetry of approximately

1.25:1 compared to 2:1 for the original nozzle.
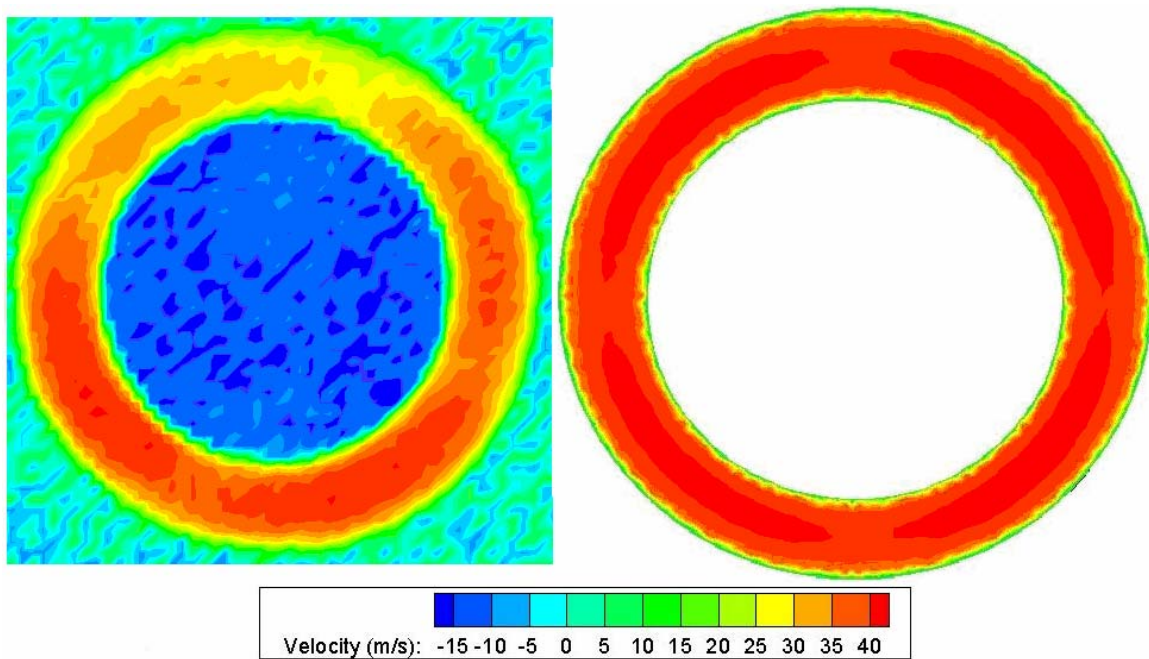
Figure 28- Comparison of experimentally determined to CFD results for the outer annulus exit plane velocity profile at 500 SLPM.

Although the nozzle produced a generally axisymmetric flow field there was a

vane influence that was not as prevalent in the CFD model. This can be seen in the areas

of slower flow directly downstream from the internal support vanes. The approximately

10% difference between the CFD analysis and experimentally determined flow velocities

may be the result of a change in model material and building process. The redesigned

model used a more accurate three dimensional printer that yields smoother products.

Because the nozzle support vanes are smoother, they may not be rough enough to trip the

flow and keep it attached on the leeward side of the vanes.

Shown below in Figure 29 is an experimentally determined flow field for the exit plane of the outer annulus while operating at a flow rate of 1500 SLPM. Notice the strong recirculation zone inside the annulus with reversed velocity approximately half that of the forward velocity.
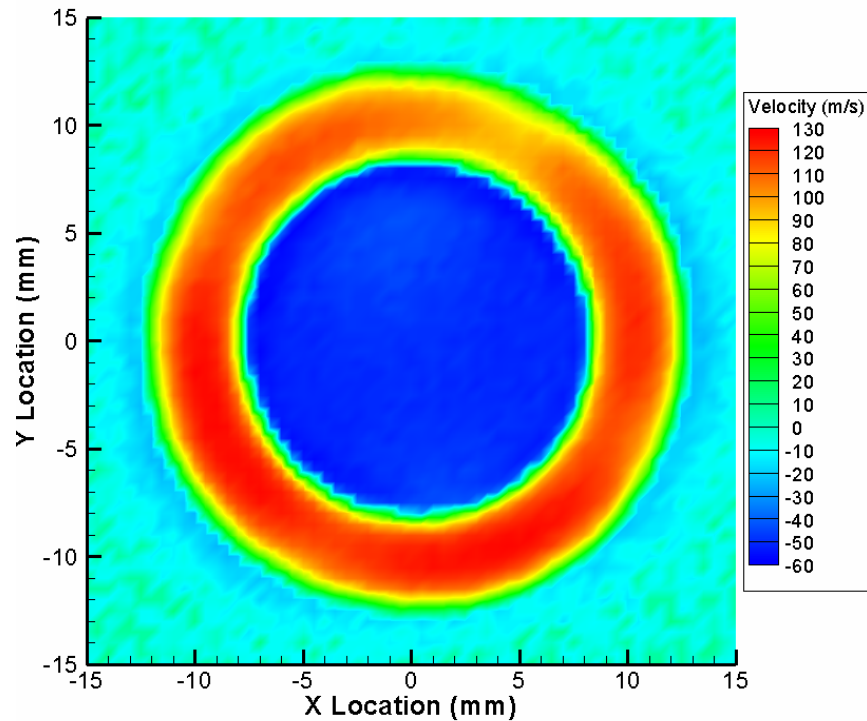
Figure 29- Experimentally determined outer annulus exit plane velocity profile at 1500 SLPM.

Once the exit plane velocity profile had been determined, the next step was to generate a complete flow field and determine the locations of the recirculation, transition and established flow zones. To determine the axial location of the recirculation zone and transition zones, the Pitot probe took data in one quarter millimeter increments along the Z axis of the nozzle. The point where the flow changed from negative to positive velocity marked the end of the recirculation zone. This point was at 10.5 millimeters down the Z-axis, which translates to approximately 0.4 L/D downstream of the exit plane. The point along the Z-axis where the axial velocity no longer increased marked the break

61

point between the transition and established flow zones. This point was at 60 millimeters down the Z-axis, which translates to approximately 2.4 diameters downstream of the exit plane. A plot of this data is shown below in Figure 30.
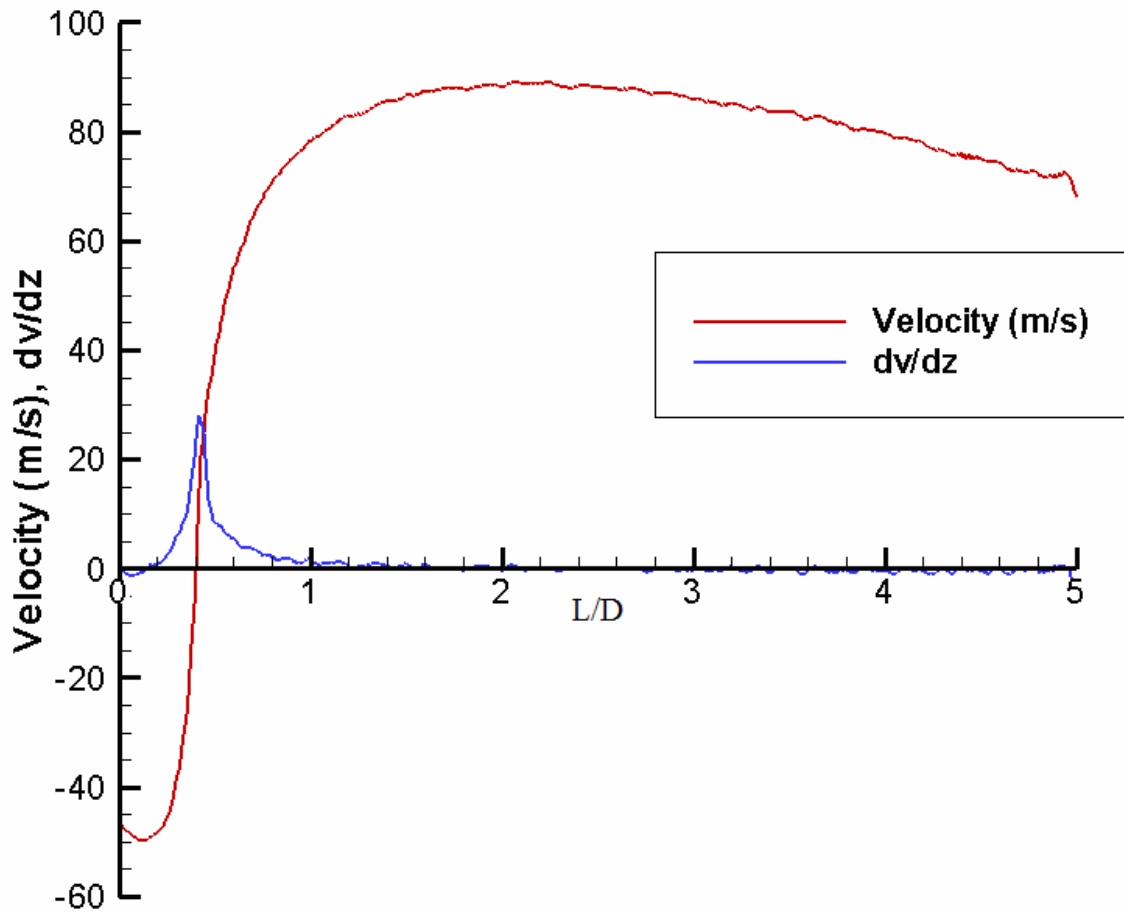
Figure 30- Plot of centerline axial velocity and derivative along centerline of outer annulus while running at 1500 SLPM

Once these locations were determined, the traverse was programmed to gather velocity profiles at the exit plane, in the recirculation zone, at the break point between the recirculation and transition zones, in the transition zone, at the break point between the

transition and established flow zones, and in the established flow zone. The resulting flow fields are shown below in Figure 31.
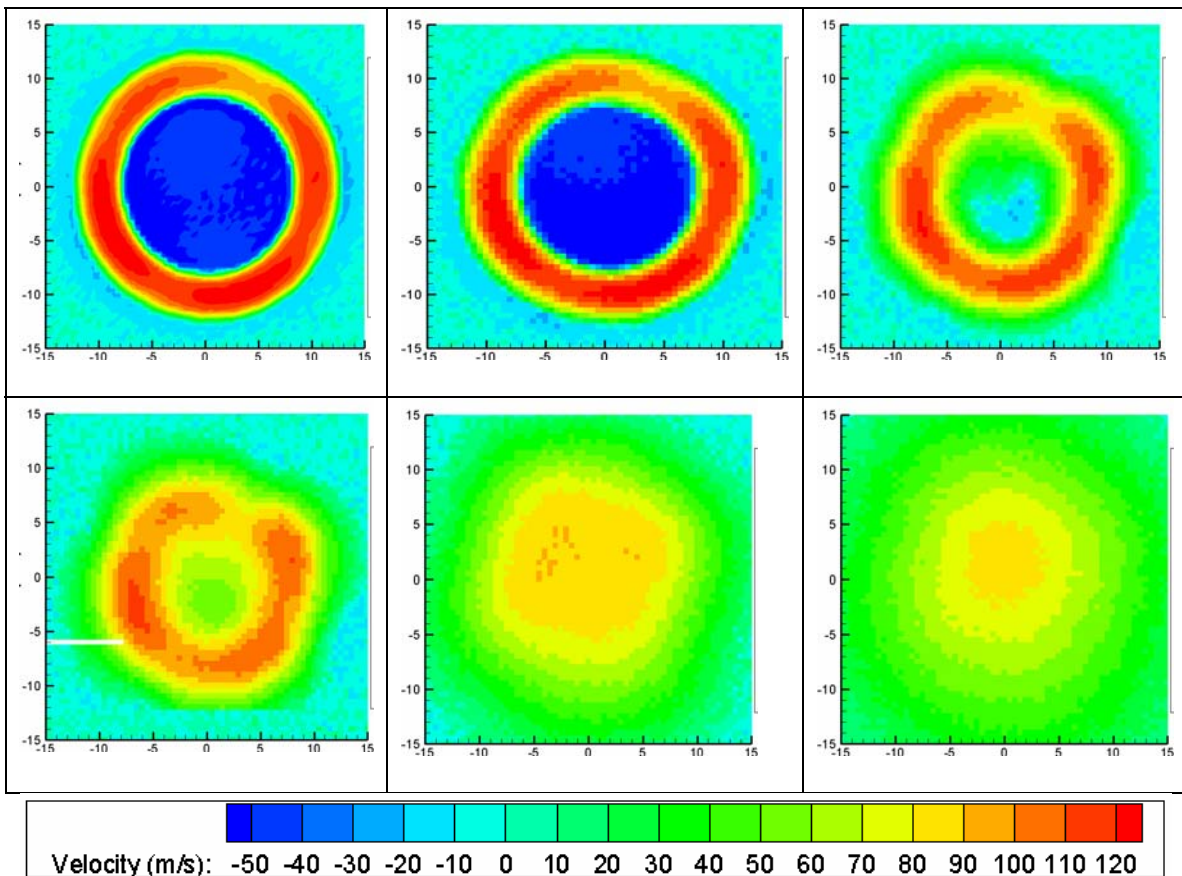
Figure 31- Outer annulus velocity profile at L/D= 0, 0.2, 0.4, 0.6, 2.4, 3. 0

Shown below in Figure 32 are the cross sectional velocity profiles at the aforementioned key axial positions for the annular flow field. Each zone clearly follows the velocity profile defining the zones. At the exit plane and in the recirculation zone, the flow field has a region of reversed flow located along the central axis of the nozzle. The end of the recirculation zone is marked by a region of stagnant flow along the central axis, which gives way to the transition zone. As the flow field develops downstream and enters the established flow zone, it clearly resembles a developed free jet and remains symmetric around the central axis.
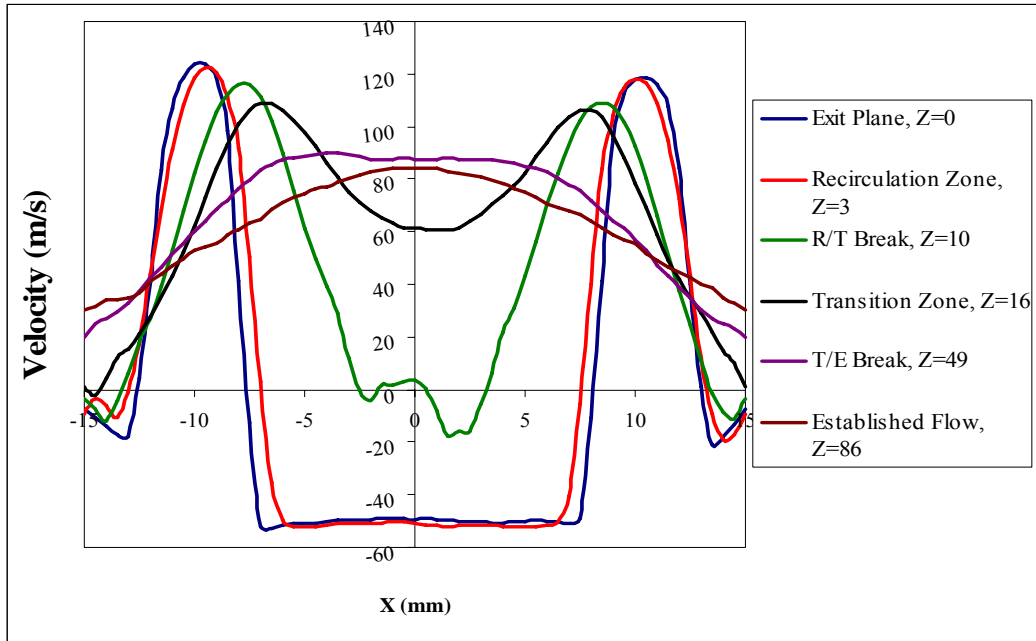
Figure 32- Centerline velocity profile of the outer annulus operating at 1500 SLPM at significant axial locations
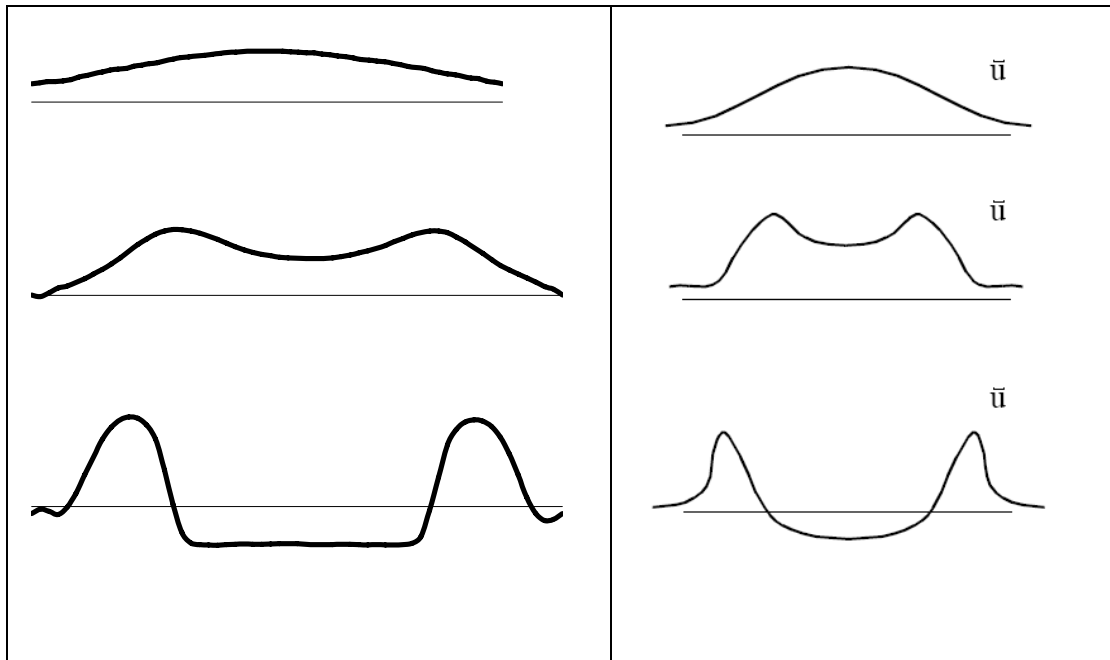
Figure 33- Qualitative comparison of experimental (left) and Davies' theoretical (right) velocity profiles of the established flow, transition and recirculation zones from top to bottom respectively.

Coflow Flow Field- External

After redesigning and experimentally testing the outer annulus, the next step was to look at the behavior of the nozzle with flows in both the outer and inner annulus, and at various mass flow rates. The goal was to generate a stable, axisymmetric flow with the largest central jet velocity possible so as to generate a large Doppler shift to facilitate flow visualizations. The central jet flow can be increased up to the maximum of the Alicat model MCR-1500SLPM-D/5M mass flow controller, 1500 SLPM. To avoid any inconsistencies in the flow velocity, the mass flow controllers have a reaction rate of one millisecond. Even with this, because the outer annulus air does not pass through a stagnation chamber, there were still some fluctuations in the mass flow rate. While running at a set point of 250 SLPM the actual output rapidly oscillates by +/- 10 SLPM around the set point. This variance only exists when the central jet air is also being run, so the independent outer annulus flow tests were not affected. Although the flow oscillations are important for the Pitot probe measurements, most of the actual Rayleigh scattering flow visualizations are time averaged, so any small fluctuations in the flow velocity are also averaged.

When the mass flow rate of the central jet flow was set to 1250 SLPM, the maximum velocity for the central jet flow increased to ~190 m/s or Mach number 0.56. Although there is still a flow bias towards one side of the outer annulus, the magnitude of the velocity of this flow field may render the bias inconsequential. The flow at the outlet of the nozzle can be seen below in Figure 34. In this and all following figures showing Pitot probe resolved data, the grid area is set at 0.25 mm^2. The number of data points was quadrupled relative to initial tests to further refine the resolution of the flow field.
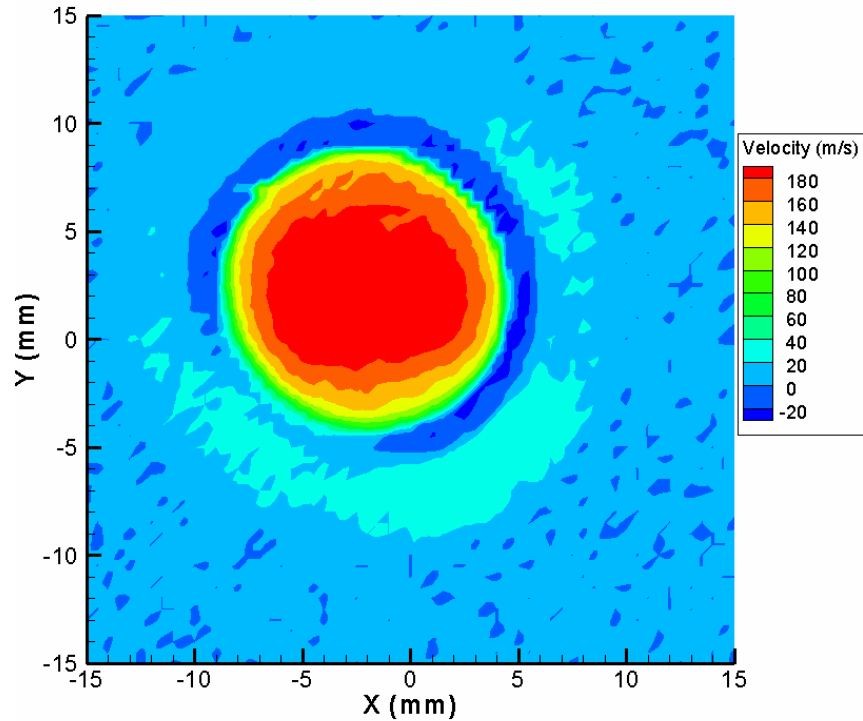
Figure 34- Original coflow nozzle exit plane velocity contour at central jet and outer annulus mass flow rates of 1250 and 250 SLPM respectively.

Figure 35 below shows the evolution of the velocity field as it moves from the nozzle exit plane to five diameters away. At this distance the core flow maintains an average of seventy five percent of its velocity when compared to the exit plane of the nozzle, although it has diverged significantly. It is important to note that the influence of the outer annulus flow dramatically reduces as the flow moves away from the nozzle. The outer annulus flow is not even visible on the contour plot as close as one diameter away from the nozzle. Because of this, a separate test was conducted to investigate the development of the outer annulus flow field independent of the central jet flow. This test shows that although there is a strong asymmetry in the flow velocities initially, as the flow propagates downstream of the exit plane, this asymmetry dissolves and the flow begins to change from an annular cross section to a circular cross section. For this

reason, the outer annulus air can only be considered a truly separate flow field from the central jet flow in the region near the exit plane of the nozzle. After only one diameter down stream, the outer annulus flow is indiscernible from the central jet flow.
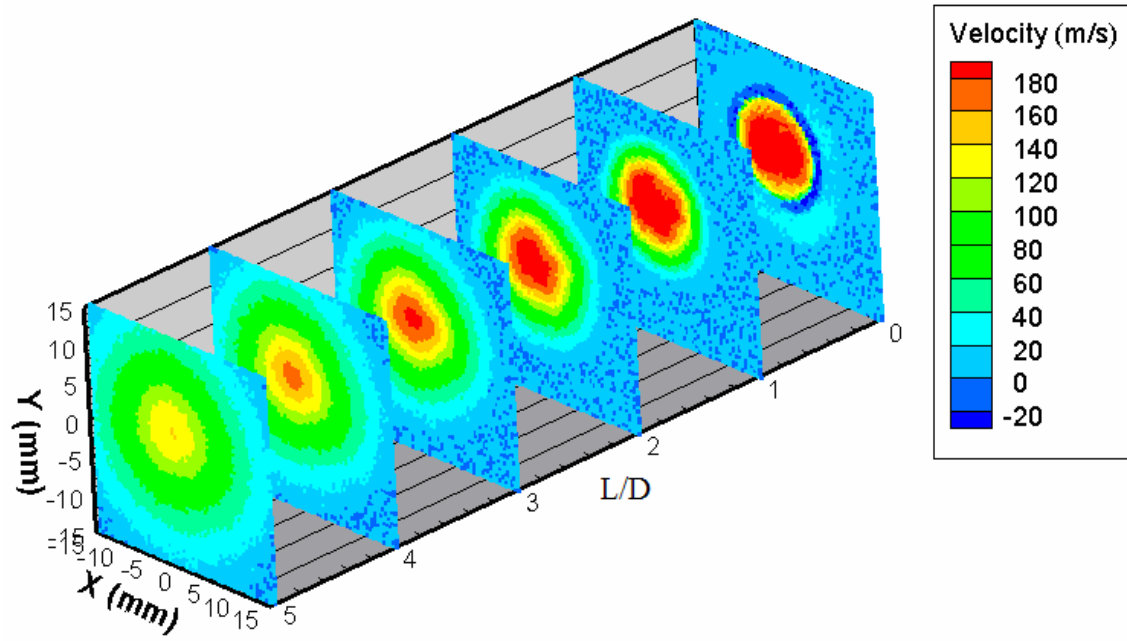
Figure 35- Original nozzle Coflow velocity field at central jet and outer annulus mass flow rates of 1250 and 250 SLPM respectively.

Shown below in figures Figure 36 and 37 are the experimentally determined coflow fields of the redesigned
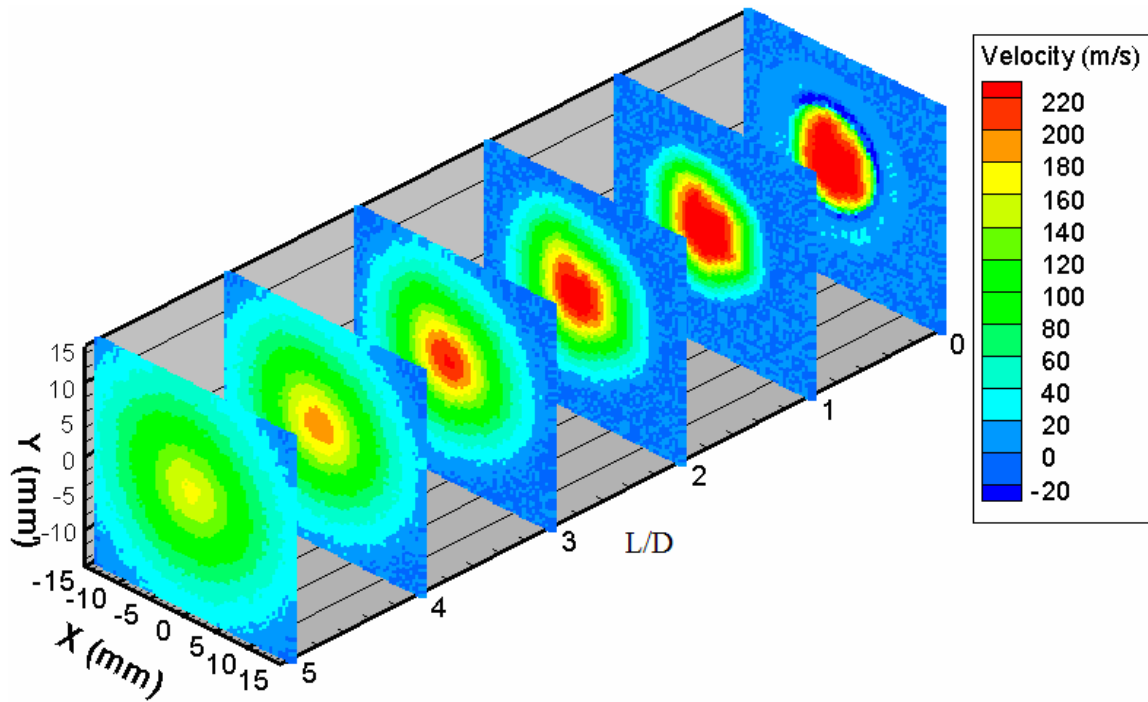
nozzle.

Figure 37
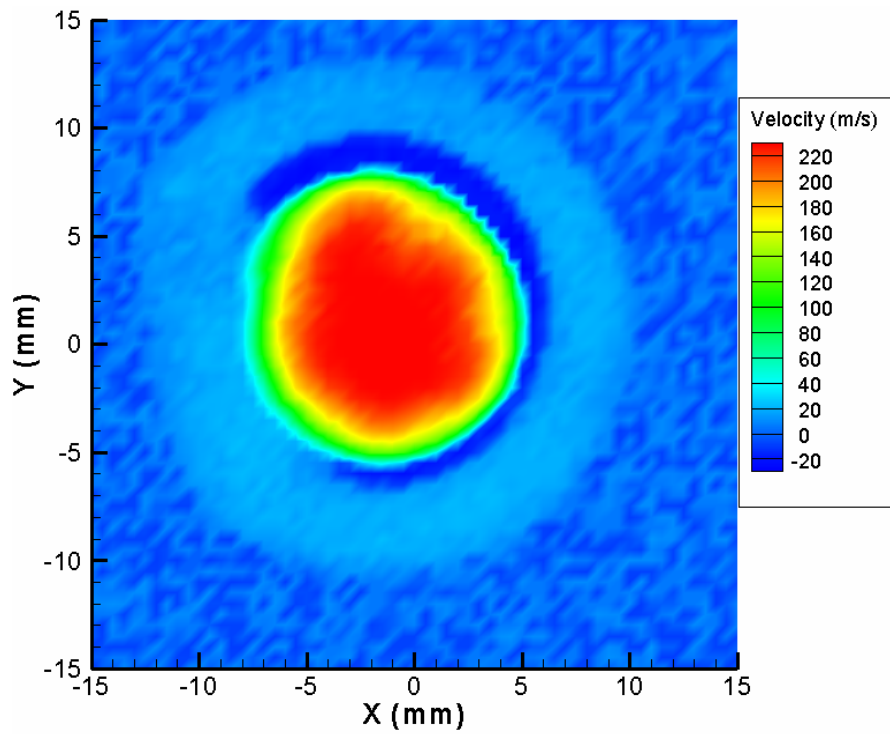
Figure 36- Exit plane velocity contour of redesigned coflow nozzle at central jet and outer annulus

mass flow rtes of 1500 and 250 SLPM respectively.

Figure 37- Redesigned nozzle coflow velocity field at central jet and outer annulus mass flow rates of 1500 and 250 SLPM respectively.

Comparison with the original nozzle reveals very similar coflow velocity profiles, both in magnitude and overall composition.

Doppler Shift

The Doppler shift generated in this experiment is a function of the velocity of the flow field. As the velocity increases, the change in frequency will also, as shown in equation 4.9 (Young, Freedman).

$$f' = \left(\cfrac{f_o}{\cfrac{1}{\sqrt{1-\left(\dfrac{V}{C}\right)^2}}\left(1+\dfrac{V\cos\theta}{C}\right)} \right) \qquad (4.9)$$

With a maximum flow velocity of ~232 m/s and an camera angle of 23.5 degrees, the corresponding expected Doppler shift was ~0.41 Ghz.

Iodine Filter Absorption Characteristics Investigation

To facilitate the filtered Rayleigh scattering flow visualizations, it was necessary to determine the absorption characteristics of the molecular iodine filter. More specifically, it was necessary to determine at what laser settings the iodine filters would provide the least transmission. It was empirically determined that there were three distinct and repeatable etalon temperature spans that corresponded to a sharp transition in iodine absorption. In each case the temperature spans were both repeatable and consistent in absorption characteristics. Shown below in Table 3 are the three etalon temperature spans of interest.

Table 3- Laser intercavity etalon temperature spans corresponding to iodine absorption notches.

Leading Edge	Peak Absorption	Trailing Edge
53.355	53.385	53.505
54.225	54.285	54.465
55.995	56.085	56.235

Although the laser output frequency is also dependent on the laser cavity length as controlled by the z-axis DAC program, its setting is not recorded here because it is constantly adjusted to reduced frequency deviation. The mode tune program was used to empirically determine the temperature spans corresponding to strong iodine absorption as

described in the methodology section of this paper. However, it was observed that merely aborting the mode tune program once it was centered inside an absorption well did not produce favorable results due to a possible lag between the temperature displayed on the laser controller versus the actual etalon temperature. Aborting mode tune in the middle of a well would typically allow the laser to continue heating and stabilize at a frequency beyond the observed notch. To combat this behavior, the mode tune program was typically halted 0.2 degrees prior to the leading edge of the notch and allowed to stabilize at a frequency within the well.

Once aborting mode tune and allowing the laser frequency to stabilize, the v-track program was engaged and the power and light regulation modes were selected. These programs maintain constant power output and laser frequency even over extended periods. It is also important to note that the laser head produces significantly more power output at different frequencies/etelon temperatures than others. Shown below in Table 4 is a tabulation of the maximum single frequency single mode laser power output at the three temperature spans of interest.

Table 4- Maximum laser power relative to iodine absorption notches

Temperature Span (C)	Peak Laser Power- Watts
53.355-53.505	~5.2
54.225-54.465	~9.2
59.995-56.235	~8.5

Flow Visualizations

Initial Setup and Refinement

Once the optimal iodine filter absorption temperatures were determined the next step was to begin capturing images. The low pressure iodine filter was set to 80 C and

the laser power was set at 1.2 watts through adjustment of the laser aperture. To place the incident light frequency just inside the low frequency edge of an absorption notch the laser was run through the mode tune program, aborted at 53.145 C and light and power regulation modes were engaged. When the program was aborted the iodine had not visibly began to reduce the background scattering seen through the digital camera. However, over the next 30 to 60 seconds, the laser frequency increased sufficiently to move into the sharp cutoff iodine absorption well. This was evidenced by a significant reduction in light intensity received by the camera. At this point, initial no flow images were captured as shown below in Figure 38.
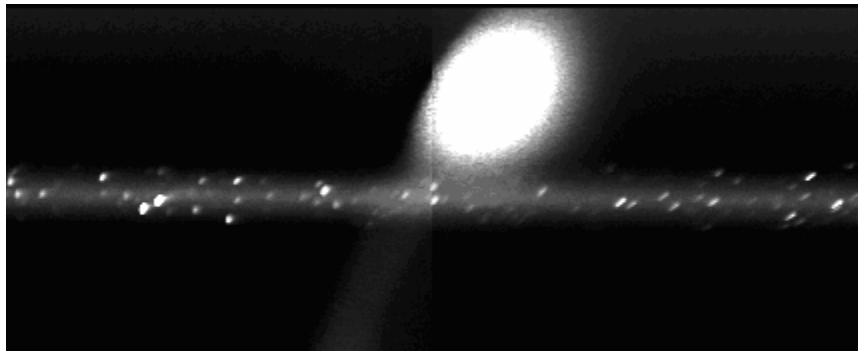
Figure 38- Initial camera images of laser line with no flow using the less dense iodine filter-Dual Dac

Although this first image had a significant reflection, the Rayleigh and Mie scattering signals are still clearly visible. The rather lengthy process of refining the experimental setup as well as additional images not shown in the body of this paper can be found in appendix C.

Because this system may be used for gathering time resolved data in the future, one parameter of interest is the camera frame rate. Although the camera is capable of exposure times as low as 5μs, to gather relevant data the camera must be exposed for substantially longer. The frame rate is a function of three parameters; camera sensitivity,

signal level and noise level. Although camera sensitivity is typically held constant for an experimental setup, the received light intensity can be increased by either increasing the incident light intensity or increasing the Rayleigh scattering signal. Increasing the incident light intensity is as simple as increasing the power to the laser. Shown below in Figure 39 and Figure 40 is a comparison of filtered images of the laser line with no flow field taken at 100 Hz with the laser power at 1.2 watts and 5.9 watts respectively. In this and all future pictures, the intensity plot is for the received intensity at the nozzle centerline and the D refers to the nozzle outer annulus diameter. Also, these images were taken at a distance of two diameters downstream and filtered using the more dense iodine filter set at 110 C.
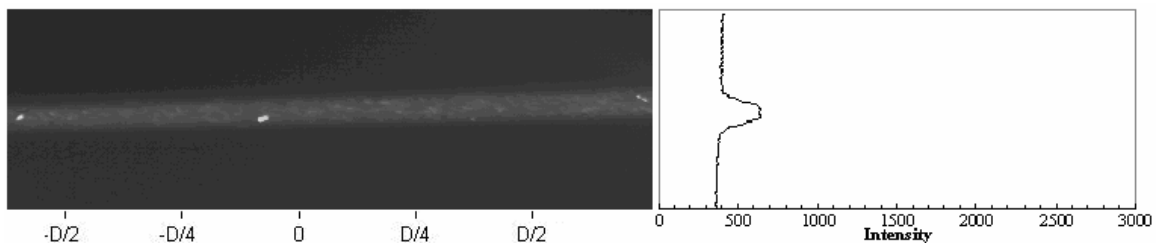
Figure 39- No flow image of 1.2 watt laser line at 100 Hz frame rate
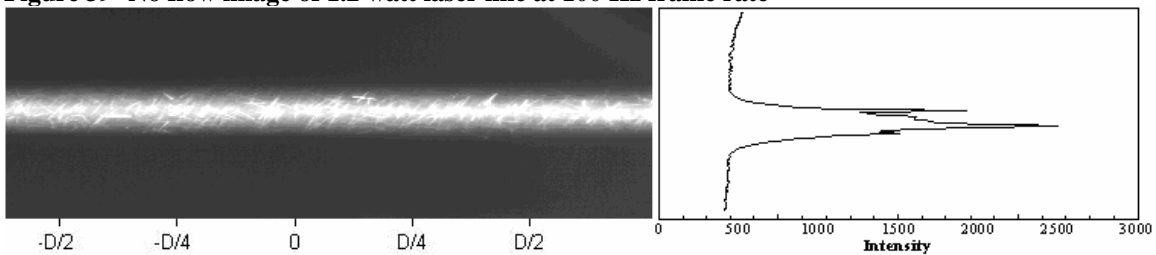
Figure 40- No flow image of 5.9 watt laser line at 100 Hz frame rate

The increase in laser power led to much more intense signals and a slight increase in background noise intensity. This signal to noise ratio increase will reduce the required camera exposure time and facilitate future time resolved data collection. The benefits of increased signal strength were clearly evident, but highlighted the predominance of particles in the stationary laboratory air. To smooth the data, the images were still collected at 100 Hz but they were averaged over at least 300 images. Because the data

would be used in its averaged form, averaged images from the baseline 250 SLPM outer

annulus flow field at both high and low power were compared.
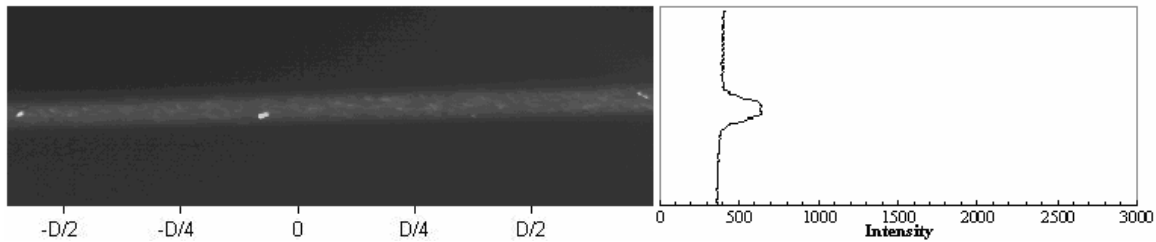
Figure 41- Averaged image of 250 SLPM outer annulus flow field at 1.2 watts laser power
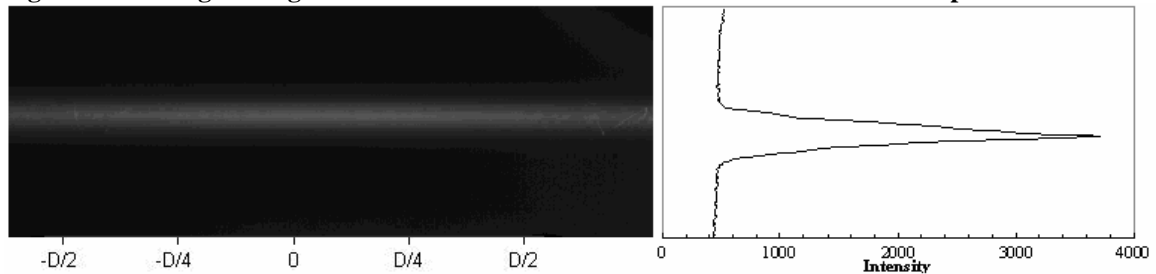
Figure 42- Averaged image of 250 SLPM outer annulus flow field at 5.9 watts laser power

Just as in the previous instantaneous case, the higher power laser setting produced a

significantly higher signal to noise ratio by increasing the signal without appreciably

increasing the background levels. The nearly 5 fold increase from ~1.2 to ~5.9 watts

returned a similar increase in signal level of nearly 5 fold. Although the laser only output

~5.9 watts at this etalon temperature, up to 9.5 watts were capable at other etalon

temperatures. Because of this, it would be beneficial for future research to be conducted

at an iodine absorption notch that allows for a higher laser power output.

To illustrate the effectiveness of the iodine filter, filtered and unfiltered images

were taken under several different flow conditions and compared. As seen below in a no

flow comparison of filtered and unfiltered images, the filter drastically reduces the

incident light intensity as well as the more intense particle scattering.
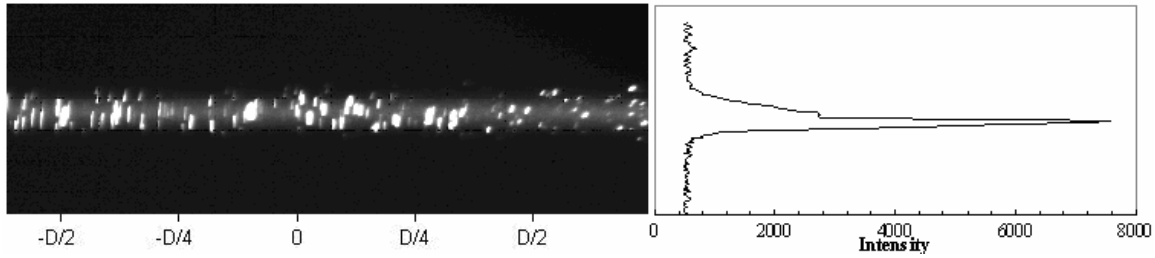
Figure 43- Instantaneous unfiltered view of laser line with no flow field at 100 Hz
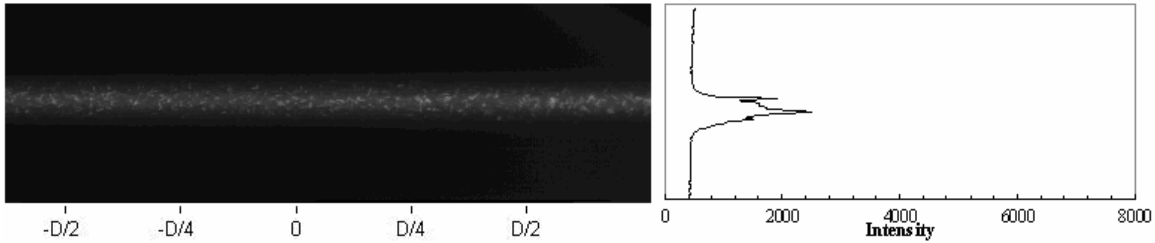
Figure 44- Instantaneous filtered view of laser line with no flow field at 100 Hz

Shown below are filtered and unfiltered images of a 250 SLPM outer annulus flow field. The light intensity in the no flow regions to the far edges of the unfiltered image is significantly less than the unfiltered case. The flow fields however have nearly the same light intensities due to the flow being Doppler shifted out of the iodine absorption well. This behavior is further investigated later.
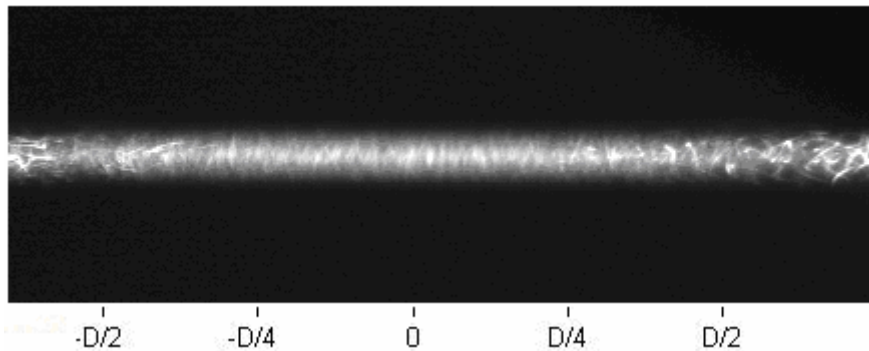
Figure 45- Instantaneous unfiltered image of 250 SLPM outer annulus flow field at 100 Hz
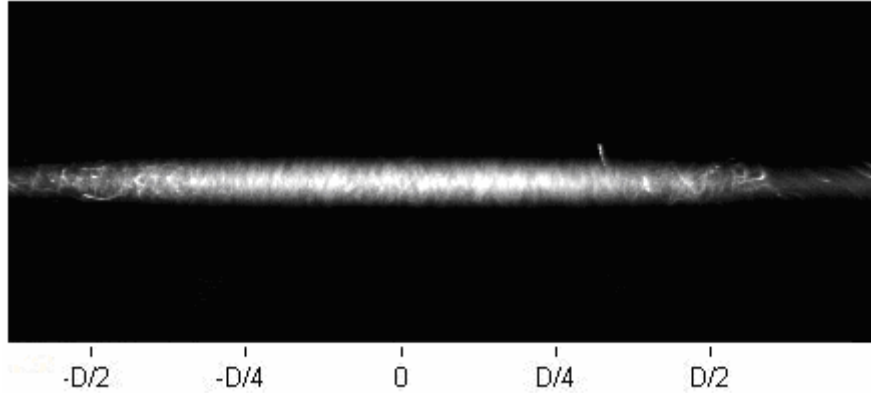
Figure 46- Instantaneous filtered image of 250 SLPM outer annulus flow field at 100 Hz

Flow Field Visualizations

To develop relationships between flow velocity and the resulting Rayleigh scattering signal it was necessary to gather data at multiple flow rates. For most of the testing done, a 250 SLPM outer annulus flow with no central jet flow is the baseline flow from which other flows are compared. All flow conditions, unless noted otherwise, refer to the specified central jet flow rate and an outer annulus flow of 250 SLPM. Tests were conducted at central jet flow rates from zero to 1500 SLPM while operating within an iodine absorption notch at 53.145 C and gathering data at 100 Hz. The image data was averaged over several hundred frames to reduce the influence of particles on the resulting data plots. The y-axis of the plots is the light intensity of the received signal. Although it is unitless, the scale is consistent for all pictures in this experiment. Shown below in Figure 47 is a plot of the received filtered Rayleigh scattering signal intensities at the laser centerline for several different flow rates.
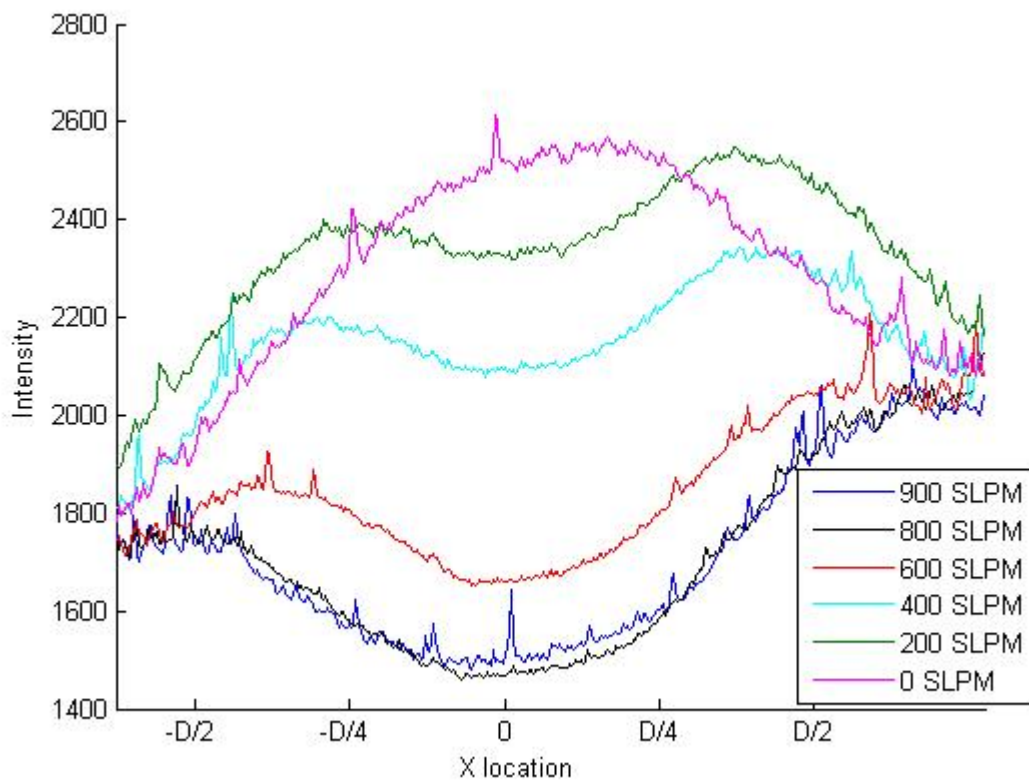
Figure 47- Centerline received FRS intensity profile at varying mass flow rates with no post processing.
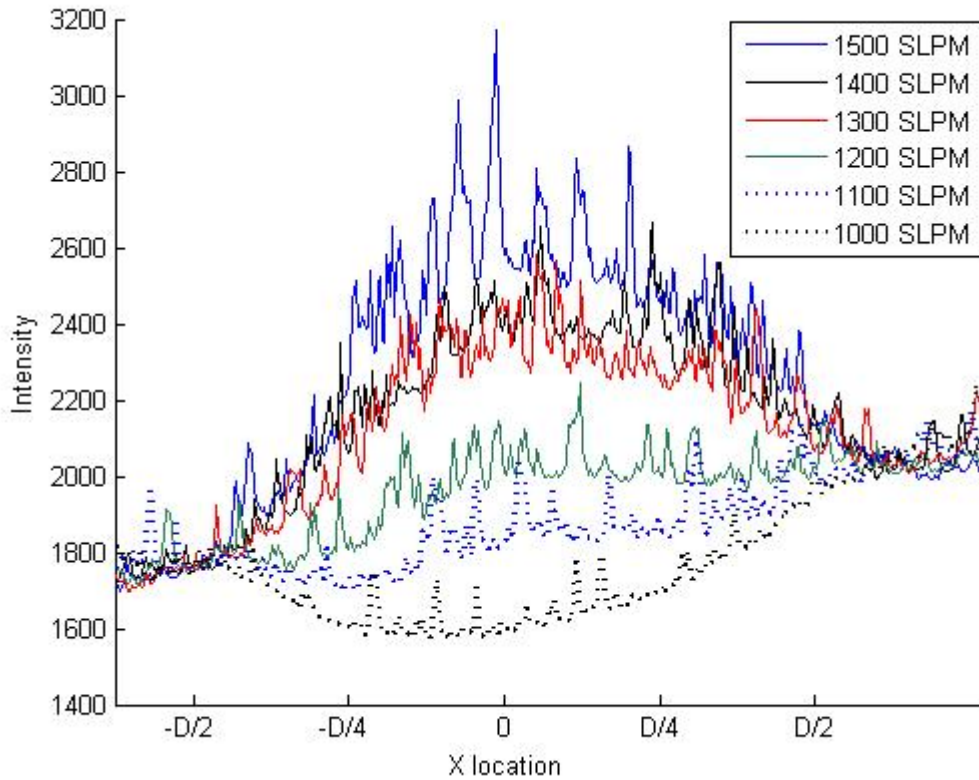
Figure 48- Centerline received FRS intensity profile at varying mass flow rates with no post processing.

The baseline of this plot is 250 SLPM outer annulus flow (labeled 0 SLPM in figure 47) with a somewhat Gaussian shape. When the center jet flow rate was increased, the resulting FRS signal was significantly reduced through the region of flow. This relationship held for flow rates up to ~900 SLPM at which point this relationship reversed and any increase in flow resulted in an increase in received intensity. In addition to this, at the high flow rates the data lines became more irregular, although the overall trend was still obvious. The spikes in the high flow rate data could be due to particles in the flow being shifted outside the absorption notch, or from the faster flow entraining more particles. Although either of these conjectures seem possible, further investigation was necessary before drawing conclusions.

Although simply looking at the centerline data from the different flow rates yields a good idea of the bulk flow properties, relating data from the varying flow rates to the baseline yields a different and relative way of viewing the data. Because the FRS signal outside the region of flow is relatively consistent between the different flow rates, subtracting data from two images accentuates the differences in FRS signals inside the region of flow. Considering the 250 SLPM outer annulus flow data as the baseline, data from higher flow rates were subtracted from it. This resulted in a plot (Figure 49) showing a clear relationship between FRS signal and flow rate.
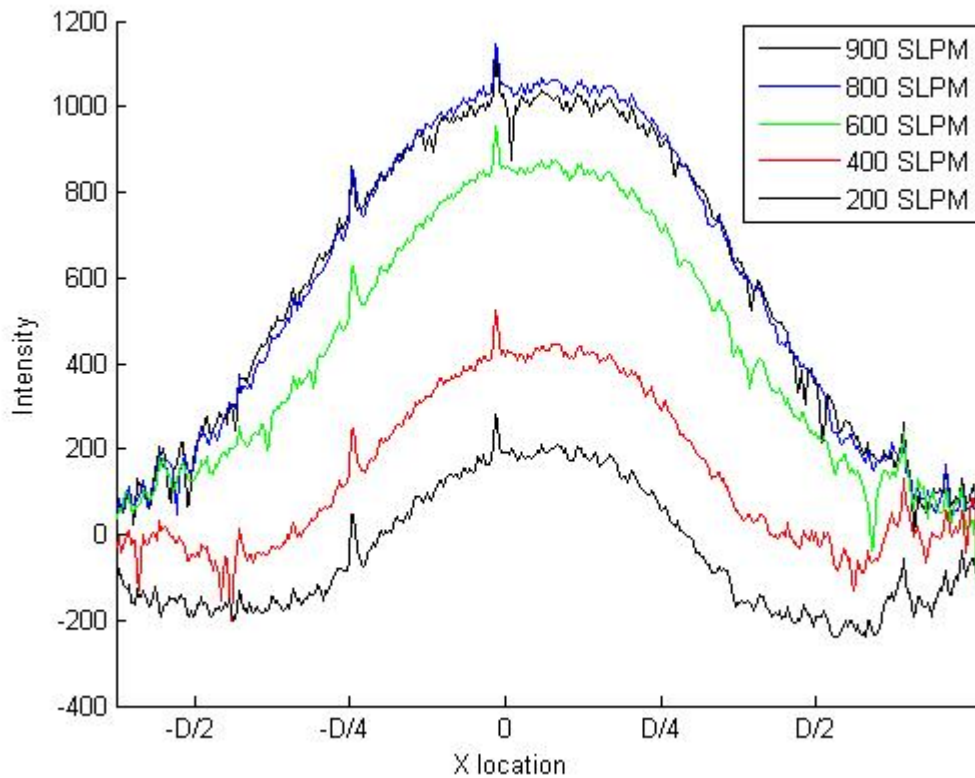
Figure 49- Received FRS centerline intensity for lower central jet mass flow rates relative to the 250 SLPM outer annulus baseline flow.

Clearly, as the flow rate increased, the FRS signal in the region of flow was reduced. This relationship however, was only consistent for lower flow velocities and

seemed to plateau between 800 and 900 SLPM. As the flow increased it also diverged

and resulted in a broader region of relative signal reduction. The peaks on each of the

data lines at ~-D/4 and ~0 X locations are due to particles in the baseline flow causing

signal spikes at those locations. It is important to realize that the data shown above is

only the relative FRS signal between the different central jet flow rates and the baseline.
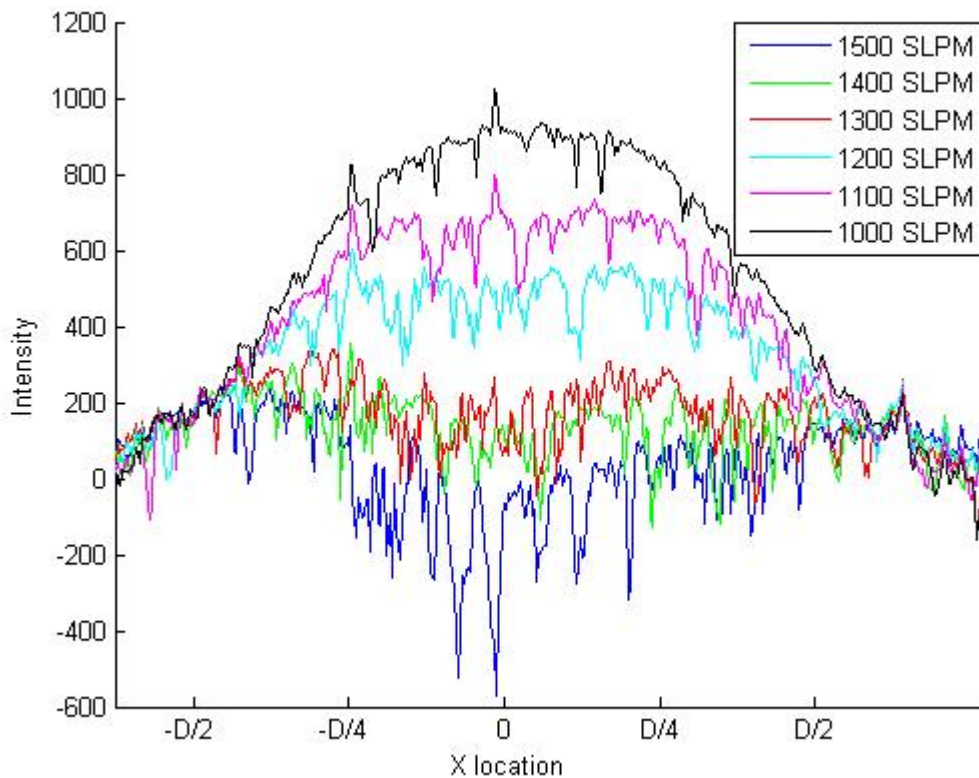
Figure 50- Received FRS centerline intensity for higher central jet mass flow rates relative to the 250 SLPM outer annulus baseline flow.

Although the lower flow rates show a decrease in FRS signal with an increase in

flow velocity, the higher flow rates show the opposite. Beyond an inflection point of

~900 SLPM, any increase in flow velocity lead to an increase in received FRS signal. It

also leads to an increase in data fluctuations caused by particles in the flow. At the

maximum flow rate of 1500 SLPM, the flow actually had some particle scattering

induced points with more signal than the baseline runs.

This relationship between the FRS signal of the baseline conditions and different

flow rates can also be shown through image subtraction as well. Shown below are the

images of several central jet mass flow rates subtracted from the baseline image. The

resulting images show bright regions where the FRS signal is less intense than the

baseline signal. The intensity of brightness corresponds to the magnitude of difference

between signals.
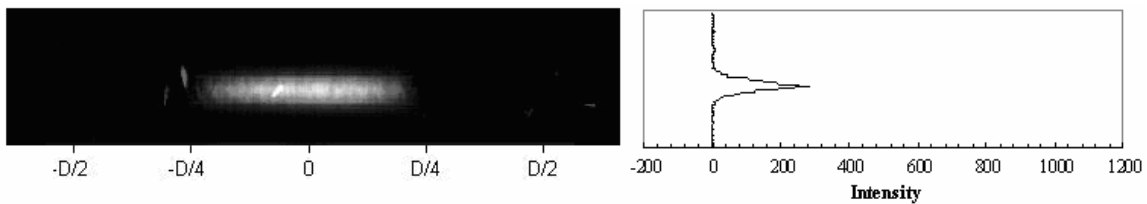
Figure 51- Relative intensity image from subtraction of 200 SLPM central jet flow from the baseline image.
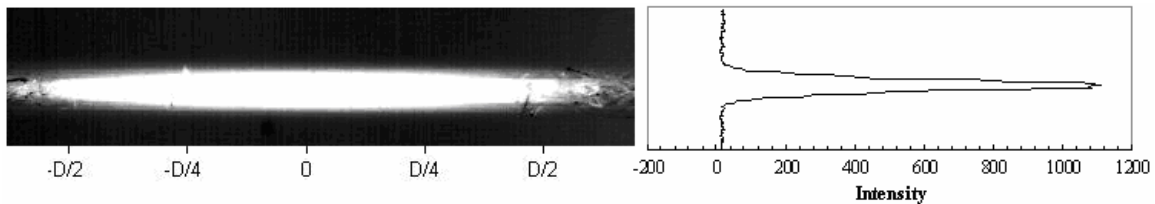
Figure 52- Relative intensity image from subtraction of 900 SLPM central jet flow from the baseline image.

Clearly as the flow rate increased from 200 to 900 SLPM, the FRS signal received

was reduced, although this relationship was reversed for flow rates higher than 900

SLPM. The images at the higher flow rates were also less distinct because the received

signals fluctuated more. Shown below is the image for 1300 SLPM, the image shows

less intensity in the flow region compared to the 900 SLPM case because at this flow rate the received signal intensity has increased towards the level of the baseline image.

-D/2   -D/4   0   D/4   D/2
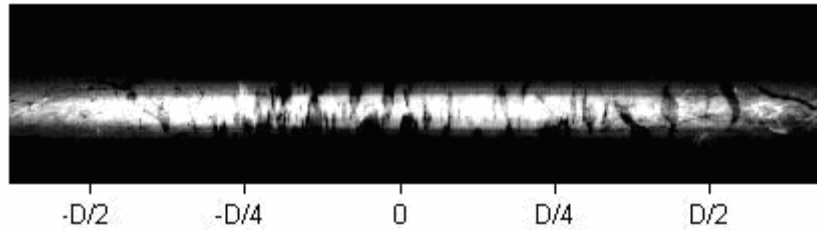
Figure 53- Relative intensity image from subtraction of 1300 SLPM central jet flow from the baseline image.

It is also clear that particles in the flow have a significant influence at this flow rate as evidenced by the dark spots indicated signal spikes caused by particle scattering.

Relative intensity images of several more flow rates can be found in Appendix D.

Data Normalization

While conducting experiments it became obvious that even unfiltered images would have reduced intensity in the flow region because of reduced particulate density. This raised the question of how much of the change in FRS signal at different flow rates was due to particle reduction and how much was due to Doppler shifting the incident light. To examine this, a reference set of unfiltered images was taken at all flow rates. This allowed for the filtered images to be normalized by the unfiltered, thus eliminating the observed changes in signal intensity due to reduced particles in the flow field.

To normalize the filtered images, unfiltered images were taken at the same flow conditions. There were two ways to produce an unfiltered image for normalization purposes, but each had their advantages and disadvantages. One option was to simply remove the existing filter. Although this was a simple option, the extremely close proximity of the camera and filter made it difficult to remove the filter entirely without

disturbing the camera. Given the difficulty in both focusing and aiming the camera on the region of interest and the near impossibility of recreating the exact camera view, angle, and distance from the laser beam if moved, it was decided to simulate the unfiltered image. To simulate an unfiltered image, the laser etalon temperature was intentionally set at 51.975 C, a point well outside the iodine absorption regions. While at this temperature, each flow condition was recreated and the data was taken again. This unfiltered data also had some interesting trends.

With only the outer annulus running at a mass flow rate of 250 SLPM, changes in the central jet had an effect on the received light intensity. As the central jet increased in intensity, the received light intensity decreased, but not as it would through filtered Rayleigh scattering. In this case, the data was being averaged at 64 pictures per frame and at up to 10 frames were averaged together. Because of this, the reduction in received light intensity can be attributed to the reduction of particles in the region of interest caused by the cleaner air of the experiment. This causes a noticeable reduction in received signal in the region of flow. Outside the region of flow, the received signal is nearly invariant with flow velocity, as expected. Because the reduction in received signal in the flow region is only due to the relatively clean air causing less particle scattering, it seems reasonable that this relationship would show diminishing returns at higher flow rates. This point is well illustrated in a plot of the received centerline signal intensity at varying central jet flow rates shown below.
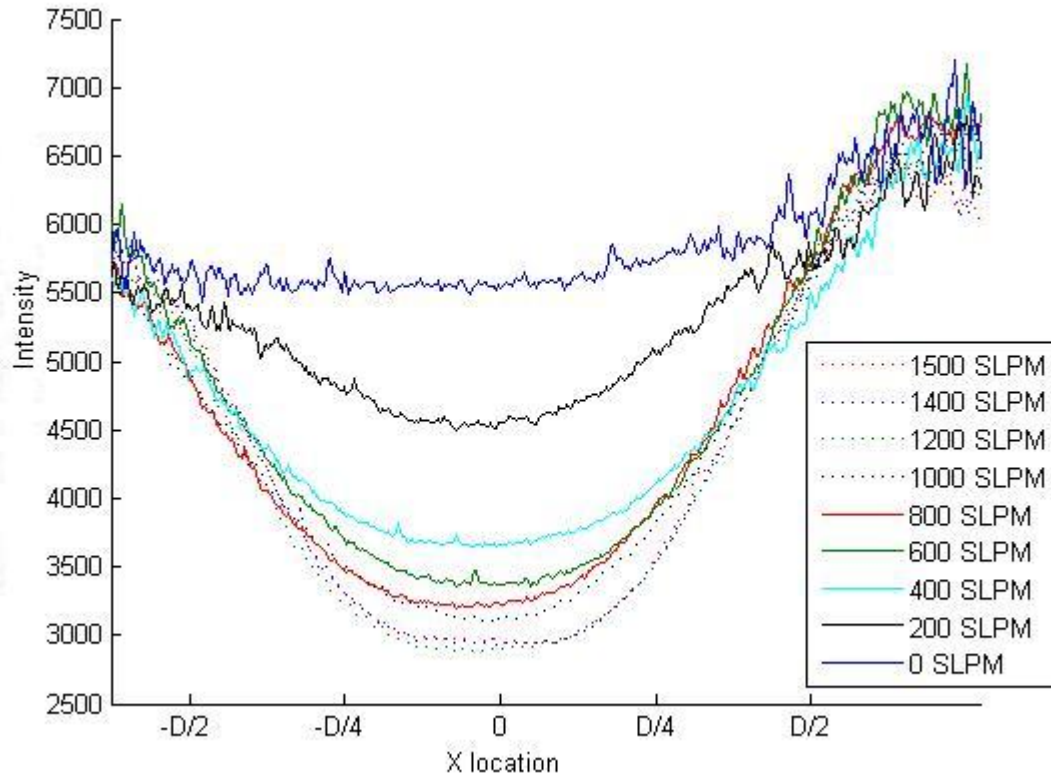
Figure 54- Plot of received unfiltered Rayleigh scattering signal at varying central jet mass flow rates.

Beyond 1000 SLPM, any increase in flow rate had very little effect on the intensity of the received light in the region of flow. This does not suggest that at high flow rates there are no particles, only that there are fewer particles at the higher flow rates because the experiment air has a reduced particle density compared to the laboratory air.

Shown below in Figure 55 and Figure 56 are normalized plots of the centerline intensity for multiple central jet mass flow rates all. Again, the outer annulus flow rate was held constant at 250 SLPM.
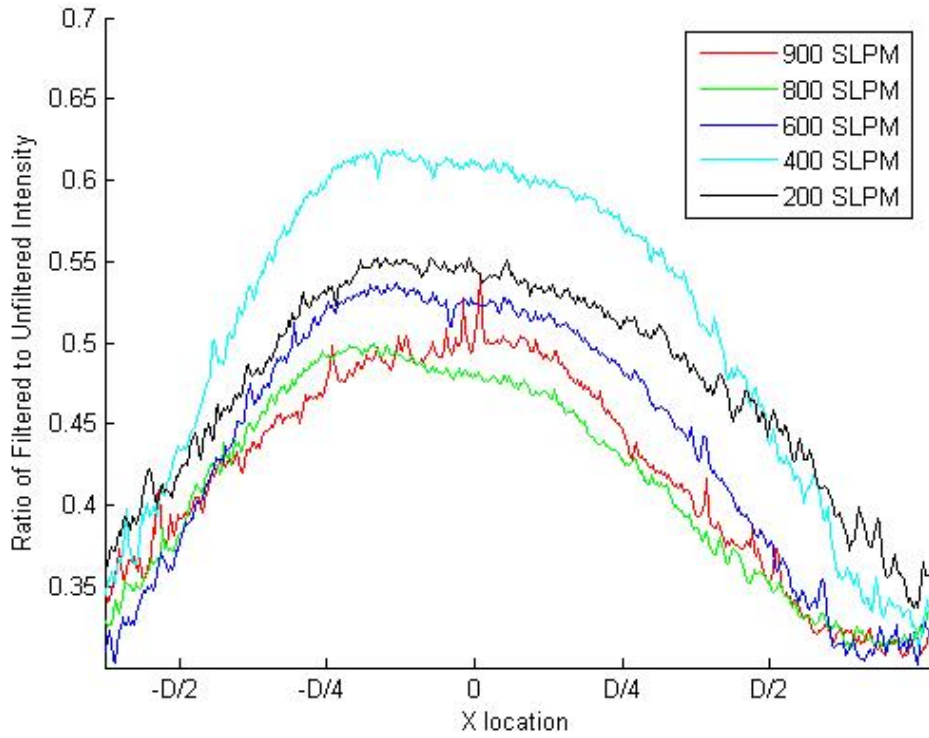
Figure 55- Plot of FRS intensity normalized by unfiltered Rayleigh scattering signal at varying flow rates.
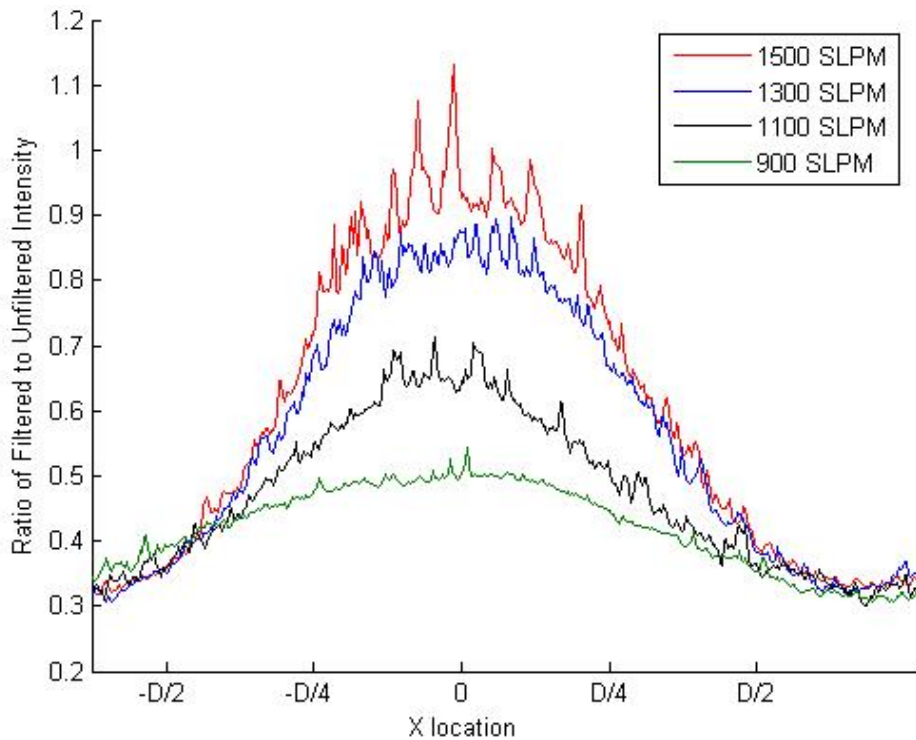
Figure 56- Plot of FRS intensity normalized by unfiltered Rayleigh scattering signal at varying flow rates.

When examining the normalized data the ratio of filtered to unfiltered intensities away from the region of flow yields an approximation of the absorption percentage of the iodine cell at that laser frequency. With the cell operating at 110 C and the laser etalon temperature at 53.145 C, the iodine absorbs approximately 60 to 65 percent of the incident light. This does not indicate a strong absorption notch given that other researchers have experimentally determined nearly 100% absorption notches, but there are many factors that can influence this, including cell depth, iodine density/pressure and cell temperature.

There seem to be two distinct trends for the normalized plots, one for the low flow rates and one for the high. Plots of the lower flow rates, from 200 to 900 SLPM, have similar smooth shapes and as flow rate increases, the normalized intensity decreases. The plots for the higher flow rates increase both in magnitude and fluctuation as the flow rates increase. This is the same trend as seen before in the non-normalized data, but is more prominent here.

Outer Annulus Flow

When conducting experiments the images for the 250 SLPM outer annulus flow field at 1 diameter distance yielded curious results. With the laser frequency tuned just inside the low frequency edge of the absorption notch, the positive flow exiting the nozzle caused an increase in the brightness of the received image. In a particle-free environment, this would intimate that the flow has a negative velocity at this location, although that was contrary to previously gathered experimental data for the outer annulus flow field at higher flow rates. Shown below are the images for the no flow and the 250 SLPM outer annulus flow.
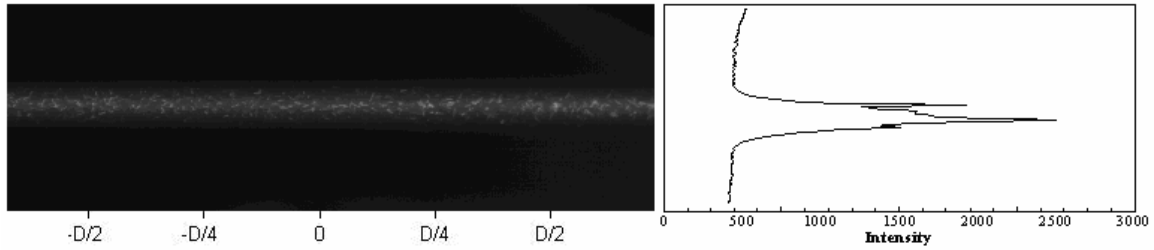
Figure 57- No flow image of laser line at 100 Hz frame rate
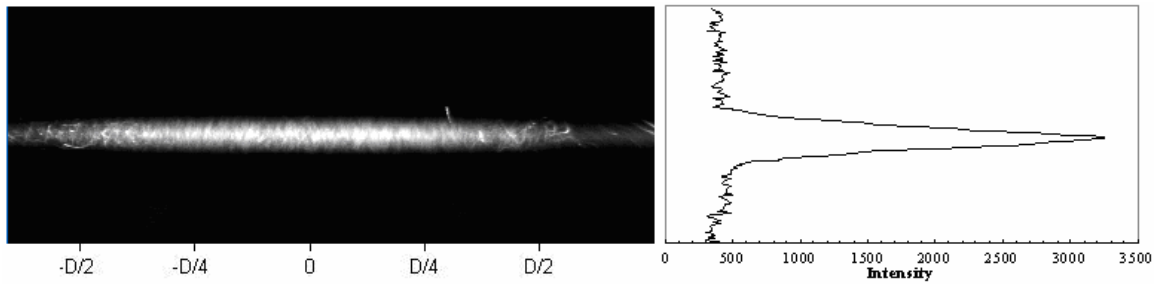
Figure 58- 250 SLPM outer annulus flow field image at 100 Hz frame rate

Clearly the addition of the flow field in the second image increases the image intensity in the region of interest.

Data Rate

Conceivably this same setup may be used in the future to gather time resolved data of flow fields, which makes the image frame rate a key parameter. Because of this, the maximum frame rate at which the Rayleigh scattered signal could be distinguished from the background signal was experimentally determined. Shown below in Figure 59 and Figure 60 are images of no flow and 1500 SLPM outer annulus flow field, both taken at a frame rate of 1 kHz.
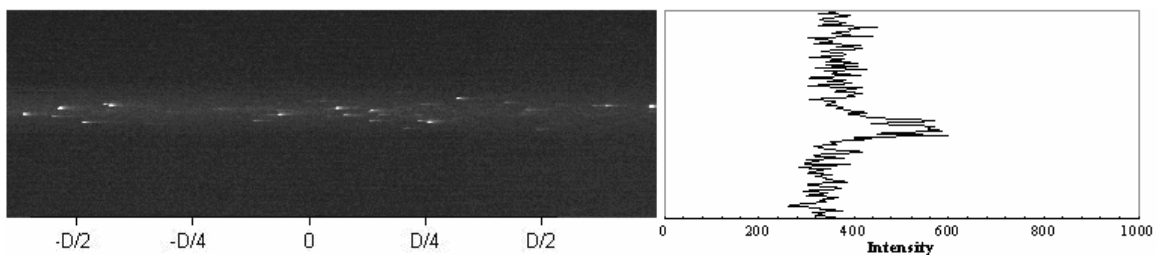
Figure 59-Filtered image of laser line with no flow field at 1kHz frame rate
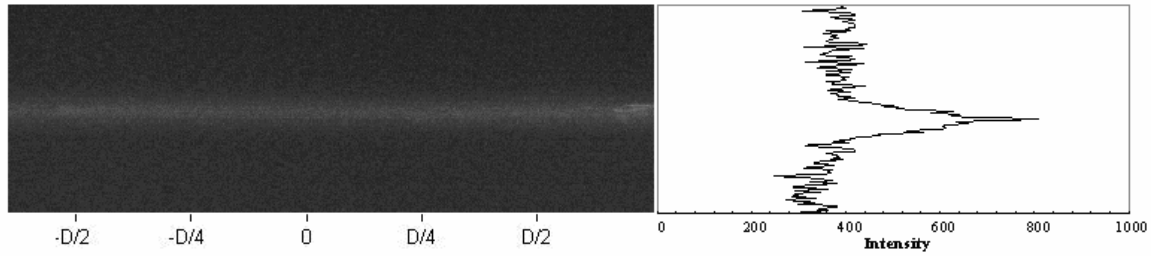
Figure 60- Filtered image of 1500 SLPM outer annulus flow field at 1kHz frame rate

In both cases the Rayleigh scattered signal is clearly distinguishable from the

background noise, although with such a low signal to noise ratio, significant data could

be difficult to extract from such images.

V. Analysis

Coflow Nozzle Characteristics

After extensive testing and redesigning, the coflow nozzle used in this experiment has been well characterized. The central jet flow field behaves as a typical atmospheric exhausting circular jet. As the flow rates increase, the measured flow velocities increase proportionally, leading to a maximum velocity of ~232 m/s at 1500 SLPM flow rate. Downstream of the nozzle exit plane the flow diverges and slows although, there still exists a coherent core flow that retains most of the initial flow velocity. At 1 L/D, where most testing took place, the flow had a maximum flow velocity of ~232 m/s corresponding to Doppler shift of ~0.45ghz.

The inner annulus initially had a bias to the side opposite the air inlet pipe causing a nearly 2:1 flow velocity ratio at the exit plane. Because the cause of this flow bias was initially unclear, a computational fluid dynamics model was generated and adjusted to recreate the flow properties of the flow at the exit plane. It was determined that insufficient air inlet pipe and stagnation volume set up an internal flow circulation that caused the flow bias at the exit plane of the nozzle. To remedy this situation a new CFD model was generated that had an air inlet pipe cross sectional area and stagnation volume nine times and five times larger, respectively, than the original nozzle. CFD testing of the new model in Fluent showed more homogeneous flow at the exit plane than the original, so it was built using a three dimensional printer and tested. Testing showed that although the flow bias still existed, it was reduced from ~2:1 to ~1.25:1.

When the outer annulus flow field was characterized using the Pitot tube measurements, its behavior was consistent with typical bluff body flows. It clearly exhibited the recirculation, transition and established flow zones characteristic for buff body flows. At a mass flow rate of 1500 SLPM, the nozzle showed a maximum negative velocity of -52 m/s in the recirculation zone at only 0.2 L/D and a maximum positive velocities of 123 m/s at the exit plane and 90 m/s at 2 L/D in the established flow zone. Although this outer annulus was originally designed to provide a buffer of clean air around the central jet, its unique flow characteristics would make for interesting flow visualizations given time.

Coflow Visualizations

Flow visualizations were generated while the outer annulus was set at a flow rate of 250 SLPM (~20 m/s) and the central jet was flow rate was varied from 200 (~32 m/s) to 1500 SLPM (~232 m/s) . The data collected from the filtered Rayleigh scattering images generated results that were somewhat unexpected, although not incorrect. There were two main trends that stood out in the flow rate vs. normalized intensity curves shown in Figures 56 and 57. The first trend is that as the flow rate increased from 200 SLPM up to 900 SLPM, the intensity ratio decreased from ~0.6 to ~0.5. The second trend was that further increases in flow rate from 900 SLPM to 1500 SLPM caused a substantial increase in intensity ratio from ~0.5 to 0.9. At the higher flow rates, particles became more prominent and the received scattering signal was directly related to flow rate.

The trends seen in the flow rate vs. intensity ratio curves were somewhat unexpected, although there is a reasonable explanation for them. For both the observed

90

trends to be true, the laser frequency would have to be close to the lower frequency edge of the absorption notch, although still inside. Also, the iodine absorption notch would have to be relatively narrow. The combination of these two conditions would lead to the trends seen in the experimental data.

As the central jet flow rate (velocity) is increased, the Rayleigh scattered signal is positively Doppler shifted further into the iodine absorption well. Because the center of the well has stronger absorption characteristics, the received scattering signal would be reduced. But because the relationship between flow velocity and scattered signal inflects at a flow rate of ~900 SLPM, this indicates that the absorption notch is narrow.

Although the laser frequency and iodine absorption versus frequency curve were not known, their relative positions are. The experimental method of setting the laser frequency strongly indicates that it is just inside the low frequency edge of the absorption notch. The mode-tune program is aborted at 53.145 C, just prior to any visible absorption effects. Once the laser stabilizes however, its output frequency has moved into the leading edge of the well.

Given that the filter absorption notch in question is likely narrow, it would allow for increasingly Doppler shifted signals to pass from the low to high frequency edges of the notch. Initially increases in flow velocity would decrease the FRS signal, then it would plateau. Further then increases in flow velocity would increase the FRS signal. In addition to this, it is assumed that the flow has a Gaussian particle velocity distribution profile. At higher flow velocities, there is a larger deviation from flow maximum to minimum velocity. Because of this Gaussian profile, even though the bulk of the flow still exists inside the notch, the Mie scattering signal caused by faster particles shifted

outside the notch would cause sharp fluctuations in the received FRS signal. This conjecture is further supported by the fact that the normalized value of filtered to unfiltered signals at high flow rates approaches unity which suggests an unfiltered flow; a condition that would exist if the flow had been Doppler shifted entirely through the iodine absorption well.

It is clear that the received signal in this experiment is highly influenced by particle scattering. This Mie scattering from dust particles in the laboratory air was seen in every test condition used. Although most images were averaged to generate a more regular data set, that did not eliminate the prevalence of the particles in the flow. This fact is highlighted by the received intensity fluctuations seen in the high flow rate data sets. These particle scattering induced fluctuations exist even though the building air supply is well filtered and the images are time averaged. What differentiates the particle scattering from the Rayleigh scattering is its relatively strong intensity, discreteness and random location.

Outer Annulus Flow Visualization

As stated earlier, running at 250 SLPM outer annulus flow yielded results that were counter intuitive. Although the flow field was expected to be positive, the increase from no flow to 250 SLPM outer annulus flow caused an increase in FRS signal. Two separate explanations for this interesting result rely on a combination of several underlying factors.

One possibility is although a 1500 SLPM outer flow field had already transitioned to positive flow by 0.4 L/D, this does not suggest that a lower velocity flow would have the same transition point. The cause for the recirculation zone in bluff body flows is flow

separation due to strong pressure gradients at the exit plane between the flow exiting the inside of the annular region and the adjacent internal flow field. A slower flow would have reduced pressure gradients and would prolong separation causing the area of recirculation to extend further downfield.

Although the other flows imaged had a central jet flow that produced a smoother flow, the 250 SLPM outer annulus flow did not. This flow condition would be typical of a bluff body flow that commonly have upwards of 30 percent turbulence intensity. This relatively large flow turbulence would lead to a much larger distribution in particle velocities. Given the high flow turbulence and extended recirculation zone resulting from this particular flow, it is very likely that some portion of the flow has a negative velocity at one diameter from the exit plane.

Assuming that there are reversed flow particles in the flow field, the particles would easily be shifted out of the absorption notch of the iodine filter. Because the laser was set very close to the low frequency edge of the filter, even a slow reversed flow may shift the particles back outside the absorption notch. The combination of these flow conditions leads to an increase in received FRS signal when operating the outer annulus at 250 SLPM with no central jet flow.

The second explanation for the increase in scattering intensity due to the addition of a 250 SLPM outer annulus flow field is based on the existence of particles in the flow. The addition of a 250 SLPM flow field over quiescent conditions may lead to an increase in particle motion through the region of interest. This may be due to either particles in the experimental air, or particle entrainment caused by the turbulent flow field. In either

case, the increase of particle motion through the region of interest will lead to an increase in Mie scattering and the resultant received signal intensity.

Experimental Component Performance

One aspect of this work was to determine the performance of the experimental components of the FRS system, many of which were previously untested. This testing was not only relevant to current work, but also for future work utilizing components of this experimental setup.

Frame Rate

An important characteristic of a FRS system is the rate it can record images. Not only does a faster frame rate decrease the time it takes to conduct an experiment, but it can also lead to time resolved data and reduced particle influence. Although most of the data presented in this paper is time averaged, the laser power and flow velocities studied were sufficient to gather data at 100 Hz. This data was averaged to reduce the significance of particle induced Mie scattering in the flow. Data was taken at a maximum rate of 1 kHz in several instances and the filtered Rayleigh scattered signal was still discernable from the background, although extracting data may prove difficult.

Laser Power

The Coherent Sabre-R series argon ion laser is rated at 15 Watts in multi-line operation, 4.2 watts for the experiment required single-line, single-mode operation. Although the manufacturers specification was 4.2 watts, the laser produced anywhere from 5 to 9.2 watts in single-line, single-mode operation, with the power output dependent on the laser intercavity etalon temperature. Initial testing was conducted as a

reduced power of ~1.2 watts and later increased once it was clear there was no danger to the test equipment or camera. By increasing the laser from ~1.2 to ~5.9 watts at an etalon temperature of 53.145 C, the scattered signal was increased dramatically with only a slight increase in noise. Because of this, its seems clear that at whatever etalon temperature testing is conducted at in the future, the laser should be set to its maximum power.

Laser Stability

Another highlight of the Coherent laser is its apparent long term frequency and power stability.   Any significant deviation in laser output frequency would lead to a change in received background scattering as viewed by the camera through the filter. Comparing pictures from the beginning and end of a test session show no perceptible change in background noise even over the course of several hours.

Iodine Filter Cell Characteristics

The performance of the FRS system as a whole depends strongly on the ability of the iodine filter to provide strong and repeatable absorption over a specified frequency span. On every occasion of testing, the laser was run through the mode-tune program to check for the location, with respect to etalon temperature, of the iodine absorption wells. Their location and intensity was quite consistent, although possibly less than ideal in intensity. The cell was determined to have ~60-65% absorption of incident light at ~514.5 nm at the notch located at a laser etalon temperature of 53.145 C. Although this was sufficient for testing for bulk characteristics of a flow, it would make more quantitative results such as flow velocity and density more difficult. It is quite possible

that the notch used in this experiment has poorer absorption qualities than others in this frequency range, and further investigation into the other two observed notches is warranted. More beneficial to future testing, however, would be to use an iodine cell capable of filtering out a higher percentage of the incident light frequency. This cell would either have to be filled with a higher iodine density, be longer, or a combination of both. It is also clear that the particular absorption notch selected would be ill-suited for flows much greater than Mach number ~0.6 because of its apparent narrowness.

Repeatability

One important quality in research is that the experimental should be repeatable. On many separate days the same relationship between iodine absorption and etalon temperature were displayed with no perceptible changes. In addition to this, the experiment itself was repeated several times with results that although quantitatively were different, were qualitatively the same. Testing yielded the same trends at ~1.2 watts as it did at ~5.9 watts, although the data was understandably different. Simple qualitative and quantitative tests also showed no perceptible changes on two separate days of testing at ~5.9 watts.

VI. Conclusions

The coflow nozzle used in this experiment had a strong asymmetry for the outer annulus flow field. This asymmetric flow was analyzed through the use of a CFD program and the nozzle was redesigned to reduce the magnitude of asymmetry. The redesigned nozzle was built and experimental testing compared well to the CFD results. The outer annulus flow field asymmetry was reduced from ~2:1 to ~1.25:1 following the nozzle redesign.

Flow visualizations were generated using the argon-ion laser throughout a range of nozzle flow rates. The laser was set to an etalon temperature of 53.145 C and output powers of 1.2 and 5.9 watts. By increasing the power from 1.2 to 5.9 watts, the received signal increased by approximately five fold with only a sight increase in noise level. For most flow visualizations the images were captured at a frame rate of 100 Hz, although frame rates as fast as 1 kHz were possible. The flow visualizations showed a relationship between flow velocity and received scattering signal that was both clear and repeatable. Unfortunately, the images collected showed significant particle influence and the Rayleigh scattering signal was interlaced with a strong Mie scattering signal.

Because the flow visualizations showed significant particle influence, the filtered images were normalized by a set of unfiltered images for the same flow rates. Plots of the ratio of filtered to unfiltered intensity showed slight decreases in the intensity ratio (~0.6 to ~0.5) resulting from an increase in central jet flow rate from 200 SLPM to 900 SLPM. Further increases in central jet flow rate from 900 SLPM to 1500 SLPM resulted in an increase in intensity ratio from ~0.5 to ~0.9. This indicates that the 1500 SLPM (232 m/s) central jet flow may have Doppler shifted the scattered signal almost entirely

through the iodine absorption well. Because the maximum ~232 m/s central jet velocity corresponds to an ~0.41 GHz Doppler shift, the filter absorption well is assumed to be only marginally broader than ~0.41 GHz. When comparing the ratio of filtered to unfiltered intensities of the images along the laser line but away from the region of flow, the iodine cell exhibited approximately 60 to 65 percent absorption.

Because this experimental setup will likely be used in future research, four key suggestions for future research exist. First, the specific absorption characteristics of the iodine filter used in this experimental setup are still unknown. All that is known currently is a range of laser etalon temperatures that correspond to reduced incident light transmission. Ideally, a direct frequency measurement device and the relationship of filtered to unfiltered signal intensity would allow for a thorough development of the frequency versus transmission curve for the filters used.

Next, although the camera sensitivity and laser output power facilitated frame rates of up to 1kHz, the existence of high particle density in the flow drastically reduced the effective data acquisition rate. In most cases, the 100Hz data had to be averaged over hundreds of images to reduce the appearance of particles in the images. In the future, effort should be made to reduce the particle density both in the laboratory environment as well as in the high pressure air supply.

Further investigation into different data reduction techniques in warranted. To reduce the strong yet random influence of particles on the flow visualizations, the data was averaged producing a more consistent data set. However, different methods of post processing may allow for elimination of the Mie scattering signal before image

averaging. This would produce a data consisting of more pure Rayleigh scattering and facilitate further quantitative analysis.

Finally, the molecular iodine filter needs to be more thoroughly characterized. The filter showed a maximum absorption of ~60-65 percent at a laser power of 5.9 watts and an etalon temperature of 53.145 C. Although this absorption percentage was acceptable for performing the flow visualizations reported here, it may be insufficient to accurately extract flow velocity or thermodynamic properties. If these absorption percentages are confirmed, the current iodine cell should be replaced with one that provides a higher absorption percentage at the corresponding laser power and frequency.

Bibliography

Boguszko, M. Elliott G. Carter, C. "Filtered Rayleigh Scattering for Fluid/Thermal Systems." 22nd AIAA Aerodynamic Measurement Technology and Ground Testing Conference. June 24-27, 2002. St. Louis, Missouri.

Chiang, T.P. and Sheu Tony W. H. "Bifurcations of Flow Through Plane Symmetric Channel Contraction." Journal of Fluids Engineering. June 2002, vol. 124. pp. 444-451.

Davies, T.W., Beér, J.M., "Flow in the Wake of Bluff-Body Flame Stabilizers", Thirteenth Symposium (International) on Combustion, The Combustion Institute, pp. 631-638 (1971)

Durao, D. F. G., and Whitelaw, J. H., 1978, ''Velocity Characteristics of the Flow in the Near Wake of a Disk,'' Journal of Fluid Mechanics., 85, pp. 369–385.

Eckbreth, Alan, C. "Diagnostics for Combustion Temperature and Species." 2nd ed. Garden & Breach Publishers, 1996.

Elliott, Gregory S. Boguszko, Martin. "Filtered Rayleigh Scattering: Toward Multiple Property Measurements (Invited)." 39th AIAA Aerospace Sciences Meeting & Exhibit. 8-11 January 2001. Reno, NV.

Elliott, Gregory S. Huffman, Rich. Boguszko, Martin. "Property and Velocity Measurements in a Supersonic Flow." 44th AIAA Aerospace Sciences Meeting and Exhibit, 9-12 January 2006, Reno, NV

Elliott, Gregory. Samimy, Mo. "Rayleigh Scattering Technique for Simultaneous Measurements of Velocity and Thermodynamic Properties" AIAA Journal Vol. 34, No 11, November 1996

Fluent 5 User's Guide. Fluent Incorporated. Lebanon New Hampshire, 1998

Gridgen User Manual, Version 15. Pointwise Incorporated. Fort Worth Texas. 2005

Helmholtz, Über diskontinuierliche Flüssigkeitsbewegungen, Monatsberichte der königlichen Akademie der Wissenschaften zu Berlin, 1868.

Helmholtz, Zur Theorie freier Flüssigkeitsstrahlen, Borchardt's Journal, 70, 1869.

Kirchhoff, Vorlesungen über Mathematische Physik, 21.Vorl., 1876

Ko, N. W. M., and Chan, W. T., 1978, ''Similarity in the Initial Region of Annular Jets: Three Configurations,'' Journal of Fluid Mechanics., 84, pp. 641–656.

Literature Review. University of North Carolina. http://www.unc.edu/depts/ wcweb/handouts/literature_review.html. 5 January, 2006.

McAlister, Sue. "From Einstein to Star Wars." Monash University. Issue 6, 2002.

Meyers, James F. "Development of Doppler Global Velocimetry as a Flow Diagnostics Tool" Measurement Science and Technology. 6 769–83 Fall 1995

Elliott Gregory S. and Beutner Thomas J. "Molecular Filter-Based Planar Doppler Velocimetry" Progress in Aerospace Sciences. Volume 12, Number 4. 2001

Miles Richard B, Forkey Joseph N and Lempert Walter R. "Filtered Rayleigh Scattering Measurements in Supersonic/Hypersonic Facilities." AIAA Paper AIAA-92-3894

Miles, Richard B. et al. "Flow Field Imaging Through Sharp-Edged Atomic and Molecular 'Notch' filters". Institute of Physics Publishing. Measurement Science and Technology. 12(2001) 442-451. 5 January 2001

Miles, Richard B, Lempert, Walter R. Forkey, Joseph, N. "Laser Rayleigh Scattering." Institute of Physics Publishing. Measurement Science and Technology. 12(2001) R33-R51. 13 February 2001.

Milonni, Peter W, Eberly, Joseph H. Lasers. A Wiley-Interscience Publication. John Wiley and Sons Inc. 1998, USA

Operator's Manual. The Coherent INNOVA Sabre-R Series Ion Laser Coherent Inc. 2001, USA

Panda, Jayanta. Gomez, Carlos R. "Setting up a Rayleigh Scattering Based Flow Measuring System in a Large Nozzle Testing Facility." NASA Technical Memorandum 211985. November, 2002.

Pinho, F. T.,Whitelaw, J. H., "Flow of Non-Newtonian Fluids Over A Confined Baffle" Journal of Fluid Mechanics., 226, pp. 475–496. 1991.

Prandtl, Ludwig. "Essentials of Fluid Dynamics." Hafner Publishing Company, New York. 1952.

Seasholtz, Richard G. and Buggele, Alvin E. "Improvement in Suppression of Pulsed Nd:YAG Laser Light With Iodine Absorption Cells for Filtered Rayleigh Scattering Measurements." NASA Technical Memorandum 113177. November, 1997.

Seasholtz, Richard G., Greer, Lawrence C., III. "Rayleigh Scattering Diagnostic for Measurement of Temperature and Velocity in Harsh Environments" NASA Technical Memorandum 1998-206980. April, 1998.

Seasholtz, Richard G., Greer, Lawrence C., III. "Rayleigh Scattering Measurement of Temperature and Velocity." AIAA Paper 98-0206; April 1998.

Schlichtin, Hermann. Krause, Egon. "Boundary Layer Theory." 8th ed. Revised. Springer-Verlag, LLC. December, 1999. New York.

Shimizu H, Lee S A and She C Y. High Spectral Resolution LIDAR System with Atomic Blocking Filters for Measuring Atmospheric Parameters. Applied Optics. 1983, 22, 1373.

Taylor, A. M. K. P., and Whitelaw, J. H., 1984, "Velocity Characteristics in the Turbulent Near Wakes of Confined Axisymmetric Bluff Bodies" J. Fluid Mech., 139, pp. 391–416.

Appendix A- Sample Traverse Control Computer Code

```
;;DAVID MICELI
;;1/11/06
;;THIS PROGRAM SWEEPS THE TRAVERSE THROUGH A 3-D GRID
HOME X Y Z
G90         ;Absolute MODE
G0 X-128 Y-15 Z15      ;SET POSITION AT 0,0,0
G92 X0 Y0 Z0      ;SOFTWARE HOME HERE

G91         ;Incremental MODE
G71         ;METRIC MODE
G75         ;UNIT/MIN
G84 X Y     ;ROTATION OFF FOR  X Y
ENABLE X Y
RapidFeedRate.X=1500   ;SET FEEDRATE FOR G0 COMMANDS
RapidFeedRate.Y=1500

G4 F1.0 ; sample initial point
; X CONTROL LOOP
RPT 5
      ;Z CONTROL LOOP
      RPT 31
            ;Y CONTROL LOOP
            RPT 30
            G0 Y1         ; SWEEP PROBE SIDE TO SIDE
            G4 F1.5   ; sample a point
            ENDRPT
      G0 Y-30 Z-1          ; BRINGS PROBE BACK TO INITIAL Y AND DOWN
      G4 F1.5   ; sample a point
   ENDRPT
```

GO Z31 X25 ; BRINGS PROBE BACK TO INITIAL Z AND DOWNSTREAM

G4 F1.5   ; sample a point

ENDRPT

Appendix B- Laser Operation

Start-Up Procedure

- Enable the primary supply of facility cooling water to the Sabre R Series heat exchanger. Note that the temperature regulation valve of the primary loop may inhibit flow until the system is ionized.

- Ensure that the keyswitch, located on the font panel of the power supply, is in the LASER OFF position. Turn on the facility circuit breaker to establish main line power

- Turn the keyswitch to the ON position. Wait for the remote control module to power up. The two indicator LEDs on the front panel of the power supply should be on.

- If sensitive optical elements exist in the output beam path and Auto Shutter is disabled, close the external shutter to protect from a possible momentary output power surge at the onset of ionization.

- Press the ON/OFF button on the remote to initiate the start delay sequence.

- Wait 25 seconds and listen to hear the supply main contactor engage.

- Wait 50 seconds more and the starter will fire resulting in ionization of the plasma tube.

- After lasing has been achieved, use the LIGHT button on the remote to select either Light or Current Regulation Mode. Use the UP/DOWN arrows to select the desired light or current setting. Select the desired aperture setting.

- Open the external shutter, if applicable, to allow the output beam to exit the laser head.

Shut-Down Procedure

- Press the ON/OFF button on the remote control module to shut the system down. This will disengage the power supply main contactor and de-ionize the plasma tube.

- Turn the keyswitch, located on the front panel of the power supply to the OFF position.

- The pump in the heat exchanger will continue to circulate the water in the secondary cooling loop for five minutes after the laser has been de-ionized. Maintain facility power and primary cooling water during this cool down period.

- Turn off the facility circuit breaker.

- Turn off the primary supply of facility cooling water to prevent over-pressurization of the heat exchanger primary cooling loop and temperature regulation valve.

Emergency Shutdown

Press the ON/OFF button on the remote control module to shut the system down

Safety

When working with any laser there are certain guidelines to follow to ensure safety and avoid possible bodily harm, especially to the eyes. These rules become increasingly important as the laser power increases. The laser used in these experiments is a class IV

Argon laser operating at 514.5 nm, which is well within the visible spectrum of light. Because of this, there are several guidelines that need to be followed:

- Use protective eyewear designed for laser wavelength whenever laser is in use

- Do not remove protective covers from laser head. During normal operation, internal reflections are confined within the laser head and pose no safety hazard.

- Never look directly into the laser output port when the power is on

- Do not stare at laser light reflected from any surface

- Avoid operating the laser in a darkened environment

- Do not use the laser in the presence of flammables, explosives, or volatile solvents such as alcohol, gasoline or ether.

- Do not wear clothing with reflective surfaces

- Avoid entering beam path

Appendix C- Additional FRS Images and Comment

Shown below in Figure 61 is an image captured with the camera lens cap in place. Note the much higher intensity at the top of the image; it is believed that this is due to uneven cooling of the digital camera.
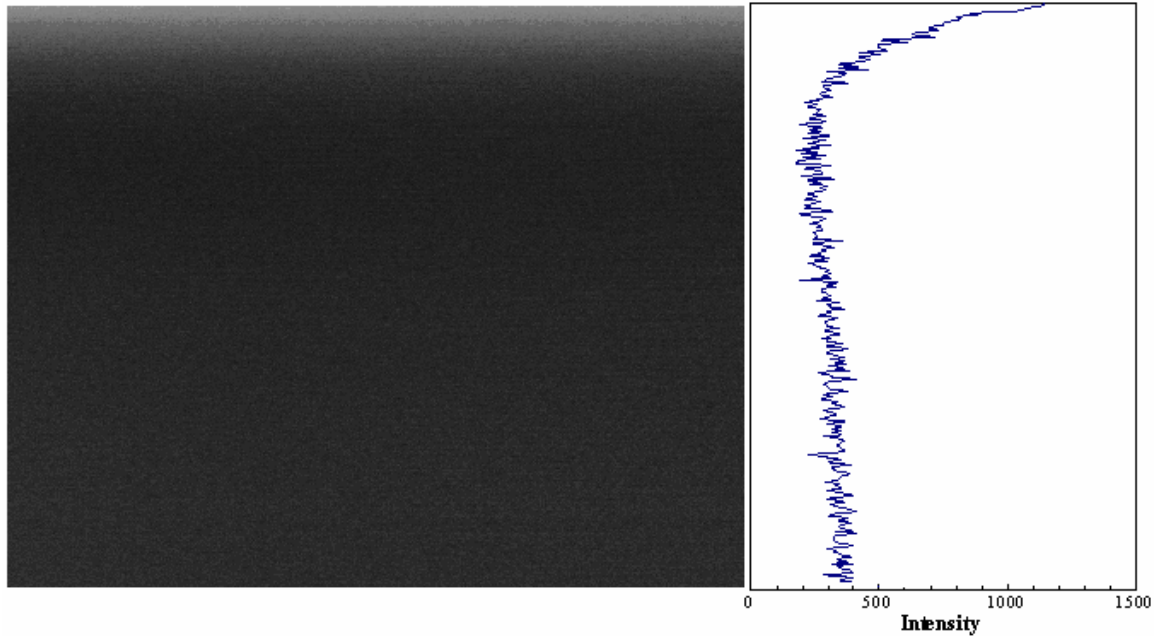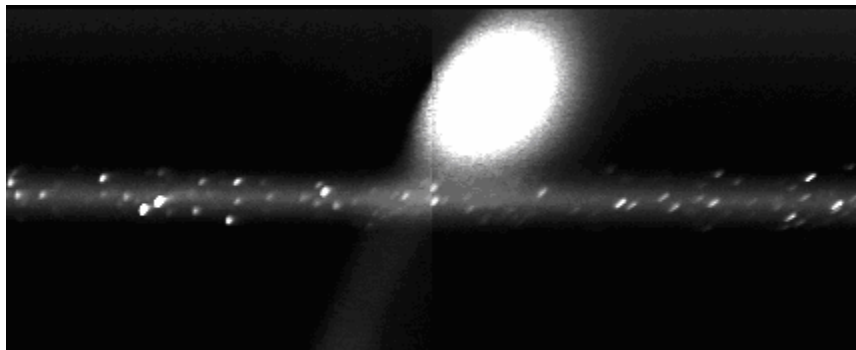

Figure 61- Image taken with camera lens cap on.

Figure 62- Initial camera images of laser line with no flow using the less dense iodine filter-Dual Dac

The first issue was the existence of several large sources of reflected laser light. Seen above in Figure 62 is one of the first images captured with the camera showing a strong reflection coming from a high pressure air hose fitting It is clear that such a

reflection would render any data taken nearly worthless. To remove this reflection, a black cloth was draped over the nozzle and stagnation chamber. To reduce ambient light in the lab, all overhead lights were extinguished and a laser curtain was positioned between the computer monitor and the experiment. In addition to this, two stray, but significant, beams were traced from the laser head and terminated into non reflective material.

Once the reflected and ambient light sources had been reduced, it next came apparent that the low pressure iodine filter was less effective than anticipated. At this point the filter was replaced with a similar filter containing higher pressure iodine. The filter was heated to 80 degrees C and initial images were taken of a no-flow condition. The change in filters caused a significant reduction in incident light intensity. Subsequently increasing the filter temperature to 110 C also increased the iodine absorption, as expected. Shown below is a no flow image of the 1.2 watt laser line through the 110 C high pressure iodine cell at a frame rate of 100 Hz.
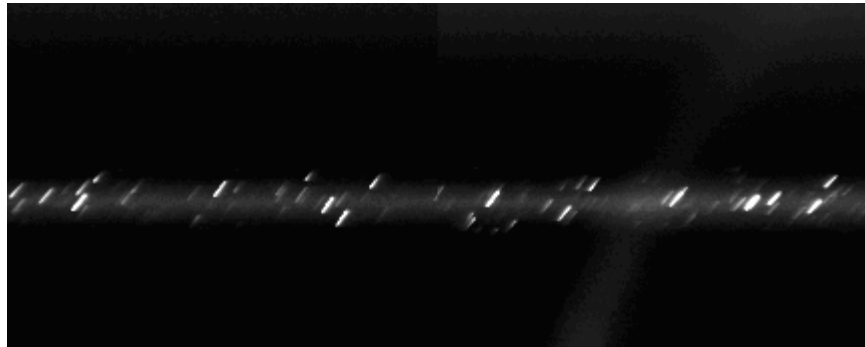

Figure 63- Image of laser line with no flow using the more dense iodine filter- Dual Dac

Attempts to gather data in close proximity to the coflow nozzle exposed another issue in the experimental setup. The PCO.4000 digital camera's default mode of operation utilizes dual digital to analog converters, one for each half of the image, split

vertically. Although that reduces the load on each DAC and facilitates high frame rates

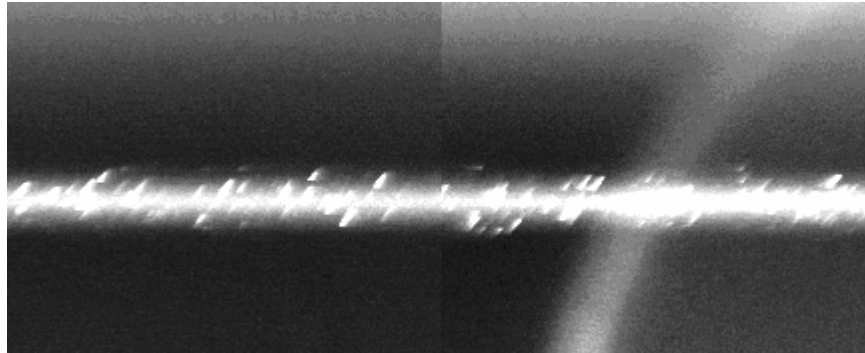for large images, it also produces a significant asymmetry in the image, as seen below.

Figure 64- Image highlighting the problem inherent in using a dual DAC image processor.

While operating in dual DAC mode, the data was unacceptably discontinuous from

left to right, resulting in only one DAC being employed for the duration of testing.

Although this action could potentially reduce the image quality, because the region of

interest for this experiment is only 1.35% of the maximum for the camera, it was deemed

an acceptable action.

Shown below are additional post processed images not included in the body of
this paper.
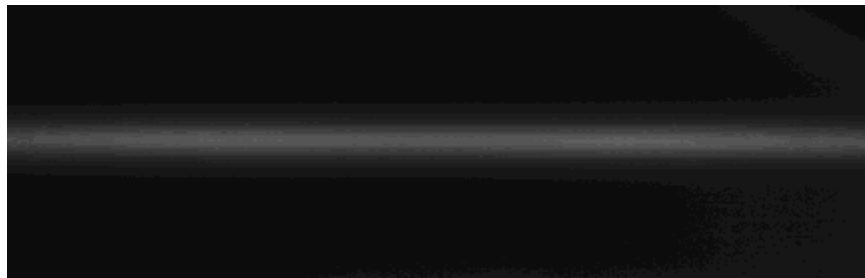
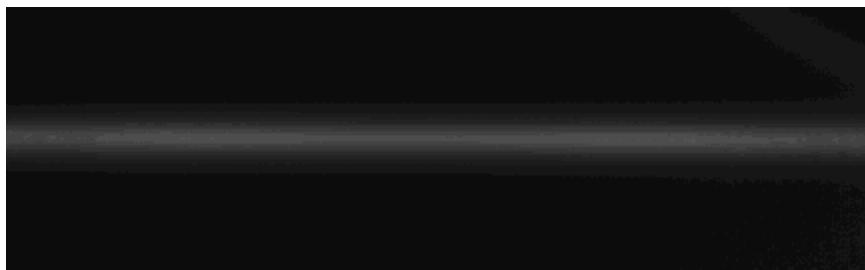**Figure 65- Averaged filtered image of 250 SLPM outer annulus and 200 central jet flow rates**

Figure 66 Averaged filtered image of 250 SLPM outer annulus and 400 central jet flow rates
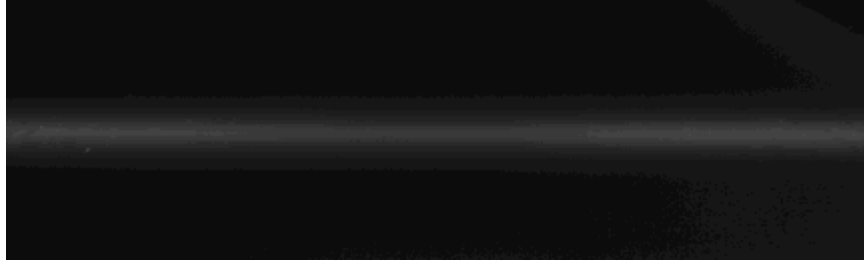
Figure 67 Averaged filtered image of 250 SLPM outer annulus and 600 central jet flow rates
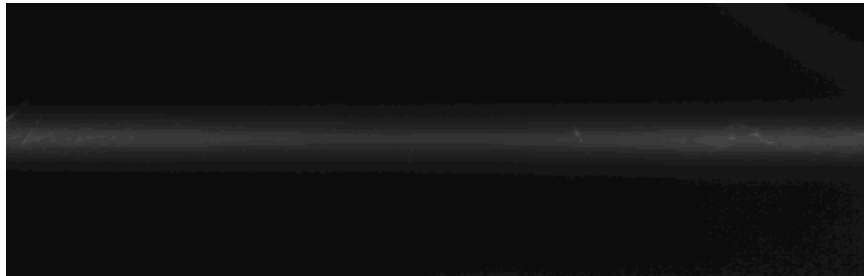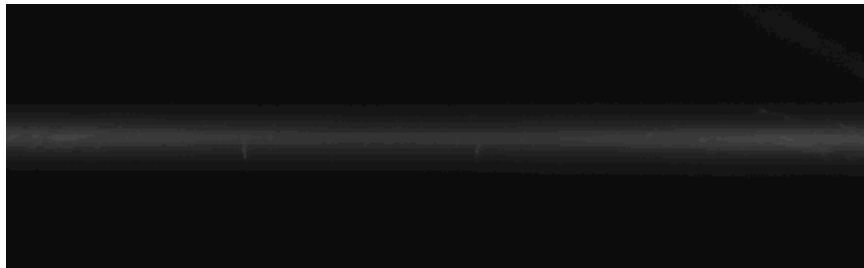

Figure 68 Averaged filtered image of 250 SLPM outer annulus and 800 central jet flow rates

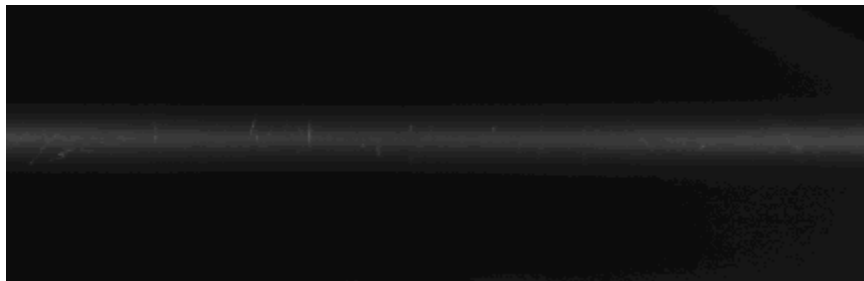**Figure 69 Averaged filtered image of 250 SLPM outer annulus and 900 central jet flow rates**

Figure 70 Averaged filtered image of 250 SLPM outer annulus and 1000 central jet flow rates
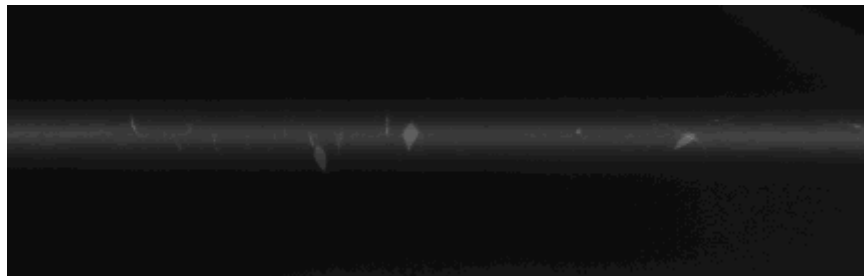

Figure 71 Averaged filtered image of 250 SLPM outer annulus and 1100 central jet flow rates
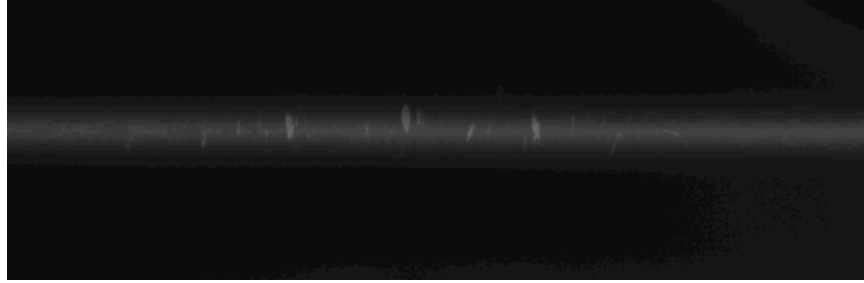
Figure 72 Averaged filtered image of 250 SLPM outer annulus and 1200 central jet flow rates
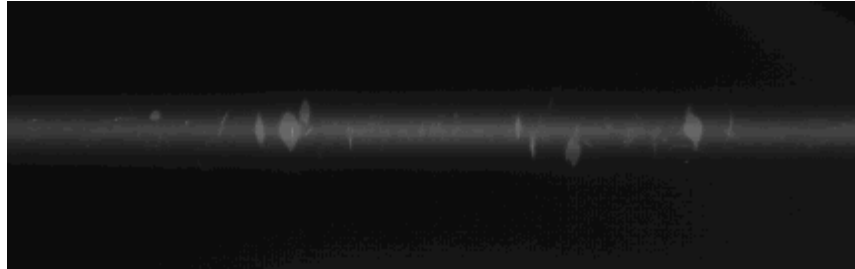

Figure 73 Averaged filtered image of 250 SLPM outer annulus and 1300 central jet flow rates
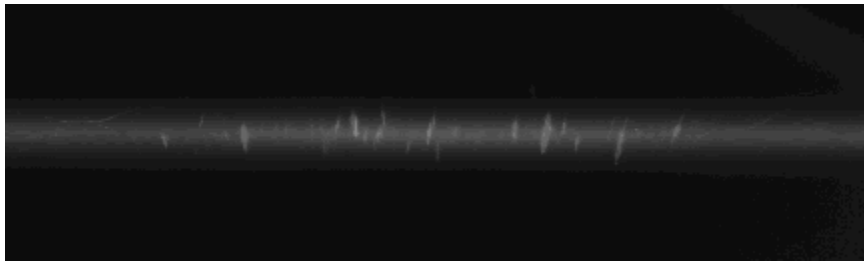

Figure 74 Averaged filtered image of 250 SLPM outer annulus and 1400 central jet flow rates
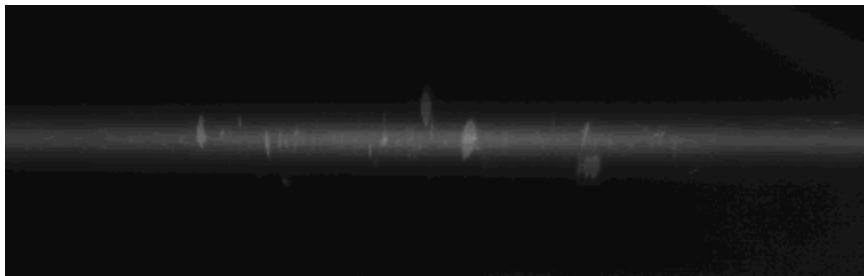

Figure 75 Averaged filtered image of 250 SLPM outer annulus and 1500 central jet flow rates
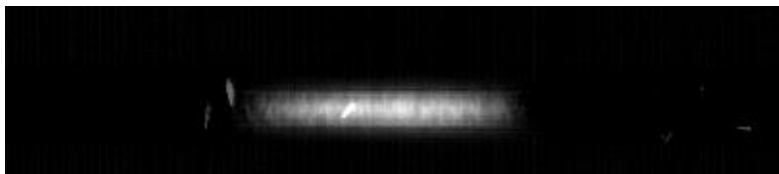

Figure 76- Relative intensity image from subtraction of 200 SLPM central jet flow from the baseline image.

Figure 77- Relative intensity image from subtraction of 400 SLPM central jet flow from the baseline image.
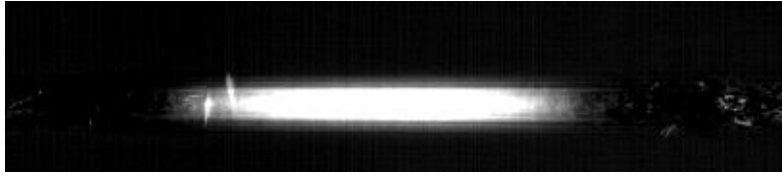

Figure 78- Relative intensity image from subtraction of 600 SLPM central jet flow from the baseline image.
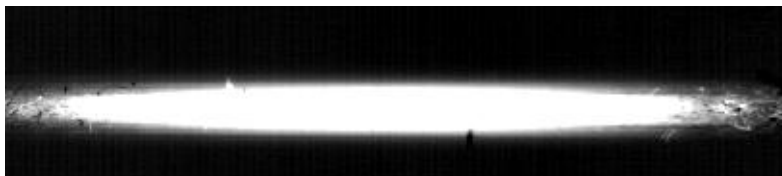

Figure 79- Relative intensity image from subtraction of 800 SLPM central jet flow from the baseline image.
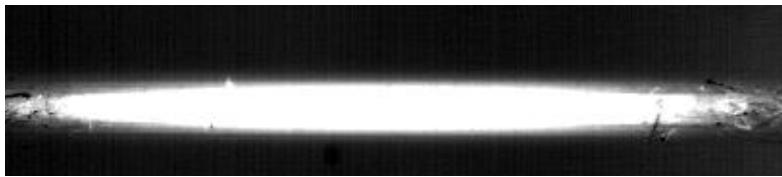

Figure 80- Relative intensity image from subtraction of 900 SLPM central jet flow from the baseline image.

Appendix D- Matlab Code for Image Post-Processing

```
%%%%%%%%%%%%%David Miceli
%%%%%%%%%%%%%Matlab code used to read Tif files from camera,
%%%%%%%%%%%%%convert the files into matracies, perform algebra
%%%%%%%%%%%%%on the matracies then generate plots from the resulting
%%%%%%%%%%%%%matracies

clc  %%%%%%%%%%Clears command window

Noflowatall_0001=imread('Noflowatall_0001.tif');
Noflowatall_0002=imread('Noflowatall_0002.tif');
Noflowatall_0003=imread('Noflowatall_0003.tif');
Noflowatall_0004=imread('Noflowatall_0004.tif');
Noflowatall_0005=imread('Noflowatall_0005.tif');
Noflowatall_0006=imread('Noflowatall_0006.tif');
Noflowatall_0007=imread('Noflowatall_0007.tif');
Noflowatall_0008=imread('Noflowatall_0008.tif');
Noflowatall_0009=imread('Noflowatall_0009.tif');
Noflowatall_0010=imread('Noflowatall_0010.tif');
Out250in1000_0001=imread('Out250in1000_0001.tif');
Out250in1000_0002=imread('Out250in1000_0002.tif');
Out250in1000_0003=imread('Out250in1000_0003.tif');
Out250in1000_0004=imread('Out250in1000_0004.tif');
Out250in1000_0005=imread('Out250in1000_0005.tif');
Out250in1000_0006=imread('Out250in1000_0006.tif');
Out250in1000_0007=imread('Out250in1000_0007.tif');
Out250in1100_0001=imread('Out250in1100_0001.tif');
%% Reading continues….

%%%%%%%%Averaging for the Unfiltered Case%%%%%%%%%%%%%%%%%%%%%%%
avgNoflowUNFILT=(Noflow_0001+Noflow_0002+Noflow_0003+Noflow_0004+Noflo
w_0005+Noflow_0006+Noflow_0007+Noflow_0008+Noflow_0009)/9;
avgO250i1000UNFILT=(O250i1000_0001+O250i1000_0002+O250i1000_0003+O250i
1000_0004+O250i1000_0005+O250i1000_0006+O250i1000_0007)/7;
avgO250i1100UNFILT=(O250i1100_0001
+O250i1100_0002+O250i1100_0003+O250i1100_0004+O250i1100_0005+O250i1100_
0006)/6;
avgO250i1200UNFILT=(O250i1200_0001+O250i1200_0002+O250i1200_0003+O250i
1200_0004+O250i1200_0005+O250i1200_0006+O250i1200_0007)/7;
avgO250i1300UNFILT=(O250i1300_0001+O250i1300_0002+O250i1300_0003+O250i
1300_0004+O250i1300_0005+O250i1300_0006+O250i1300_0007+O250i1300_0008+
O250i1300_0009)/9;
```

avgO250i1400UNFILT=(O250i1400_0001+O250i1400_0002+O250i1400_0003+O250i1400_0004+O250i1400_0005+O250i1400_0006+O250i1400_0007+O250i1400_0008+O250i1400_0009)/9;
avgO250i1500UNFILT=(O250i1500_0001+O250i1500_0002+O250i1500_0003+O250i1500_0004+O250i1500_0005+O250i1500_0006)/6;
avgO250i200UNFILT=(O250i200_0001+O250i200_0002+O250i200_0003+O250i200_0004+O250i200_0005)/5;
avgO250i400UNFILT=(O250i400_0001
+O250i400_0002+O250i400_0003+O250i400_0004+O250i400_0005+O250i400_0006+O250i400_0007+O250i400_0008+O250i400_0009)/9;
avgO250i600UNFILT=(O250i600_0001+O250i600_0002+O250i600_0003+O250i600_0004+O250i600_0005+O250i600_0006+O250i600_0007+O250i600_0008+O250i600_0009)/9;
avgO250i800UNFILT=(O250i800_0001+O250i800_0002+O250i800_0003+O250i800_0004+O250i800_0005+O250i800_0006+O250i800_0007+O250i800_0008+O250i800_0009)/9;
avgO250i900UNFILT=(O250i900_0001+O250i900_0002+O250i900_0003+O250i900_0004+O250i900_0005+O250i900_0006+O250i900_0007+O250i900_0008+O250i900_0009)/9;
avgOuter250OnlyUNFILT=(Outer250av_0001+Outer250av_0002+Outer250av_0003+Outer250av_0004+Outer250av_0005+Outer250av_0006)/6;

%%%%%%%%%%%%%%%%Averaging for the filtered
case%%%%%%%%%%%%%%%%%%%%%%
avgO250=(O250_0001+O250_0002+O250_0003+O250_0004+O250_0005+O250_0006+O250_0007+O250_0008+O250_0009+O250_0010)./10;
avgOuter1000=(Outer1000_0001+Outer1000_0002+Outer1000_0003+Outer1000_0004+Outer1000_0005+Outer1000_0006+Outer1000_0007+Outer1000_0008)./8;
avgOuter1500=(Outer1500_0001+Outer1500_0002+Outer1500_0003+Outer1500_0004+Outer1500_0005+Outer1500_0006+Outer1500_0007+Outer1500_0008+Outer1500_0009+Outer1500_0010)./10;
avgOuter250=(Outer250_0001+Outer250_0002+Outer250_0003+Outer250_0004+Outer250_0005+Outer250_0006+Outer250_0007+Outer250_0008+Outer250_0009+Outer250_0010)./10;
avgOuter500=(Outer500_0001+Outer500_0002+Outer500_0003+Outer500_0004+Outer500_0005+Outer500_0006+Outer500_0007+Outer500_0008+Outer500_0009+Outer500_0010)./10;
avgNoflowatall=(Noflowatall_0001+Noflowatall_0002+Noflowatall_0003+Noflowatall_0004+Noflowatall_0005+Noflowatall_0006+Noflowatall_0007+Noflowatall_0008+Noflowatall_0009+Noflowatall_0010)./10;
avgOut250in1000=(Out250in1000_0001+Out250in1000_0002+Out250in1000_0003+Out250in1000_0004+Out250in1000_0005+Out250in1000_0006+Out250in1000_0007)./7;
avgOut250in1100=(Out250in1100_0001+Out250in1100_0002+Out250in1100_0003+Out250in1100_0004+Out250in1100_0005+Out250in1100_0006)./6;

avgOut250in1200=(Out250in1200_0001+Out250in1200_0002+Out250in1200_0003+Out250in1200_0004+Out250in1200_0005+Out250in1200_0006+Out250in1200_0007+Out250in1200_0008)./8;
avgOut250in1300=(Out250in1300_0001+Out250in1300_0002+Out250in1300_0003+Out250in1300_0004+Out250in1300_0005+Out250in1300_0006+Out250in1300_0007+Out250in1300_0008)./8;
avgOut250in1400=(Out250in1400_0001+Out250in1400_0002+Out250in1400_0003+Out250in1400_0004+Out250in1400_0005+Out250in1400_0006+Out250in1400_0007)./7;
avgOut250in1500=(Out250in1500_0001+Out250in1500_0002+Out250in1500_0003+Out250in1500_0004+Out250in1500_0005)./5;
avgOut250in200=(Out250in200_0001+Out250in200_0002+Out250in200_0003+Out250in200_0004+Out250in200_0005+Out250in200_0006+Out250in200_0007+Out250in200_0008+Out250in200_0009+Out250in200_0010+Out250in200_0011+Out250in200_0012+Out250in200_0013+Out250in200_0014)./14;
avgOut250in400=(Out250in400_0001+Out250in400_0002+Out250in400_0003+Out250in400_0004+Out250in400_0005+Out250in400_0006+Out250in400_0007+Out250in400_0008+Out250in400_0009+Out250in400_0010)./10;
avgOut250in600=(Out250in600_0001+Out250in600_0002+Out250in600_0003+Out250in600_0004+Out250in600_0005+Out250in600_0006+Out250in600_0007+Out250in600_0008+Out250in600_0009+Out250in600_0010+Out250in600_0011+Out250in600_0012+Out250in600_0013)./13;
avgOut250in800=(Out250in800_0001+Out250in800_0002+Out250in800_0003+Out250in800_0004+Out250in800_0005+Out250in800_0006+Out250in800_0007+Out250in800_0008+Out250in800_0009)./9;
avgOut250in900=(Out250in900_0001+Out250in900_0002+Out250in900_0003+Out250in900_0004+Out250in900_0005+Out250in900_0006+Out250in900_0007)./7;
avgOut250in0=(Out250out0_0001+Out250out0_0002+Out250out0_0003+Out250out0_0004+Out250out0_0005+Out250out0_0006+Out250out0_0007+Out250out0_0008+Out250out0_0009)./9;

%%%%%%%%%%%%%%%%%Double Conversions%%%%%%%%%%%%%%%%%%%%%%
1500
avgO250i1500UNFILTDouble= double(avgO250i1500UNFILT)+1;
avgOut250in1500Double= double(avgOut250in1500)+1;
1400
avgO250i1400UNFILTDouble= double(avgO250i1400UNFILT)+1;
avgOut250in1400Double= double(avgOut250in1400)+1;
1300
avgO250i1300UNFILTDouble= double(avgO250i1300UNFILT)+1;
avgOut250in1300Double= double(avgOut250in1300)+1;
1200
avgO250i1200UNFILTDouble= double(avgO250i1200UNFILT)+1;
avgOut250in1200Double= double(avgOut250in1200)+1;
1100
avgO250i1100UNFILTDouble= double(avgO250i1100UNFILT)+1;
avgOut250in1100Double= double(avgOut250in1100)+1;

1000
avgO250i1000UNFILTDouble= double(avgO250i1000UNFILT)+1;
avgOut250in1000Double= double(avgOut250in1000)+1;
900
avgO250i900UNFILTDouble= double(avgO250i900UNFILT)+1;
avgOut250in900Double= double(avgOut250in900)+1;
800
avgO250i800UNFILTDouble= double(avgO250i800UNFILT)+1;
avgOut250in800Double= double(avgOut250in800)+1;
600
avgO250i600UNFILTDouble= double(avgO250i600UNFILT)+1;
avgOut250in600Double= double(avgOut250in600)+1;
400
avgO250i400UNFILTDouble= double(avgO250i400UNFILT)+1;
avgOut250in400Double= double(avgOut250in400)+1;
200
avgO250i200UNFILTDouble= double(avgO250i200UNFILT)+1;
avgOut250in200Double= double(avgOut250in200)+1;
250 outer only
avgOut250in0Double= double(avgOut250in0)+1;

%%%%%%%%%Flow Pictures with subtracted 250 outer for baseline %%%%%%
flow1500.tif= avgOut250in0-avgOut250in1500;
flow1400.tif=avgOut250in0-avgOut250in1400;
flow1300.tif=avgOut250in0-avgOut250in1300;
flow1200.tif=avgOut250in0-avgOut250in1200;
flow1100.tif=avgOut250in0-avgOut250in1100;
flow1000.tif=avgOut250in0-avgOut250in1000;
flow900.tif=avgOut250in0-avgOut250in900;
flow800.tif=avgOut250in0-avgOut250in800;
flow600.tif=avgOut250in0-avgOut250in600;
flow400.tif=avgOut250in0-avgOut250in400;
flow200.tif=avgOut250in0-avgOut250in200;

%%%%%%%%%Flow data with subtracted baseline DOUBLE!!!%%%
flow1500Double= avgOut250in0Double-avgOut250in1500Double;
flow1400Double=avgOut250in0Double-avgOut250in1400Double;
flow1300Double=avgOut250in0Double-avgOut250in1300Double;
flow1200Double=avgOut250in0Double-avgOut250in1200Double;
flow1100Double=avgOut250in0Double-avgOut250in1100Double;
flow1000Double=avgOut250in0Double-avgOut250in1000Double;
flow900Double=avgOut250in0Double-avgOut250in900Double;
flow800Double=avgOut250in0Double-avgOut250in800Double;
flow600Double=avgOut250in0Double-avgOut250in600Double;
flow400Double=avgOut250in0Double-avgOut250in400Double;

```
flow200Double=avgOut250in0Double-avgOut250in200Double;


%Plot of centerlines with no post processing%%%%
hold on
plot (avgOut250in1500 (220,1:435), 'DisplayName', '1500 SLPM', 'YDataSource',
'avgOut250in1500(217,1:435)','Color','b'); figure(gcf)
plot (avgOut250in1400 (220,1:435), 'DisplayName', '1400 SLPM', 'YDataSource',
'avgOut250in1400(217,1:435)','Color','b'); figure(gcf)
plot (avgOut250in1300 (220,1:435), 'DisplayName', '1300 SLPM', 'YDataSource',
'avgOut250in1300(217,1:435)','Color','r'); figure(gcf)
plot (avgOut250in1200 (220,1:435), 'DisplayName', '1200 SLPM', 'YDataSource',
'avgOut250in1200(217,1:435)','Color','r'); figure(gcf)
plot (avgOut250in1100 (220,1:435), 'DisplayName', '1100 SLPM', 'YDataSource',
'avgOut250in1100(217,1:435)','Color','k'); figure(gcf)
plot (avgOut250in1000 (220,1:435), 'DisplayName', '1000 SLPM', 'YDataSource',
'avgOut250in1000(217,1:435)','Color','g'); figure(gcf)
plot (avgOut250in900 (220,1:435), 'DisplayName', '900 SLPM', 'YDataSource',
'avgOut250in900(217,1:435)','Color','b'); figure(gcf)
plot (avgOut250in800 (220,1:435), 'DisplayName', '800 SLPM', 'YDataSource',
'avgOut250in800(217,1:435)','Color','k'); figure(gcf)
plot (avgOut250in600 (220,1:435), 'DisplayName', '600 SLPM', 'YDataSource',
'avgOut250in600(217,1:435)','Color','r'); figure(gcf)
plot (avgOut250in400 (220,1:435), 'DisplayName', '400 SLPM', 'YDataSource',
'avgOut250in400(217,1:435)','Color','c'); figure(gcf)
plot (avgOut250in200 (220,1:435), 'DisplayName', '200 SLPM', 'YDataSource',
'avgOut250in200(217,1:435)','Color','k'); figure(gcf)
plot (avgOut250in0 (220,1:435), 'DisplayName', '0 SLPM', 'YDataSource',
'avgOut250in0(217,1:435)','Color','m'); figure(gcf)
xlabel('X location')
set(gca,'XTick',(39.5:77.75:350.5))
set(gca,'XTickLabel',{'-D/2','-D/4','0','D/4','D/2'})
ylabel('Intensity')


%%%%%%%%%%%%Plot of centerline intensity with baseline
subtraction%%%%%%%%%%%%%
hold on
plot (flow1500Double(220,1:435), 'DisplayName', '1500 SLPM','YDataSource',
'flow1500Double(217,1:435)','Color','b'); figure(gcf)
plot (flow1400Double(220,1:435), 'DisplayName', '1400 SLPM','YDataSource',
'flow1400Double(217,1:435)','Color','g'); figure(gcf)
plot (flow1300Double(220,1:435), 'DisplayName', '1300 SLPM', 'YDataSource',
'flow1300Double(217,1:435)','Color','r'); figure(gcf)
```

```
plot (flow1200Double(220,1:435), 'DisplayName', '1200 SLPM', 'YDataSource',
'flow1200Double(217,1:435)','Color','c'); figure(gcf)
plot (flow1100Double(220,1:435), 'DisplayName', '1100 SLPM', 'YDataSource',
'flow1100Double(217,1:435)','Color','m'); figure(gcf)
plot (flow1000Double(220,1:435), 'DisplayName', '1000 SLPM', 'YDataSource',
'flow1000Double(217,1:435)','Color','k'); figure(gcf)

plot (flow900Double(220,1:435), 'DisplayName', 'flow900', 'YDataSource',
'flow900Double(217,1:435)','Color','k'); figure(gcf)
plot (flow800Double(220,1:435), 'DisplayName', '800 slm', 'YDataSource',
'flow800Double(217,1:435)','Color','b'); figure(gcf)
plot (flow600Double(220,1:435), 'DisplayName', '600 slm', 'YDataSource',
'flow600Double(217,1:435)','Color','g'); figure(gcf)
plot (flow400Double(220,1:435), 'DisplayName', '400 slm', 'YDataSource',
'flow400Double(217,1:435)','Color','r'); figure(gcf)
plot (flow200Double(220,1:435), 'DisplayName', '200 slm', 'YDataSource',
'flow200Double(217,1:435)','Color','k'); figure(gcf)
legend '900 SLPM' '800 SLPM' '600 SLPM' '400 SLPM' '200 SLPM'
xlabel('X location')
set(gca,'XTick',(39.5:77.75:350.5))
set(gca,'XTickLabel',{'-D/2','-D/4','0','D/4','D/2'})
ylabel('Intensity')

%%%%Normalization of FRS by Unfiltered Signal%%%%%%%%%%%%%%%%%%%
flow1500Normalized=(avgOut250in1500Double(219,1:435)./avgO250i1500UNFILTDo
uble(226,1:435));
flow1400Normalized=(avgOut250in1400Double(219,1:435)./avgO250i1400UNFILTDo
uble(226,1:435));
flow1300Normalized=(avgOut250in1300Double(219,1:435)./avgO250i1300UNFILTDo
uble(226,1:435));
flow1200Normalized=(avgOut250in1200Double(219,1:435)./avgO250i1200UNFILTDo
uble(226,1:435));
flow1100Normalized=(avgOut250in1100Double(219,1:435)./avgO250i1100UNFILTDo
uble(226,1:435));
flow1000Normalized=(avgOut250in1000Double(219,1:435)./avgO250i1000UNFILTDo
uble(226,1:435));
flow900Normalized=(avgOut250in900Double(219,1:435)./avgO250i900UNFILTDouble
(226,1:435));
flow800Normalized=(avgOut250in800Double(219,1:435)./avgO250i800UNFILTDouble
(226,1:435));
flow600Normalized=(avgOut250in600Double(219,1:435)./avgO250i600UNFILTDouble
(226,1:435));
flow400Normalized=(avgOut250in400Double(219,1:435)./avgO250i400UNFILTDouble
(226,1:435));
flow200Normalized=(avgOut250in200Double(219,1:435)./avgO250i200UNFILTDouble
(226,1:435));
```

```
%%%%%%%%%%%%Plot of unfiltered centerline intensity%%%%%%%%%%%%%%%
hold on
plot (avgO250i1500UNFILTDouble(226,1:435),'DisplayName','1500 SLPM','color','r')
plot (avgO250i1400UNFILTDouble(226,1:435),'DisplayName','1400 SLPM','color','g')
plot (avgO250i1300UNFILTDouble(226,1:435),'DisplayName','1300 SLPM','color','b')
plot (avgO250i1200UNFILTDouble(226,1:435),'DisplayName','1200 SLPM','color','c')
plot (avgO250i1100UNFILTDouble(226,1:435),'DisplayName','1100 SLPM','color','k')
plot (avgO250i1000UNFILTDouble(226,1:435),'DisplayName','1000 SLPM','color','m')
plot (avgO250i900UNFILTDouble(226,1:435),'DisplayName','900 SLPM','color','r')
plot (avgO250i800UNFILTDouble(226,1:435),'DisplayName','800 SLPM','color','g')
plot (avgO250i600UNFILTDouble(226,1:435),'DisplayName','600 SLPM','color','b')
plot (avgO250i400UNFILTDouble(226,1:435),'DisplayName','400 SLPM','color','c')
plot (avgO250i200UNFILTDouble(226,1:435),'DisplayName','200 SLPM','color','k')
plot (avgOuter250OnlyUNFILT(226,1:435),'DisplayName','0 SLPM','color','b')
plot (avgNoflowUNFILT(225,1:435),'DisplayName','No Flow','color','r')
xlabel('X location')
set(gca,'XTick',(39.5:77.75:350.5))
set(gca,'XTickLabel',{'-D/2','-D/4','0','D/4','D/2'})
ylabel('Unfiltered Rayleigh Scattering Intensity')

%%%%%%%%%%%%%%Plot of normalized centerline
intensity%%%%%%%%%%%%%%%
hold on
plot (flow1500Normalized, 'DisplayName', '1500 SLPM', 'YDataSource',
'flow1500Normalized','Color','r'); figure(gcf)
plot (flow1400Normalized, 'DisplayName', '1400 SLPM', 'YDataSource',
'flow1400Normalized','Color','g'); figure(gcf)
plot (flow1300Normalized, 'DisplayName', '1300 SLPM', 'YDataSource',
'flow1300Normalized','Color','b'); figure(gcf)
plot (flow1200Normalized, 'DisplayName', '1200 SLPM', 'YDataSource',
'flow1200Normalized','Color','c'); figure(gcf)
plot (flow1100Normalized, 'DisplayName', '1100 SLPM', 'YDataSource',
'flow1100Normalized','Color','k'); figure(gcf)
plot (flow1000Normalized, 'DisplayName', '1000 SLPM', 'YDataSource',
'flow1000Normalized','Color','m'); figure(gcf)
plot (flow900Normalized, 'DisplayName', '900 SLPM', 'YDataSource',
'flow900Normalized','Color','r'); figure(gcf)
plot (flow800Normalized, 'DisplayName', '800 SLPM', 'YDataSource',
'flow800Normalized','Color','g'); figure(gcf)
plot (flow600Normalized, 'DisplayName', '600 SLPM', 'YDataSource',
'flow600Normalized','Color','b'); figure(gcf)
plot (flow400Normalized, 'DisplayName', '400 SLPM', 'YDataSource',
'flow400Normalized','Color','c'); figure(gcf)
plot (flow200Normalized, 'DisplayName', '200 SLPM', 'YDataSource',
'flow200Normalized','Color','k'); figure(gcf)
```

```
xlabel('X location')
set(gca,'XTick',(39.5:77.75:350.5))
set(gca,'XTickLabel',{'-D/2','-D/4','0','D/4','D/2'})
ylabel('Ratio of Filtered to Unfiltered Intensity')
hold off
```

1. REPORT DATE *(DD-MM-YYYY)* 13-06-2006	2. REPORT TYPE Master's Thesis		3. DATES COVERED *(From – To)* July 2005 – June 2006		
4. TITLE AND SUBTITLE Characterization of a Coflow Nozzle for use in a Filtered Rayleigh Scattering System			5a. CONTRACT NUMBER		
			5b. GRANT NUMBER		
			5c. PROGRAM ELEMENT NUMBER		
6. AUTHOR(S) Miceli, David S. Ensign, USN			5d. PROJECT NUMBER		
			5e. TASK NUMBER		
			5f. WORK UNIT NUMBER		
7. PERFORMING ORGANIZATION NAMES(S) AND ADDRESS(S) Air Force Institute of Technology Graduate School of Engineering and Management (AFIT/EN) 2950 Hobson Way, Building 640 WPAFB OH 45433-8865			8. PERFORMING ORGANIZATION REPORT NUMBER AFIT/GAE/ENY/06-J10		
9. SPONSORING/MONITORING AGENCY NAME(S) AND ADDRESS(ES) N/A			10. SPONSOR/MONITOR'S ACRONYM(S)		
			11. SPONSOR/MONITOR'S REPORT NUMBER(S)		
12. DISTRIBUTION/AVAILABILITY STATEMENT APPROVED FOR PUBLIC RELEASE; DISTRIBUTION UNLIMITED.					
13. SUPPLEMENTARY NOTES					

14. ABSTRACT

Research was conducted on the flow field exiting a co-annular flow nozzle for use in filtered Rayleigh scattering flow visualizations. More specifically, the flow visualizations were of the flow field exiting a coflow nozzle and illuminated by a tunable, nominal 4.2 watt narrow line width Argon laser operating at 514.5nm. ND:YAG lasers are typically used in this application, but some of the properties of a tunable Argon laser make it an attractive alternative. Before generating flow visualizations, the coflow nozzle was characterized both experimentally and computationally. Due to a flow asymmetry in the outer annulus flow field, the nozzle was redesigned using a commercially available computational fluid dynamics program (Fluent) to produce a more homogeneous exit plane velocity profile. The redesigned nozzle was built and experimentally tested through the use of a three dimensional traverse controlled Pitot probe resulting in good relationship between the computational and experimental results. The sharp cutoff molecular iodine filters used to reduce the incident frequency light were tested and the locations of their iodine absorption transitions were determined. Finally, the argon laser was used to produce flow visualizations at both 100 Hz and 1 kHz frame rates.

15. SUBJECT TERMS
  Filtered Rayleigh scattering, argon-ion laser, coflow nozzle, iodine filter.

16. SECURITY CLASSIFICATION OF: Unclassified			17. LIMITATION OF ABSTRACT	18. NUMBER OF PAGES	19a. NAME OF RESPONSIBLE PERSON Reeder, Mark F, Assistant Professor, AFIT
a. REPORT U	b. ABSTRACT U	c. THIS PAGE U	UU	138	19b. TELEPHONE NUMBER *(Include area code)* (937) 255-3636, x4530 (mark.reeder@afit.edu)